Advancing Hydrophobic Desalination Membranes using Initiated Chemical Vapor Deposition (iCVD)

by

Amelia Tepper Servi

S.B. Mechanical Engineering, Massachusetts Institute of Technology, 2010

S.M. Mechanical Engineering, Massachusetts Institute of Technology, 2013

Submitted to the Department of Mechanical Engineering
in partial fulfillment of the requirements for the degree of

Doctor of Philosophy in Mechanical Engineering

at the

MASSACHUSETTS INSTITUTE OF TECHNOLOGY

June 2016

Author:＿＿＿＿＿＿＿＿＿＿＿＿＿＿＿＿＿＿＿＿＿＿＿＿＿＿＿＿＿＿＿＿
Department of Mechanical Engineering
May 20, 2016

Certified by:＿＿＿＿＿＿＿＿＿＿＿＿＿＿＿＿＿＿＿＿＿＿＿＿＿＿＿＿＿
Karen K. Gleason
Associate Provost and Alexander and I. Michael Kasser Professor of Chemical Engineering
Thesis Supervisor

Certified by:＿＿＿＿＿＿＿＿＿＿＿＿＿＿＿＿＿＿＿＿＿＿＿＿＿＿＿＿＿
John H. Lienhard V
Abdul Latif Jameel Professor of Water
Thesis Committee Chair

Accepted by:＿＿＿＿＿＿＿＿＿＿＿＿＿＿＿＿＿＿＿＿＿＿＿＿＿＿＿＿＿
Rohan Abeyaratne
Graduate Officer, Department of Mechanical Engineering

Advancing Hydrophobic Desalination Membranes using Initiated Chemical Vapor Deposition (iCVD)

by

Amelia Tepper Servi

Submitted to the Department of Mechanical Engineering on May 20, 2016
in partial fulfillment of the requirements for the degree of
Doctor of Philosophy in Mechanical Engineering

ABSTRACT

Hydrophobic membranes are the central component of membrane distillation (MD) desalination systems. Optimizing their design is crucial for efficient desalination. There are many requirements on MD membranes. These include high liquid entry pressure (LEP) and high permeability to water vapor. There are many available manufacturing methods for producing hydrophobic membranes. An important subset of these methods use surface modification to prepare hydrophobic composite membranes. The many options for MD membrane design results in lack of consensus about how to achieve optimal performance. In this thesis we use initiated chemical vapor deposition (iCVD) to study how surface modification parameters and membrane morphology contribute to MD membrane performance. We introduce new models and analysis methods to support experimental results. This work informs hydrophobic MD membrane design by clarifying the roles of different membrane elements. By advancing MD technology, we increase capacity to produce fresh water for society.

Thesis Supervisor: Karen K. Gleason
Thesis Committee: John H. Lienhard V, Gareth McKinley

Acknowledgments

First and foremost, I want to thank my advisor, Professor Karen Gleason. She has been a role model for achievement, hard work, clarity and strength. She has helped me develop as a researcher and has always been encouraging while also pushing for my best work. I also want to thank my committee members, Professor John H. Lienhard V and Professor Gareth McKinley. They have been great coaches and I have appreciated their feedback and the chance to learn by their example. I am also grateful to Professor Hassan A. Arafat at the Masdar Institute for sharing his expertise and advice.

I have been incredibly lucky to work with such a great group of people in the G-Lab. It has been wonderful being in the company of such high-achieving, knowledgeable, intelligent and kind-hearted people. In particular, I want to thank Peter Kovacik, Nan Chen, Andong Liu and Dan Soto for being great officemates at ISN, and Priya Moni and Rong Yang for their support and friendship. I also want to thank our administrative assistants: Gwen Wilcox, Anthee Travers and Alina Haverty without whom the lab would not run nearly as smoothly.

I would like to express my appreciation to my other collaborators and classmates at MIT and the Masdar Institute of Science and Technology: Fei Guo, David Warsinger, Vicky Lee, Jaichander Swaminathan, Jehad Kharraz, and Elena Guillen-Burrieza have been a joy to work with. I also want to thank my UROP students: Marie Muodio, Will Livernois, David Klee, Katie Notarangelo and Brook Eyob. I have been continually impressed with their intelligence, creativity and work ethic and greatly appreciated their diligence. I am also grateful to Susan Murcott, Mary Rowe, Barbara Hughey, Thalia Rubio, and Leslie Regan who have all support and guidance over the years.

I have only gratitude to my friends: Faye Wu, Priya Moni, David Warsinger, Nevan Hanumara, Chelsey Faller, Claire Winchell-Manning, Natasha Eilbert, Jared Dominguez, Henry Hallem, Matt Ritter, Steven Tobias, Roxana Safipour, Tamzin Mitchell and many others friends and roommates. I am also extremely thankful to my family: Mom, Dad, Susan, Jim, Joe and Jesse. Their support has been invaluable. I am grateful to my grandparents who inspire me and especially my grandfather, Al, who has been a steady source of encouragement. Special thanks as well to my aunts and uncles and especially my aunt Devorah – I have felt their support from near and far.

I lastly want to express my gratitude to MIT itself. It has been a strange and wonderful place where I have felt immense freedom to learn and grow. I had no idea what I was getting into when I first arrived, but I will miss this place.

Table of Contents

List of Figures

7

List of Tables

List of Acronyms and Abbreviations

ACA	advancing contact angle
AFM	atomic force microscope
AGMD	air gap membrane distillation
ARXPS	angle-resolved X-ray photoelectron spectroscopy
ATR	attenuated total reflection
C6PFA	1H, 1H, 2H, 2H - perfluorooctyl acrylate
C-B	Cassie-Baxter
CA	contact angle
$CaSO_4$	calcium sulfate
CFP	capillary flow porometry
CVD	chemical vapor deposition
DCMD	direct contact membrane distillation
DI	deionized
DVB	divinyl benzene
ES	electrospun
FTIR	Fourier transform infrared
iCVD	initiated chemical vapor deposition
Kn	Knudsen number
LEP	liquid entry pressure
LEP_w	water liquid entry pressure
MD	membrane distillation
MED	multi-effect evaporation/distillation
MSF	multi-stage flash distillation
NaCl	sodium chloride
PA6(3)T	poly(trimethyl hexamethylene terephthalamide)
PC	polycarbonate
PCTE	track-etched polycarbonate
PC6PFA	poly(1H, 1H, 2H, 2H - perfluorooctyl acrylate)
PDVB	poly(divinyl benzene)
PECS	precision etching coating system
PFDA	1H, 1H, 2H, 2H - perfluorodecyl acrylate
PFHxA	$C_5F_{11}COOH$
PFOA	$C_7F_{13}COOH$
PGMD	permeate gap membrane distillation
PI	phase-inversion
PP	polypropylene
PPFDA	poly(1H, 1H, 2H, 2H - perfluorodecyl acrylate)
PSD	pore size distribution

PTFE	poly(tetrafluoroethylene)
PVDF	poly(vinylidene fluoride)
PVP	polyvinylpyrrolidone
RCA	receding contact angle
RO	reverse osmosis
SCA	static contact angle
SEM	scanning electron microscope
S_L	step coverage
SR	salt rejection
TBPO	tert-butyl peroxide
TE	track-etched
UNESCO	United Nations Educational Scientific and Cultural Organization
WASH	water, sanitation and hygiene

CHAPTER ONE

Introduction

Abstract

Desalination technologies, including membrane distillation (MD), address the critical societal need for fresh water. In this thesis, we advance the science of MD membranes in order to improve the effectiveness of MD desalination. We prepare the membranes in this thesis using initiated chemical vapor deposition (iCVD) of polymer films deposited onto multiple different base membranes. We use these composite membranes to analyze how iCVD films and membrane morphology affect membrane performance. Our findings can inform the development of more efficient MD membranes with improved capacity to produce fresh water.

1.1. Need for freshwater and desalination

Fresh water is essential for life on Earth. We use it for personal water supply, sanitation and hygiene (WASH), agriculture, energy production and manufacturing. Yet shortage of fresh water is a worldwide problem. By 2030, UNESCO projects a 40% global freshwater deficit [1]. Desalination technology has been increasingly used to fill this gap. In 2007, the total installed desalination capacity worldwide was 47.6 million m^3/d. By 2015, it was projected to more than double to 97.5 million m^3/day [2].

1.2. Membrane distillation

There are many desalination technologies currently available. These technologies fall into two main categories. Thermal desalination technologies use phase-change to separate water from non-volatiles such as salts. These technologies include multi-effect evaporation/distillation (MED) and multi-stage flash distillation (MSF). Membrane-based desalination technologies use a membrane to filter saline solution to produce fresh water. These technologies include reverse osmosis (RO). Membrane distillation (MD) is a hybrid of these categories using both phase-change and a membrane to desalinate water.

This hybrid approach has many strengths. MD operates at lower temperatures than other thermal processes such as MSF and MED. This allows the use of low-grade energy sources (e.g. solar, waste heat and geothermal) [3]. The wound membrane modules also make MD more compact than other thermal options. MD operates at ambient pressure, so does not use powerful pumps like other membrane processes. In addition, as a thermal process, MD can treat feeds with higher solute concentration than can RO. Disadvantages of MD include slow water production, lack of

commercial membranes and high energy consumption. This difference in energy consumption is highlighted in Table 1-1 which shows energy consumption and costs for conventional water treatment, RO and MD.

Table 1-1. Minimum estimated energy consumption and cost of three water treatment systems. For MD, costs assume (1) low-grade energy and (2) conventional energy sources.

Technology	Energy consumption (kWh/m^3)	Minimum cost ($/m^3)
Conventional	0.1 [2]	0.25 [2]
Seawater reverse osmosis	2.5 [2]	0.50 [2]
Membrane distillation	39.7 [4]	0.64[1], 1.23[2] [4]

Despite its strengths, MD represents a small fraction of global desalination capability. In 2016, 63% of worldwide desalination capacity is RO, 23% is MSF and 8% is MED. The rest of the industry comprises all other desalination technologies including MD [2]. However, MD is still an important desalination technology, especially for remote locations or "extreme" applications. These applications include treatment of high salinity brine, systems powered with solar panels and water treatment aboard nautical and space ships [3] (Fig. 1-1). Harnessing alternative energy sources, identifying additional applications and increasing efficiency through improved system and membrane design are expected to further its reach [3].

Fig. 1-1. Solar-powered Oryx 150 membrane distillation system installed in Tunisia [5].

In this thesis, we study the hydrophobic membranes that are the critical components of MD systems. Improving MD membrane design can increase the efficiency and appeal of MD technology. In MD, the hydrophobic membrane acts as a barrier against a heated feed stream (e.g. seawater) (Fig. 1-2). A temperature difference across the membrane causes a partial pressure gradient that drives water vapor through the membrane leaving salt and other contaminants behind. We use three MD system configurations in this thesis (Fig. 1-2b – Fig. 1-2d). In direct contact membrane distillation (DCMD), a stream of chilled distillate cools the non-feed side of the membrane. Water vapor passing through the membrane condenses in this stream. In air gap membrane distillation (AGMD), water vapor passes through the membrane where it condenses on a chilled solid plate. The condensate collects in a separate vessel. Permeate gap membrane distillation (PGMD) is like DCMD, but the distillate stream is unmoving. The non-feed side of the membrane is cooled by a chilled solid plate like the one used for AGMD. DCDM and AGMD are standard membrane distillation configurations. PGMD is an experimental configuration.
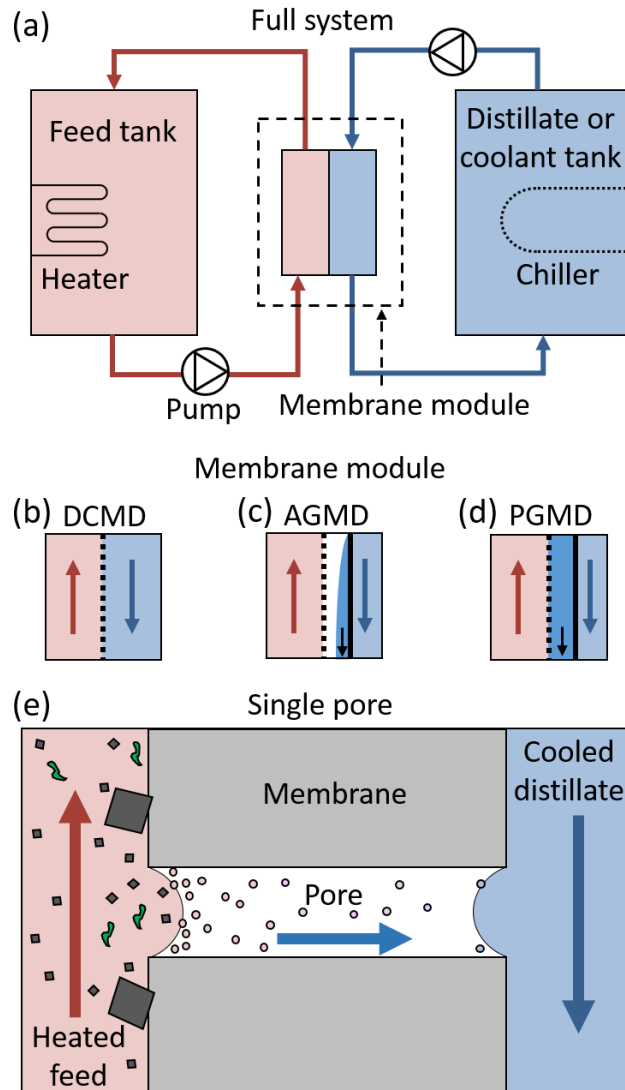
Fig. 1-2. (a) Schematic of a full membrane distillation system. Three membrane module configurations are shown: (b) Direct contact membrane distillation (DCMD), (c) air gap membrane distillation (AGMD), and (d) permeate gap membrane distillation (PGMD). In (b – d), the dashed vertical lines are membranes, the solid, thick vertical lines are solid plates. (e) shows a single pore in a membrane in a DCMD system. Water vapor travels through the pore from the heated feed to the cooled distillate, leaving salts and organic matter behind. Menisci form at both ends of the pore, but high liquid entry pressure (LEP) prevents the pore from fully wetting.

There are many requirements that must be met by MD membranes. The membranes must have high liquid entry pressure (LEP) to prevent wetting (Fig. 1-2e). They must also be highly permeable to water vapor, resist fouling and be stable over time. In addition, low cost and environmental safety must be preserved. There are no commercial membranes currently sold for MD. Instead, MD systems use membranes developed for other applications [6]. Table 1-2 shows a representative sampling of these membranes. Experimental membranes are continually being developed to optimize membrane performance [7]. A particularly versatile approach is to start with a hydrophilic base membrane. This membrane is then treated to reduce surface energy [8–12]. This method decouples the base material from surface properties, increasing the potential for optimization. In this thesis, we follow this approach, using initiated chemical vapor deposition (iCVD) as the surface treatment.

Table 1-2. Representative commercial membranes used for membrane distillation. TF200 and TF450 are stretched polytetrafluoroethylene (PTFE) mounted on polypropylene (PP) backings. GVHP and HVHP are phase-inversion polyvinyldene fluoride (PVDF) membranes. Membrane coefficient describes the rate of water vapor flux through the membrane in a DCMD system. LEP_w is the liquid entry pressure to water. Data compiled from [6].

Trade name	Manufacturer	Material	Mean pore size (μm)	LEP_w (kPa)	Membrane coefficient (kg/m^2/pa/s)
TF200	Gelman	PTFE/PP	0.20	282	14.5×10^{-7}
TF450	Gelman	PTFE/PP	0.45	138	21.5×10^{-7}
GVHP	Millipore	PVDF	0.22	204	3.8×10^{-7}
HVHP	Millipore	PVDF	0.45	105	4.8×10^{-7}

1.3. Initiated chemical vapor deposition

Initiated chemical vapor deposition (iCVD) was first conducted in the Gleason Lab at MIT in 1996 [13]. It is a solventless, free-radical polymerization technology [14]. iCVD polymer films range in thickness from nanometers to microns. Deposition rates can be as high as 375 nm/min [15]. iCVD can be conducted in small experimental systems or in commercial roll-to-roll systems [16]. Using the model for CVD processes by Aixtron [17], the costs of the iCVD films in this thesis would be on the order of 10 \$/m^2 at industrial scale.

In iCVD, the substrate (membrane) is placed on a cooled stage in an iCVD vacuum chamber (Fig. 1-3). The chamber is evacuated and monomer and initiated flow into the iCVD chamber in vapor phase. A pump maintains constant pressure in the chamber. In the chamber, hot filaments above the membrane break the entering initiator molecules into radicals. These radicals react with monomer adsorbed to the membrane, growing a conformal polymer film. Because monomer and initiator enter the chamber as vapor, the iCVD film conformality is not limited by surface tension of the liquid monomer (Fig. 1-4). However, the thickness of the film within the membrane pores is not uniform. Factors such as functional groups, monomer fractional saturation pressure and pore aspect ratio determine the distribution [18–20]. This becomes important when analyzing the effects of the iCVD film on pore permeability.
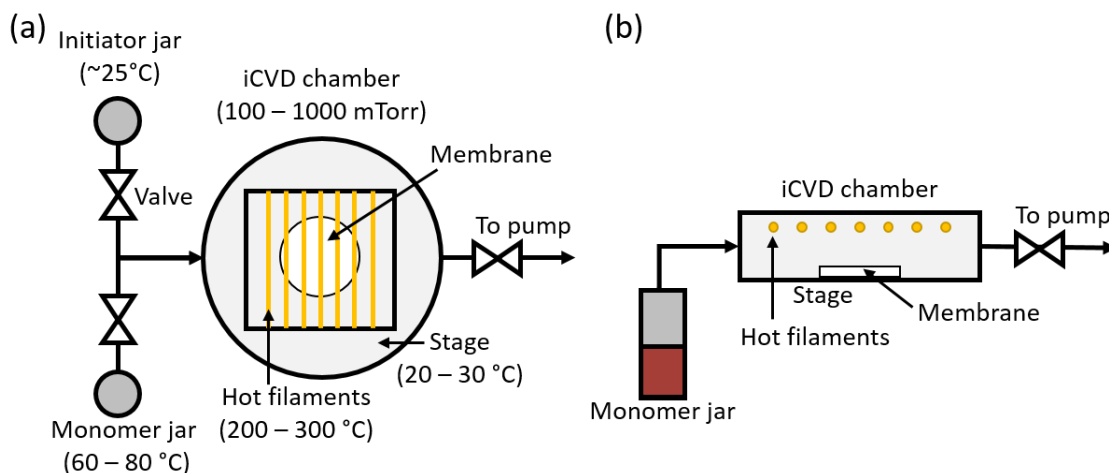
Fig. 1-3. (a) Top view and (b) side view schematics of an iCVD system. Vapor-phase monomer and initiator flow into an iCVD chamber the membrane. Polymer growth occurs directly on the membrane. Chamber dimensions are 38 mm height and 246 mm diameter.
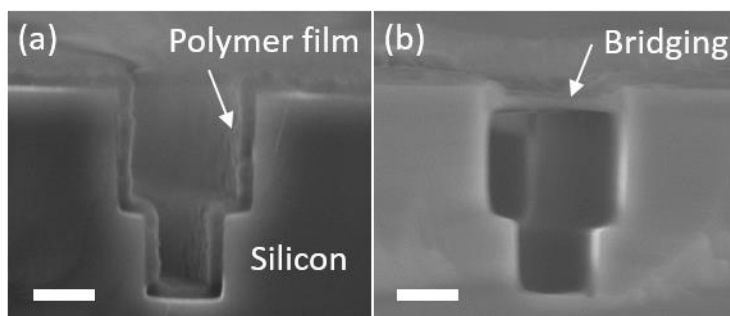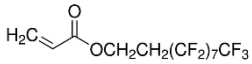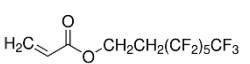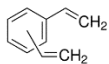
Fig. 1-4. (a) iCVD poly(1H, 1H, 2H, 2H – perfluorodecyl acrylate) (pPFDA) conformally coating a track-etched silicon wafer. (b) pPFDA deposited onto a track-etched wafer in liquid phase. This film exhibits bridging across the top of the pore due to surface tension. Scale bar is 2 µm.

iCVD can deposit many polymer chemistries. In this thesis, we use three hydrophobic chemistries (Table 1-3). poly(1H, 1H, 2H, 2H – perfluorodecyl acrylate) (pPFDA) is a widely used hydrophobic polymer with many previous uses in iCVD [21–23]. It has high advancing contact

23

angle (~135 °) and low contact angle hysteresis due to its CF_3 end-groups and semi-crystalline structure [24]. However, the eight carbon perfluorinated side chains of pPFDA are persistent in the environment and toxic to humans [25]. In 2015 it was banned from commercial use. As a well-characterized iCVD polymers with exceptional properties, it is still useful for research. poly(1H, 1H, 2H, 2H-perfluorooctyl acrylate) (pC6PFA) is a shorter side chain analog of pPFDA. The pC6PFA has similar advancing contact angle as pPFDA, but it is not semi-crystalline. The reorientation of pC6PFA disordered side chains in response to wetting results in a much greater contact angle hysteresis. The six carbon perfluorinated compounds are orders of magnitude less persistence in the environment than the eight carbon analogs. Thus, C6PFA has been proposed as an environmentally friendly substitute for pPFDA [25]. The third polymer that we use is poly(divinyl benzene) (pDVB). DVB is a cross-linking monomer. It is hydrophobic but only moderately so. It is inexpensive, non-toxic, robust and exceptionally easy to process, making it appealing for membrane treatment.

Table 1-3. The three iCVD polymers used in the thesis: poly(1H, 1H, 2H, 2H-perfluorodecyl acrylate) (pPFDA), poly(1H, 1H, 2H, 2H-perfluorooctyl acrylate) (pC6PFA) and poly(divinyl benzene) (pDVB). ACA is the advancing contact angle. RCA is the receding contact angle. PFOA ($C_7F_{13}COOH$) and PFHxA ($C_5F_{11}COOH$) are byproducts of PFDA and C6PFA respectively. Styrene (C_8H_8) has similar structure to DVB. p_{sat} is saturation pressure. Lower saturation pressure makes it more difficult to prevent condensation during iCVD deposition.

Monomer	PFDA	C6PFA	DVB
ACA (°)	> 130	> 130	~ 100
RCA (°)	~ 100	~ 40	~ 70
Persistence (half-life, human plasma)	PFOA: 1000 days [26]	PFHxA: 2 – 20 days [26]	Styrene: 3.9 hours [27]
Cost (Sigma Aldrich)	$455 / 25 mL	$625 / 25 mL	$155 / 1 L
Processing difficulty (p_{sat} at 25 °C, Torr[1])	0.056	0.332	0.650
Structure			

1.4. Scope of thesis

In this thesis, we use iCVD to advance the science of membranes for membrane distillation. We use two approaches. We first study how the iCVD polymer films themselves affect membrane performance. In Chapter 2 we analyze the effects of iCVD film thickness and conformality on the permeability of membranes to water vapor. We develop an original model for permeability of asymmetric membranes and assess the potential of non-conformal iCVD films to increase

---

[1] 1 Torr = 133.322 Pa

membrane permeability while maintaining liquid entry pressure (LEP). In Chapter 3 we use iCVD to analyze the effects surface energy on LEP. We also develop an original model for LEP of complex pores that includes the effects of pore interaction. In Chapter 5.1 (collaborative work based in the Professor Lienhard at MIT) we analyze how iCVD film surface energy and the introduction of air layers affect inorganic and organic fouling [28]. Together, these studies produce guidelines for how iCVD can best be used to develop improved membranes for MD. Aspects of these findings also extend to other membrane surface treatment methods.

Second, we use iCVD to standardize surface energy to enable studies of membrane morphology. By removing surface energy as a variable, we can study the effects of morphology on membrane performance. In Chapter 4 (collaborative work based in the Professor Arafat Lab at Masdar Institute) we determine how membrane morphology affects LEP across membrane types [29]. We evaluate an existing model for LEP and discuss empirical correlations between morphology and LEP. In Chapter 5.2 (collaborative work based in the Professor Rutledge Lab at MIT) we analyze how fiber diameter determines the LEP and vapor flux of electrospun membranes [21].

Experimental details for each chapter are shown in Table 1-4. In Chapter 6, we present general and specific recommendations for improving MD membrane design based on our findings.

Table 1-4. Experimental parameters for each chapter. Membrane materials: PC (polycarbonate), Nylon (unspecified polyamide), PTFE (polytetrafluoroethylene), PVDF (polyvinyldene fluoride), PA6(3)T (polytrimethyl hexamethylene terephthalamide). Membrane types: TE (track-etched), PI (phase-inversion), S (stretched), ES (electrospun). iCVD chemistries: pPFDA (poly(1H, 1H, 2H, 2H –perfluorodecyl acrylate)), pC6PFA (poly(1H, 1H, 2H, 2H – perfluorooctyl acrylate)), pDVB (poly(divinyl benzene)). MD configurations: PGMD (permeate gap membrane distillation, DCMD (direct contact membrane distillation), AGMD (air gap membrane distillation).

Chapter	Membrane material	Membrane type	iCVD chemistry(s)	MD configuration
TWO	PC	TE	pDVB, pC6PFA	PGMD
THREE	Nylon	PI	pDVB, pPFDA	DCMD
FOUR	PTFE, PVDF, Nylon, PC	S, PI, TE	pC6PFA	N/A
FIVE Part 1	PVDF	PI	pPFDA	N/A
FIVE Part 2	PA6(3)T	ES	pPFDA	AGMD

References

[1]   Water for a sustainable world, Unesco, Paris, 2015.

[2]   V.G. Gude, Desalination and sustainability – An appraisal and current perspective, Water Res. 89 (2016) 87–106.

[3]   H. Susanto, Towards practical implementations of membrane distillation, Chem. Eng. Process. Process Intensif. 50 (2011) 139–150.

[4]   S. Alobaidani, E. Curcio, F. Macedonio, G. Diprofio, H. Alhinai, E. Drioli, Potential of membrane distillation in seawater desalination: Thermal efficiency, sensitivity study and cost estimation, J. Membr. Sci. 323 (2008) 85–98.

[5]   M. Rolletschek, M. Wieghaus, Membrane distillation - Experience in field applications and potentials, in: Int. Workshop Membr. Distill. Relat. Technol., Italy, 2011.

[6]   A. Alkhudhiri, N. Darwish, N. Hilal, Membrane distillation: A comprehensive review, Desalination. 287 (2012) 2–18.

[7] M. Khayet, Membranes and theoretical modeling of membrane distillation: A review, Adv. Colloid Interface Sci. 164 (2011) 56–88.

[8] M. Essalhi, M. Khayet, Surface segregation of fluorinated modifying macromolecule for hydrophobic/hydrophilic membrane preparation and application in air gap and direct contact membrane distillation, J. Membr. Sci. 417–418 (2012) 163–173.

[9] M. Khayet, J.I. Mengual, T. Matsuura, Porous hydrophobic/hydrophilic composite membranes, J. Membr. Sci. 252 (2005) 101–113.

[10] M. Qtaishat, M. Khayet, T. Matsuura, Novel porous composite hydrophobic/hydrophilic polysulfone membranes for desalination by direct contact membrane distillation, J. Membr. Sci. 341 (2009) 139–148.

[11] Y. Zhang, R. Wang, S. Yi, L. Setiawan, X. Hu, A.G. Fane, Novel chemical surface modification to enhance hydrophobicity of polyamide-imide (PAI) hollow fiber membranes, J. Membr. Sci. 380 (2011) 241–250.

[12] Y. Liao, R. Wang, A.G. Fane, Engineering superhydrophobic surface on poly(vinylidene fluoride) nanofiber membranes for direct contact membrane distillation, J. Membr. Sci. 440 (2013) 77–87.

[13] S.J. Limb, C.B. Labelle, K.K. Gleason, D.J. Edell, E.F. Gleason, Growth of fluorocarbon polymer thin films with high CF2 fractions and low dangling bond concentrations by thermal chemical vapor deposition, Appl. Phys. Lett. 68 (1996) 2810.

[14] A.M. Coclite, R.M. Howden, D.C. Borrelli, C.D. Petruczok, R. Yang, J.L. Yagüe, A. Ugur, N. Chen, S. Lee, W.J. Jo, A. Liu, X. Wang, K.K. Gleason, 25th Anniversary Article: CVD Polymers: A New Paradigm for Surface Modification and Device Fabrication, Adv. Mater. 25 (2013) 5392–5423.

[15] M. Gupta, K.K. Gleason, Initiated Chemical Vapor Deposition of Poly(1H,1H,2H,2H-perfluorodecyl Acrylate) Thin Films, Langmuir. 22 (2006) 10047–10052.

[16] H.G. Pryce Lewis, N.P. Bansal, A.J. White, E.S. Handy, HWCVD of polymers: Commercialization and scale-up, Thin Solid Films. 517 (2009) 3551–3554.

[17] Personal communication with Mr. Jurgen Kreis (source K. K. Gleason)., (n.d.).

[18] S.H. Baxamusa, K.K. Gleason, Thin Polymer Films with High Step Coverage in Microtrenches by Initiated CVD, Chem. Vap. Depos. 14 (2008) 313–318.

[19] A. Asatekin, K.K. Gleason, Polymeric nanopore membranes for hydrophobicity-based separations by conformal initiated chemical vapor deposition, Nanoletters. 11 (2011) 677–686.

[20] M. Gupta, V. Kapur, N.M. Pinkerton, K.K. Gleason, Initiated Chemical Vapor Deposition (iCVD) of Conformal Polymeric Nanocoatings for the Surface Modification of High-Aspect-Ratio Pores, Chem. Mater. 20 (2008) 1646–1651.

[21] F. Guo, A. Servi, A. Liu, K.K. Gleason, G.C. Rutledge, Desalination by Membrane Distillation using Electrospun Polyamide Fiber Membranes with Surface Fluorination by Chemical Vapor Deposition, ACS Appl. Mater. Interfaces. 7 (2015) 8225–8232.

[22] M. Ma, Y. Mao, M. Gupta, K.K. Gleason, G.C. Rutledge, Superhydrophobic Fabrics Produced by Electrospinning and Chemical Vapor Deposition, Macromolecules. 38 (2005) 9742–9748.

[23] D.M. Warsinger, A. Servi, S. Van Belleghem, J. Gonzalez, J. Swaminathan, J. Kharraz, H.W. Chung, H.A. Arafat, K.K. Gleason, J.H. Lienhard V, Combining air recharging and membrane superhydrophobicity for fouling prevention in membrane distillation, J. Membr. Sci. 505 (2016) 241–252.

[24] K. Honda, M. Morita, H. Otsuka, A. Takahara, Molecular aggregation structure and surface properties of poly(fluoroalkyl acrylate) thin films, Macromolecules. 38 (2005) 5699–5705.

[25] R.C. Buck, J. Franklin, U. Berger, J.M. Conder, I.T. Cousins, P. de Voogt, A.A. Jensen, K. Kannan, S.A. Mabury, S.P. van Leeuwen, Perfluoroalkyl and polyfluoroalkyl substances in the environment: Terminology, classification, and origins, Integr. Environ. Assess. Manag. 7 (2011) 513–541.

[26] R.C. Buck, N. Wang, Biodegradability of perfluoroalkyl and polyfluoroalkyl substances - What do we know?, (2012). http://polyacs.net/Workshops/12fluoropolymer/home.htm.

[27] F. Brugnone, L. Perbellini, G.Z. Wang, G. Maranelli, E. Raineri, E. De Rosa, C. Saletti, C. Soave, L. Romeo, Blood styrene concentrations in a "normal" population and in exposed workers 16 hours after the end of the workshift, Int. Arch. Occup. Environ. Health. 65 (1993) 125–130.

[28] D.M. Warsinger, A. Servi, S. Van Belleghem, J. Gonzalez, J. Swaminathan, J. Kharraz, H.W. Chung, H.A. Arafat, K.K. Gleason, J.H. Lienhard V, Combining air recharging and membrane superhydrophobicity for fouling prevention in membrane distillation, J. Membr. Sci. 505 (2016) 241–252.

[29] E. Guillen-Burrieza, A. Servi, B.S. Lalia, H.A. Arafat, Membrane structure and surface morphology impact on the wetting of MD membranes, J. Membr. Sci. 483 (2015) 94–103.

CHAPTER TWO

The effects of iCVD surface modification on the permeability and wettability of MD membranes

Abstract

Membranes possessing high permeability to water vapor and adequate liquid entry pressure (LEP) are necessary for efficient membrane distillation (MD) desalination. Many MD membranes consist of a base membrane with the surface modified to decrease surface-energy. This surface-modification increases membrane LEP, but may decrease permeability by reducing pore size. In this study, we use initiated chemical vapor deposition (iCVD) to quantify the effects of surface modification on membrane permeability and LEP. The iCVD films are bilayers of poly(divinyl benzene) (pDVB) and poly(1H, 1H, 2H, 2H-perfluorooctyl acrylate) (pC6PFA). The base membranes are track-etched polycarbonate (PCTE) chosen for their well-defined 400 nm diameter cylindrical pores. We experimentally determined the effects of hydrophobic iCVD polymer films and analyzed the results by developing new models for permeability. These models incorporated the effects of the Knudsen number and the asymmetry of the pores after iCVD treatment. We found that MD membrane permeability is maximized when iCVD film thickness is minimized. Using thicker, asymmetric films to produce "bottle-neck" shaped pores has a negative effect on permeability at constant LEP. Dr. Elena Guillen-Burrieza, Dr. David M. Warsinger, William Livernois, Katie Notarangelo, Jehad Kharraz, Professor John H. Lienhard V, Professor Hassan A. Arafat and Professor Karen K. Gleason contributed to this work.

2.1. Introduction

Membrane distillation (MD) is a thermal separation process used for desalination [1–5]. In two common variants of MD, direct contact and permeate gap membrane distillation (DCMD and PGMD), a hydrophobic membrane acts as a barrier separating the heated feed stream from the cooled distillate stream [6]. The temperature difference across the membrane creates a difference in the partial pressure between the water vapor on either side. This causes a net diffusion of water vapor through the membrane from the feed to the distillate. Salt and other contaminants in the feed stream are left behind.

The hydrophobic membrane in the MD system has two roles. It must prevent liquid entry, but it must also be highly permeable to water vapor diffusion. Adequate liquid entry pressure (LEP) is necessary to prevent membrane wetting and cross-contamination. High permeability to water vapor diffusion is necessary to maintain MD system efficiency [13–16]. Currently, MD systems primarily use hydrophobic membranes developed for micro- and ultra- filtration [5]. Designing specialized membranes optimized for LEP and permeability is an area of active research. Specialized MD membranes are often prepared from a base membrane with the surface modified to decrease surface energy and increase liquid entry pressure (LEP) [7–12]. This is a versatile method that increases the options for membrane design. However, if the hydrophobic surface treatment has thickness that is a significant fraction of pore radius, it will affect the membrane's permeability to water vapor.

Permeability to water vapor depends on membrane thickness, porosity and pore structure. Increasing pore radius increases permeability. Because the water vapor must travel across the

entire membrane, variation in pore radius within the membrane impacts permeability. While larger

pores enhance permeability, they reduce LEP. If LEP becomes too low, MD is not possible.

According to the Young-Laplace model [17], LEP for cylindrical pores is given by

$$\Delta P = \frac{-2\gamma\cos(\theta)}{r_t} \tag{Eq. 2-1}$$

where γ is the solution's surface tension, θ is the contact angle, and r_t is the pore radius at the

surface of the membrane. It is important to note that while LEP is inversely proportional to pore

radius at the membrane surface, according to the Young-Laplace equation, LEP is independent of

membrane thickness and variation in pore radius within the membrane. Thus, it may be possible

to maintain a small surface pore size to achieve an acceptably high value of LEP, while enlarging

pore radius below the surface to enhance permeability. This is illustrated in Fig. 2-1 which shows

three pores with the same LEP. Fig. 2-1c has higher permeability than Fig. 2-1a and Fig. 2-1b

because the non-conformal hydrophobic coating creates an asymmetric, "bottle-neck" pore shape.

The current study explores how the thickness and conformality of the hydrophobic surface

treatment affects the relationship between LEP and permeability.
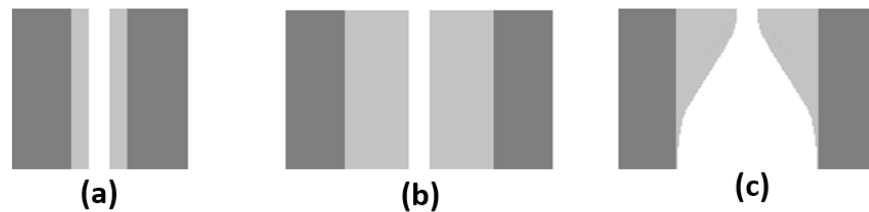
Fig. 2-1. Schematic diagrams of three pores with the same top pore radius (r_t) and LEP. The

membrane is dark grey, and the hydrophobic coating is light grey. (a) has an ultra-thin, conformal

coating; (b) has a thick, conformal coating; and (c) has a thick, non-conformal coating. The non-

conformal coating in (c) produces a pore with an asymmetric "bottle-neck" shape and higher

permeability than the symmetric pores.

In this study, we used track-etched polycarbonate (PCTE) membranes as the base membranes because their simple pore structure isolates the effects of the surface modification (Fig. 2-2). The pore size of the membranes in this study (400 nm diameter) is similar to that of membranes often used for MD [5]. We used initiated chemical vapor deposition (iCVD) as the hydrophobic surface-modification method [18]. iCVD can deposit polymer films that range from ultra-thin to microns thick. iCVD has been used previously to prepare hydrophobic membranes for MD and other applications [12,19–21]. The iCVD polymer used in this study was a bilayer of poly(divinyl benzene) (pDVB) and poly(1H, 1H, 2H, 2H-perfluorooctyl acrylate) (pC6PFA) (Fig. 2-2d).
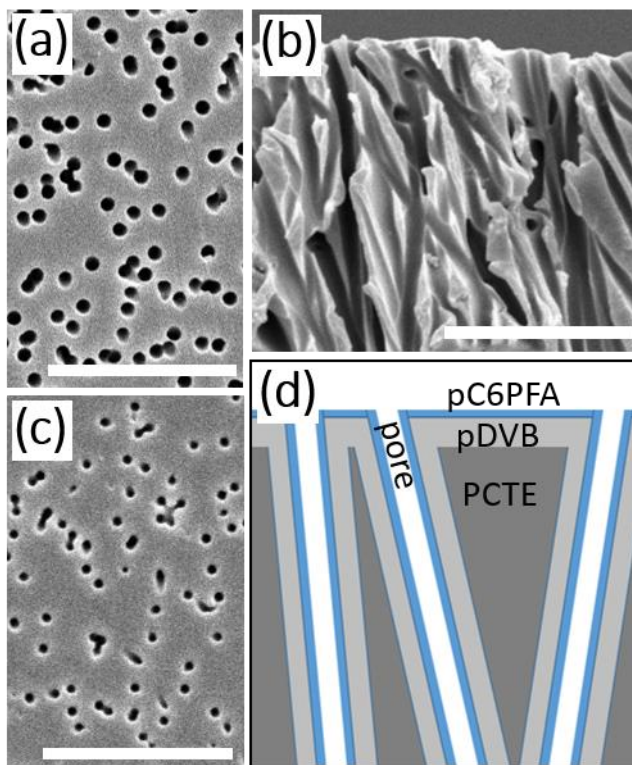
Fig. 2-2. SEM images of the PCTE membrane (a) as-purchased (top view) (b) as-purchased (cross-section) and (c) after iCVD treatment (top view). The scale bars represent 5 µm. (d) is a schematic of the bilayer coating on the PCTE membrane assuming a perfectly conformal film.

2.2. Theoretical background

2.2.1. Pore radius as a function of depth into an iCVD-treated pore

In this study, we use iCVD polymer films to increase membrane hydrophobicity and LEP. These films also decrease pore radius and increase pore asymmetry (Fig. 2-1). Here, we present an equation for the pore radius within membranes treated using iCVD.

iCVD films are grown from vapor-phase monomer and initiating radicals. The monomer and initiating radicals enter the pores from the "top" surface of the membrane, polymerizing on the internal walls [22–24] (Fig. 2-3a). During the deposition, the diffusion rate of the monomer into the pores is fast with respect to the surface reaction rate (low Damköhler number). This is due to the relatively large pore size (~200 nm) and the slow deposition rate. Under this assumption, an equilibrium concentration of monomer is maintained on all surfaces of the membrane. However, unreacted initiating radicals in the gas phase are depleted with increasing depth into the pores. If the rate of polymerization is proportional to radical concentration, film-thickness decreases down the length of the pore, resulting in increased pore radius with increasing distance from the top surface. The rate of depletion of initiated radical with depth depends on a quantity called the sticking coefficient [23]. The sticking coefficient is controlled during iCVD deposition by the fractional saturation of the monomer in the deposition chamber. Low sticking coefficients produce films that are nearly conformal (constant film thickness) (Fig. 2-1a and Fig. 2-1b). Higher sticking coefficients cause steeper depletion and greater asymmetry of the film, producing pores increasingly similar to Fig. 2-1c.
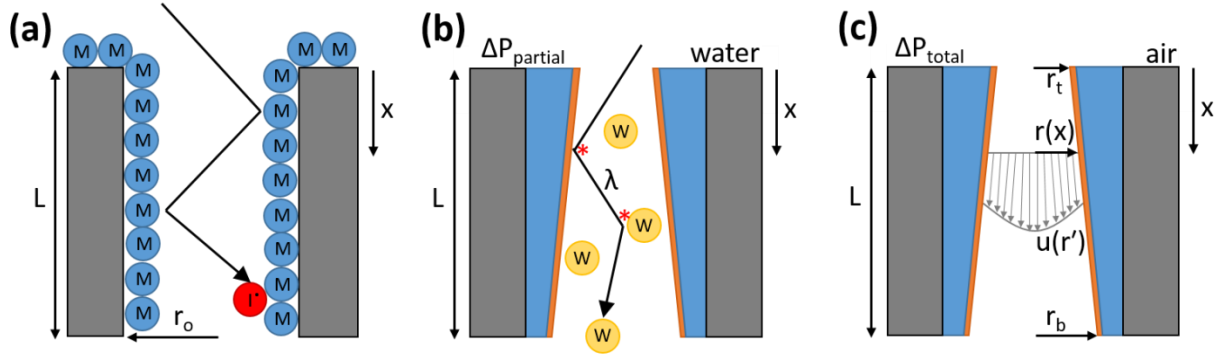
Fig. 2-3. Schematic drawings of a single pore during: (a) iCVD polymer deposition; (b) water vapor diffusion; and (c) forced air flow. (b) and (c) show an iCVD bilayer coating the pore walls. Film thickness is shown to linearly decrease from the top ($x = 0$) to the bottom ($x = L$) of the pore. This is an approximation of the actual pore profile. In (a), M is a monomer and I˙ is an initiating radical. In (b), W is a water vapor molecule.

The step coverage of iCVD polymer films has been studied previously [23]. Step coverage, S_L, is the ratio of film thickness at the bottom and top of a pore. It can be written as

$$S_L = \frac{r_o - r_b}{r_o - r_t} \tag{Eq. 2-2}$$

where r_o is the unmodified pore radius. r_t and r_b are the top and bottom pore radii after iCVD treatment. Analytical modeling [23] has determined that

$$\ln(S_L) = -\frac{3\Gamma}{4}\left(\frac{L}{2r_o}\right)^2 \tag{Eq. 2-3}$$

where Γ is the sticking coefficient of the initiator and L is the length of the pore. For a membrane, L is the membrane thickness multiplied by tortuosity. This model assumes that the monomer and initiating radicals are in the Knudsen diffusion regime within the pore and so collide primarily with the pore walls. This is a reasonable assumption given the low pressure in the iCVD deposition

chamber (< 1 Torr[2]). Increasing the sticking coefficient or increasing the aspect ratio of the pores lowers the step coverage, producing a less conformal coating.

Equation (2-3) can be generalized to describe the step coefficient at any distance x from the top surface of the membrane. S_L is replaced by $S(x)$ which is defined as

$$S(x) = \frac{r_o - r(x)}{r_o - r_t} \tag{Eq. 2-4}$$

where $r(x)$ is the pore radius at distance x from the top of the pore. Using the same analytical model as for Eq. (2-3), $S(x)$ is modeled as

$$\ln(S(x)) = -\frac{3\Gamma}{4}\left(\frac{x}{2r_o}\right)^2 = \left(\frac{x}{L}\right)^2 \ln(S_L). \tag{Eq. 2-5}$$

As x approaches L, $S(x)$ approaches S_L. Combining Eq. (2-4) and Eq. (2-5) and solving for $r(x)$ produces an equation for $r(x)$:

$$r(x) = r_o - S_L^{\left(\frac{x}{L}\right)^2}(r_o - r_t). \tag{Eq. 2-6}$$

r_o, r_t and r_b can be determined using image analysis of SEM images of the top and bottom surfaces of unmodified and iCVD-treated membranes. From these measurements, we can compute S_L and so determine the pore radius, $r(x)$ at any location within the membrane. While the pore profile in Eq. (2-6) is implied in [23], this is the first time it has been calculated explicitly.

2.2.2. Permeability to water vapor diffusion

In an MD system, a partial pressure gradient causes net diffusion of water vapor through the membrane from the feed to the distillate (Fig. 2-3b). The membrane distillation coefficient is the

---

[2] 1 Torr = 133.322 Pa

ratio of specific vapor flux to partial pressure difference across the membrane. This quantity is equivalent to the permeability of the membrane to water vapor diffusion. MD membranes typically have pore sizes ranging from 100 to 450 nm [5]. At this pore size, the mean free path of water vapor, λ, is comparable to the pore radius (Appendix 2-A). This means that the Knudsen numbers, $Kn = \lambda/2r$, is within the transition regime ($0.2 < Kn < 1.0$) in which both continuum and discrete effects are important. Multiple models for gas diffusion in such pores have been proposed [25]. Although it has been met with some criticism [25], the membrane coefficient for MD membranes is often described using the dusty gas model [26]. In the dusty gas model, the total resistance to diffusion is the sum of the resistances to molecular and Knudsen diffusion. This captures the effects of both the intramolecular and the wall collisions expected to occur at these Kn values. In this study, we extend the dusty gas model to describe membranes with pores whose radii vary lengthwise along the pore. This new model is described below with further derivation information in Appendix 2-B.

For $Kn \gg 1$, gas transport is described by Knudsen diffusion. Knudsen permeability, K_k, of a membrane consisting of cylindrical pores of radius, r and length, L can be written as

$$K_k = A_k \frac{cr^3}{L}.$$ (Eq. 2-7)

where pore length, L, is membrane thickness multiplied by tortuosity, and c is the pore-density of the membrane (pores/m^2). Throughout this study, we describe the permeability of membranes with respect to pore density, c, rather than porosity, ε which is often used. Porosity is related to pore density according to $\varepsilon = \frac{n\pi r^2}{A} = c\pi r^2$ where n is the number of pores in the membrane and A is the area of the membrane. All equations for permeability in this study are in units of kg/m^2-Pa-s. In Eq. (2-7), A_k is a constant defined as

$$A_k = \frac{2\pi}{3} \frac{M_w}{RT} \left(\frac{8RT}{\pi M_w} \right)^{1/2} \qquad \text{(Eq. 2-8)}$$

where R is the universal gas constant (J/mol-K), T is temperature (K), and M_w is the molecular weight of water (g/mol).

When $Kn<<1$, gas transport in the pores is described by molecular diffusion. Permeability to molecular diffusion can be written as

$$K_d = A_d \frac{cr^2}{L} \qquad \text{(Eq. 2-9)}$$

where A_d is a constant defined as

$$A_d = \frac{\pi M_w}{RT} \frac{PD}{p_a}. \qquad \text{(Eq. 2-10)}$$

P is the total pressure inside the pore (Pa), D is the water diffusion coefficient (m^2/s) and p_a is the air pressure within the pore (Pa) [26].

At transition values of Kn, a model for permeability must be interpolated to combine Knudsen permeability (Eq. (2-7)) and molecular diffusion (Eq. (2-9)). In the dusty gas model, these two mechanisms are assumed to occur in series [26]. This means that the resistance from intramolecular and molecule-wall collisions are additive. The equation for dusty gas model permeability, K_c, is

$$K_c = [K_k^{-1} + K_d^{-1}]^{-1} = \frac{A_d A_k}{A_d + A_k r} \frac{cr^3}{L}. \qquad \text{(Eq. 2-11)}$$

The physical basis for the mechanisms being in series is still under debate [25]. However, Eq. (2-11) predicts the expected limiting behavior: As r approaches zero ($Kn >>1$), K_c approaches K_k. As r becomes very large ($Kn<<1$), K_c approaches K_d. At intermediate values of Kn, both sources of resistance are significant and K_c is less than both K_k and K_d.

K_c assumes cylindrical pores with constant radius, r. Due to the iCVD coating, the membranes in this study have pores that are asymmetric, with the pore radius varying with distance from the surface of the membrane. We have not seen analysis of the permeability of such pores in the literature so we derive new equations. If the pores have radii that vary with distance, x, from the membrane surface, the dusty gas permeability becomes

$$K_e = \frac{L}{\int_0^L \frac{1}{K_c(x)} \partial x} \qquad \text{(Eq. 2-12)}$$

where K_c is a function of x. This approach assumes that changes in r with respect to x occur over length scales much larger than r. It also assumes that the mean free path of the gas is small compared to the rate of variation of r with respect to x.

A closed-form solution for K_e is not available when $r(x)$ is defined by Eq. (2-6). However, a closed-form solution would be useful to build intuition about the system. One such solution can be obtained if we approximate $r(x)$ as varying linearly in x as it appears in Fig. 2-3. Analysis of the errors introduced by this approximation is found in Appendix 2-C. In a linear approximation, $r(x)$ is described by

$$r(x) = r_t + \frac{r_t(a-1)}{L} x \qquad \text{(Eq. 2-13)}$$

where a is a measure of asymmetry defined as the ratio of the radius at the bottom of the pore (r_b) and the radius at the top of the pore (r_t) so that $a = r_b/r_t$. The pore radius is always larger at the bottom of the pore so a is always greater than one. With this definition of $r(x)$, the dusty gas permeability of a membrane is given by

$$K_a = \frac{2a^2 A_d A_k}{A_d(a+1) + 2aA_k r_t} \frac{cr_t^3}{L}. \qquad \text{(Eq. 2-14)}$$

2.2.3. Permeability to forced air

Forced air permeability tests (Fig. 2-3c) are significantly faster (minutes rather than hours) than MD tests and need significantly smaller membrane samples. This makes it possible to test more membranes than could be tested in an MD system. In this study, we use MD tests to verify that the iCVD coating effectively increases LEP and produces MD vapor flux in the expected range. We use forced air permeability tests to go into greater detail, analyzing permeability for a series of nine membranes with varying pore size and asymmetry. We use the trends from these tests to infer MD performance at higher levels of asymmetry.

Both the forced air and MD system tests have Knudsen numbers in the transition diffusion regime (Appendix 2-A). A disadvantage of using forced air as an experimental system is that the transition regime for forced air involves different transport mechanisms than the transition regime for concentration-driven diffusion. For forced air, there is no concentration gradient of the gas, so molecular diffusion is not present. However, there is net viscous flow which is not present in the MD system. We thus need a separate set of equations to describe the permeability of the membranes to forced-air.

A framework for forced gas flow at transition Knudsen numbers is found in ultra-thin film gas lubrication theory ("slip flow") (Fig. 2-3c) [27]. Other theories have also been proposed with different constants but the same form [25]. Ultra-thin film gas lubrication theory has been applied for gas-lubricated bearings and other hardware applications [28–31]. We have not seen it widely applied to describe gas flow through membranes. Slip flow assumes locally fully developed,

41

pressure-driven flow with viscous slip at the interface of the pore wall. In this study, we extend the slip-flow model to membranes with non-uniform pore radius.

At low Reynolds numbers, locally fully-developed, pressure-driven flow through cylindrical pores of radius, r and length, L, is described by Poiseuille flow. Permeability to this flow can be written as

$$K_p = A_p \frac{cr^4}{L} \tag{Eq. 2-15}$$

where K_p is Poiseuille permeability. A_p is a constant defined as

$$A_p = \frac{\pi \rho}{8\mu} \tag{Eq. 2-16}$$

where ρ is gas density (kg/m^3) and μ is gas dynamic viscosity (kg/m-s).

Poiseuille flow assumes a no-slip boundary condition on the pore walls. However, at low pressures or small pore sizes, pore size becomes comparable in magnitude to the molecular mean free path of the gas. In this regime, viscous slip becomes significant, and the boundary condition on the walls becomes [27]

$$u(r) = -\xi \frac{\partial u}{\partial r'} \tag{Eq. 2-17}$$

where ξ is the coefficient of slip, r' is the distance from the center-line of the pore and $u(r')$ is velocity along the axis of the pore. ξ has been found to be proportional to the molecular mean free path, λ (m), with a coefficient dependent on the properties of the wall. To first approximation, $\xi = \lambda$ and this is the form that we use in this study.

Using this boundary condition, permeability, K_s, of the membrane can be expressed as

$$K_s = A_p \left(1 + \frac{4\lambda}{r}\right) \frac{cr^4}{L}. \qquad\qquad \text{(Eq. 2-18)}$$

The addition of the *4λ/r* term, caused by slip along the pore walls, increases total permeability. As

r becomes large relative to the mean free path (*Kn*<<1), the slip term because insignificant.

Alternative models to describe pressure-driven gas flow for transition *Kn* have been proposed [25].

The general form of these models ($K = ar^4 + br^3$) is consistent across models.

K_p and K_s both assume cylindrical pores with constant radius, *r*. Since we are interested in iCVD-

treated pores which are asymmetric, we derive new equations for slip flow in an asymmetric pore.

If pore radius varies along the length of the pore, slip-flow permeability becomes

$$K_t = \frac{L}{\int_0^L \frac{1}{K_s(x)} \partial x} \qquad\qquad \text{(Eq. 2-19)}$$

where $K_s(x)$ is a function of *x*.

A closed-form solution for K_t is not available when *r(x)* is as defined by Eq. (2-6). However, a

closed-form solution can be obtained by approximating *r(x)* as varying linearly in *x* according to

Eq. (2-13). Using this equation for *r(x)*, slip-flow permeability, K_m, for a membrane with linearly

varying asymmetric pores is

$$K_m = A_p \frac{64a^2}{\frac{a^2}{a-1}b^3 \ln\frac{a(4+b)}{4+ab}+8b(a+1)-4b^2a} \frac{cr_t^4}{L} \qquad\qquad \text{(Eq. 2-20)}$$

where $b = r_t/\lambda$ and r_t is the pore radius at the top of the pore.

For both K_m and K_a, the numerator is proportional to a^2 and the denominator is approximately

proportional to *a*. Thus, for constant r_t, *c* and *L*,

$$K_a \sim aK_c \qquad\qquad \text{(Eq. 2-21)}$$

and

$$K_m \sim aK_s. \tag{Eq. 2-22}$$

As a increases, K_a and K_m increase at the same rate, becoming increasingly larger than K_c and K_s. In this analysis, we assume constant r_t because, when developing membranes for MD, the value of r_t is often constrained to ensure adequate LEP. Eq. (2-21) and Eq. (2-22) are essential to our understanding of how asymmetric iCVD films affect the permeability of MD membranes. It is also notable that Eq. (2-21) and Eq. (2-22) have the same form. This indicates that permeability to water vapor diffusion and permeability to forced air have the same dependence on asymmetry. Thus, findings for forced air should extend to water vapor flux.

2.3. Materials and methods

2.3.1. Membrane preparation

Ten iCVD-treated membranes were prepared for this study (Table 2-1). Membrane M0 was used to quantify MD performance. Membranes M1 – M9 were used to analyze the relationship between iCVD coating parameters and permeability to forced air. The base membranes in this study were polyvinylpyrrolidone (PVP) treated, hydrophilic, track-etched polycarbonate membranes (Sterlitech, PCT0214220) (Fig. 2-2). Pore size (diameter) was 400 nm. Total membrane thickness was 10 µm (24 µm for membrane M0 only). Pore density was 1.1×10^{12} pores/m^2 (1.5×10^{12} pores/m^2 for membrane M0 only).

iCVD was used to conformally coat the base membranes with pDVB-pC6PFA bilayers (Fig. 2-3). The bilayers consist of a pDVB base layer and a pC6PFA top-layer. The cross-linking polymer, pDVB, forms a robust layer at the interface of the membrane of tunable thickness. The pC6PFA

forms an ultra-thin (<10 nm) layer on top of the pDVB to achieve a high contact angle with water (110 - 135 °). pDVB-pC6PFA bilayers have been studied but have not been applied to MD membranes [32,33]. Previously, iCVD poly(1H, 1H, 2H, 2H-perfluorodecyl acrylate) (pPFDA) films have been used for hydrophobic surface modification. However, pPFDA, having eight-carbon perfluoro pendent groups, has been banned from future commercial use due to environmental concerns [34]. For this reason, alternative chemistries are currently being sought [35]. The pDVB-pC6PFA bilayer, with six-carbon perfluoro side chains, has a lower bioaccumulation factor than pPFDA, and so is an environmentally friendly alternative.

Both layers were deposited in a custom-built reaction chamber. The chamber was cylindrical (height = 38 mm, diameter = 246 mm). It contained an array of 14 resistively heated parallel filaments (80% Ni, 20% Cr). Membranes were taped to a cooled stage (recirculating chiller/heater, NESLAB). The total pressure inside the chamber was maintained at a constant value using a mechanical pump (45 CFM pumping speed, Alcatel).

To produce the pDVB layer, tert-butyl peroxide (TBPO, Sigma-Aldrich, 97%) initiator and DVB (Sigma-Aldrich, 80%) monomer were introduced into the chamber. The TBPO was at room-temperature and was introduced at a rate of 1.0 sccm[3]. The DVB was heated to 60 °C and introduced at a rate of 0.5 sccm. The stage was maintained at 30 °C, and the total pressure in the vacuum chamber was 800 mTorr. This resulted in a fractional saturation of the DVB of 0.3. A piece of silicon wafer was treated along with the membranes. Film thickness on the silicon was

---

[3] sccm = standard cubic centimeters per minute (cm^3/min at standard temperature and pressure).

monitored *in situ* using a laser interferometer. The deposition time of this layer determined the film thicknesses.

The pC6PFA layer was deposited directly on top of the pDVB film using the iCVD closed-batch configuration described previously [36]. The closed-batch configuration makes it easier to control film thickness for monomers that polymerize rapidly such as C6PFA. C6PFA monomer (Sigma-Aldrich, 97%,) and TBPO (Sigma-Aldrich, 97%) were used. The chamber was initially evacuated. The TBPO initiator was fed into the evacuated chamber at room temperature until the total pressure reached 110 mTorr. The C6PFA monomer was heated to 80 °C and fed into the chamber until the total pressure in the chamber was 190 mTorr. The stage was maintained at 25 °C. After filling the chamber with initiator and monomer, all valves were closed and the system was let rest for 2 minutes to allow mixing. The filament array was then turned on for 15 minutes, allowing the film to form. Next, the filaments were turned off and the chamber was evacuated. When the system had cooled, the chamber was refilled with initiator and monomer and the deposition process was repeated for a total of two times for membranes M1 – M9 and nine times for membrane M0. Depositing multiple rounds of C6PFA increases the pC6PFA layer thickness, reducing the possibility of defects due to thinness of the coating.

Membranes M0 – M9, are described in Table 2-1. The deposition parameters for Membranes M1 – M9 were identical with the only difference being the deposition time of the pDVB layer. By varying deposition time, the pDVB layer thickness varied across the series. The thickness of pC6PFA layer was held constant. This was done because the properties of pC6PFA are highly sensitive to film thickness [32]. Below a certain thickness, the film is not complete and surface-

energy is higher than it would be for a complete film. Above a certain thickness, the film has side-chain rearrangement when in contact with water, increasing contact angle hysteresis [32,33]. By using the pDVB layer to control pore size and keeping the pC6PFA layer thickness constant, we varied pore size/asymmetry while maintaining constant surface properties. While total bilayer thickness varied across membranes, the deposition parameters were identical so all membranes had the same step coverage. Asymmetry, ($a = r_b/r_t$), increased with film thickness. Membrane M0 had the same deposition parameters as M1 – M9 but with a thicker pC6PFA layer.

Table 2-1. The ten membranes prepared for this study. All membranes have step coverage, $S_L = 0.25$. Asymmetry, a, varies with film thickness. Permeability refers to permeability to air for M1 – M9. It refers to the membrane distillation coefficient (permeability to water vapor diffusion) for M0. An uncoated PCTE membrane is included for comparison. Average pore radius uncertainty was +/- 14 nm. Average permeability uncertainty was +/- 0.68×10^{-6} kg/m^2-Pa-s.

Name	Top pore radius, r_t (nm)	Bottom pore radius, r_b (nm)	Asymmetry, $a = r_b/r_t$	Permeability (kg/m^2-Pa-s)
Uncoated PCTE	200	200	1.0	1.36×10^{-5}
M1	192	198	1.0	8.58×10^{-6}
M2	183	196	1.1	6.93×10^{-6}
M3	175	194	1.1	9.68×10^{-6}
M4	166	192	1.2	7.15×10^{-6}
M5	158	189	1.2	6.93×10^{-6}
M6	149	187	1.3	6.22×10^{-6}
M7	133	183	1.4	1.49×10^{-6}
M8	116	179	1.5	3.23×10^{-6}
M9	99	175	1.8	2.33×10^{-6}
M0	180	195	1.1	1.51×10^{-6}

2.3.2. SEM imaging and pore size analysis

The pore sizes of the membranes were determined using image analysis of 445 µm^2, 5 nm/pixel resolution SEM images of the top and bottom surfaces of the membranes. This made it possible to characterize the asymmetry of the pores in a way that bulk characterization would be unable to do.

SEM images were collected using a JEOL 6010a SEM microscope with an acceleration voltage of 5 keV. All SEM samples were sputtered with gold to improve conductivity during imaging. The thickness of this gold layer was taken into account when calculating pore sizes. SEM images were read into MATLAB and converted to black and white using a threshold determined using Otsu's method. Pores were identified and their areas were measured using MATLAB's regionprops command. Pores with areas smaller than 500 pixels were discarded. The remaining pores were placed in a histogram with bin-size of 5 nm. The average (mode) pore size was determined by identifying the bin with the most pores and calculating a radius assuming a circular pore-shape. Similar analysis using curve-fitting instead of mode value to determine average pore size, has been used by other researchers [37].

The pore size distribution for membrane M1 is shown in Fig. 2-4 as a representative example. The inset shows a section of the membrane with the centroids of pores marked. Some overlapping pores can be seen which produce larger openings at the surface of the membrane. However, these pores split from each other just below the surface of the membrane. This creates regularly-sized pore openings at the location where they split. Because of this, we expect that these "double pores" do not have a significant effect on LEP or permeability. More work is needed to determine their exact effect.
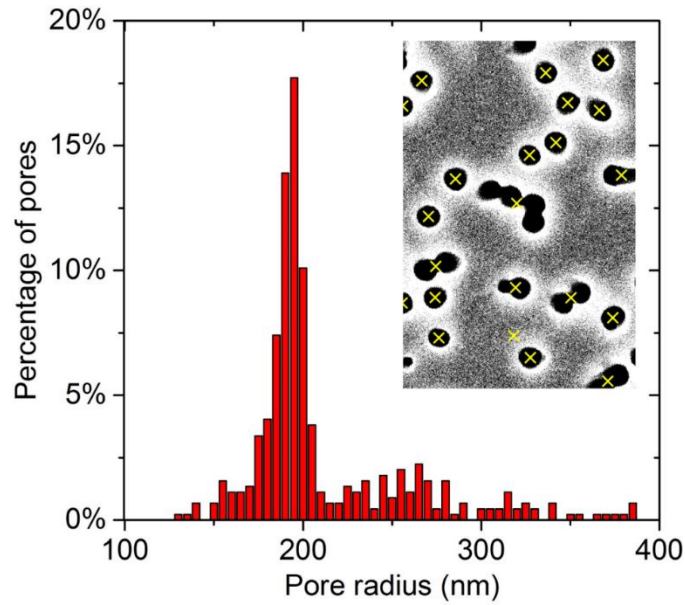
Fig. 2-4. The pore size distribution of a 445 μm^2 section of an iCVD-treated membrane as determined using analysis of an SEM image. The inset is a small section of the processed image.

This method for determining pore size introduces uncertainty due to the small areas of the images sampled. To reduce this uncertainty in our results, we used the pore radii measured using image analysis to determine the ratio between the deposition rates on the top and bottom surfaces of the PCTE membranes and the deposition rate on the pieces of silicon wafer coated along with the membranes. We used these ratios to calculate the expected film thickness on the membranes, thereby smoothing out errors caused by regional differences. We found that the deposition rates on the top and bottom surfaces of membranes were 4.21% and 1.06% the rate on the silicon. This is a larger difference than expected and was likely caused by the PCTE membranes losing contact with the cooled stage during the deposition. This would cause the membranes to overheat, reducing the fractional saturation of the monomer and slowing polymer film formation. All pore sizes reported in this study were calculated using these averaged deposition rates. The error-bars for pore size account for the average error between the calculated and measured pore size values.

2.3.3. Angle resolved X-ray photo spectroscopy

Angle resolved X-ray photo spectroscopy (ARXPS) data were obtained using a Surface Science Instruments SSX-100 with an operating pressure of ~2×10^{-9} Torr. A 4 keV Argon ion source was used with a beam current of 1 mA. We used angling of the beam to measure the ratio of the F_{S1} and C_{S1} signals at a range of depths from the top and bottom surfaces of the membrane (where top is the direction from which the iCVD coating was deposited). Based on the inelastic mean free path of 2.4 nm, the depth of penetration of the X-ray beam was calculated to be 7.2, 6.2, 4.6 and 2.5 nm at incidence angles of 0, 30, 50 and 70 °, respectively. Measurements taken at each angle indicated the strength of the fluorine signal to each of these depths. F_{S1}/C_{S1} for pure pC6PFA is 1.3 based on calculation from its chemical structure. Values below this indicate that the coating is incomplete when measured to that depth.

2.3.4. Contact angle

Advancing contact angles were measured using a goniometer equipped with an automatic dispenser (model 590, Ramé-Hart). DropImage software was used to acquire images for measurement. A 3 µL drop of room-temperature DI water was first placed onto the membrane surface. Water was then added to this drop in increments of 2 µL, and the angle between the advancing drop and the membrane surface was measured 100 ms after each addition.

2.3.5. Liquid entry pressure

Liquid entry pressure (LEP) of some of the membranes was measured with a custom system similar to ones used previously [12,38,39]. A pristine sample of the membrane was held in a 13 mm syringe membrane holder (GE healthcare biosciences). The membrane was exposed to the saline

solution (35 g/L, NaCl) on one surface and deionized (DI) water on the other. A syringe pump (PHD 22/2000, Harvard apparatus) incrementally increased the pressure of the saline solution against the membrane. After each increase, the pressure was held constant for 12 seconds. A USB pressure transducer (PX409, Omega) monitored the pressure difference across the membrane. LEP is defined as the pressure at which liquid first passes through the membrane. The deionized water reservoir was monitored using an electrical conductivity meter (Oakton Con6 Probe). LEP was detected by an increase in the electrical conductivity of the reservoir corresponding to a rate of 0.3 µL/s of saline entering the reservoir. This was the smallest rate that we could measure with our system. For all LEP and air permeability testing, the active area of the membrane was 0.64 cm^2. Three samples from each membrane were tested for LEP.

2.3.6. Permeate gap membrane distillation

Permeate gap membrane distillation (PGMD) was conducted using a custom-built lab-scale system. The active area of the membrane was rectangular with a surface area of 21 cm^2. The feed solution contained DI water and NaCl at a concentration of 35 g/L. Feed and distillate flowed past the membrane at a rate of 680 L/hr. Distillate temperature was maintained at 20 °C. Feed temperature was 40 – 60 °C. Experiment duration was 18 hours. Water vapor flux from feed to distillate ranged from 8.4 to 18.6 LMH. When calculating the membrane distillation coefficient, temperature polarization was taken into account using previous calibrations [40].

2.3.7. Forced air permeability

Permeability to forced air was measured using the same system as was used to measure liquid entry pressure. The syringe was filled with air and the air was pushed through the membrane at a constant rate of 210 mL/min. The equilibrium pressure measured across the membrane was used

to calculate the air permeability. Three samples from each membrane were tested for air permeability.

2.4. Results and discussion

2.4.1. Permeate gap membrane distillation

We prepared one membrane to test in a permeate gap membrane distillation (PGMD) system (Membrane M0, Table 2-1). This membrane was used to determine the effects of a ~20 nm iCVD pDVB-pC6PFA bilayer film on MD membrane permeability and LEP. Image analysis determined that the bilayer was 20 nm thick at the top of the membrane and 5 nm thick at the bottom of the membrane. This corresponds to step coverage, $S_L = 0.25$ and asymmetry, $a = 1.1$. Angle resolved XPS (ARXPS) was used to determine the contribution of the pC6PFA to the total bilayer thickness (Fig. 2-5). On the top surface, the ratio of the F_{S1} and C_{S1} signals stayed above the polymer's elemental ratio of 1.3 even at the maximum probing depth of 7.2 nm. This indicates that the pC6PFA layer on the top surface is at least 7.2 nm thick. On the bottom surface, the ratio of F_{S1} and C_{S1} signals approached 1.3 at the 2.5 nm probing depth. This indicates that the pC6PFA layer is slightly thinner than 2.5 nm on the bottom surface.
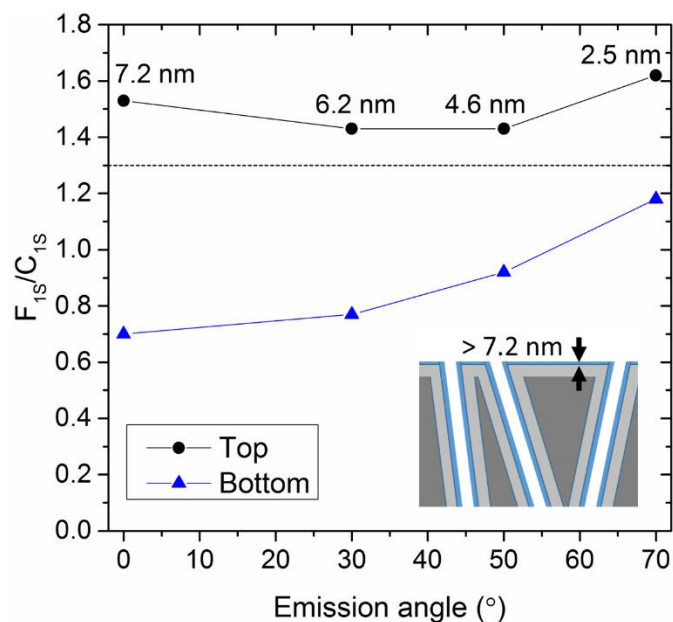
Fig. 2-5. The ratio of the F_{S1} and C_{S1} ARXPS signals at four sampling depths from the top and bottom surfaces of Membrane M0. The inset shows a schematic of the area near the membrane's top surface. The thickness of the pC6PFA film is indicated. The layer below the pC6PFA is the pDVB.

2.4.1.1. Resistance to wetting

We first verified that the pDVB-pC6PFA bilayer on Membrane M0 increased LEP enough to prevent wetting. This was especially important because bilayer polymer films of this composition have never before been applied to MD membranes. We measured the apparent advancing contact angle (ACA) and LEP of a PCTE membrane as-purchased, after application of pDVB and after applications of the pDVB-pC6PFA bilayer (Table 2-2). This last sample was taken from Membrane M0. Measurements showed that Membrane M0 has an LEP to water that is suitable for MD. The pDVB layer alone does not raise the LEP to a value that we would expect to have successful MD performance.

Table 2-2. Advancing contact angle (ACA) and liquid entry pressure (LEP) of PCTE membranes as-purchased, after application of pDVB and after application of the full pDVB-pC6PFA bilayer.

Membrane	r_t (nm)	ACA (°)	LEP (kPa) (measured)	LEP (kPa) (Y-L)
As-purchased PCTE	200	91	0	13
pDVB	193	103	53	168
pDVB-pC6PFA bilayer (Membrane M0)	180	124	276	447

We compared the measured LEP values to the values calculated from the Young-Laplace model (Eq. (2-1)). In this calculation, we assumed surface tension, $\gamma = 0,072$ N/m. This may introduce errors as surface tension varies depending on the salinity of the liquid [41]. We found that for the three membranes in Table 2, measured LEP was less than the predicted values. This may be due to the contact angle with water within the pores being lower than the value measured on the membrane surface. However, accurately predicting LEP for membranes has been shown to be difficult, even for membranes with relatively simple pore structures [42]. It is clear from this data that the iCVD pDVB-pC6PFA bilayer is effective at increasing LEP to a value high enough to support MD.

With LEP verified, Membrane M0 was tested in a permeate gap membrane distillation (PGMD) system to treat 35 g/L of NaCl solution. This test showed that the iCVD-treated PCTE membrane had 99.98% salt rejection. This indicates that the membrane did not wet in the MD system. This is the first demonstration of a pDVB-pC6PFA bilayer successfully being used to prepare a hydrophobic membrane with adequately high LEP for MD.

2.4.1.2. Permeability to water vapor (Membrane distillation coefficient)

The PGMD system was also used to determine the permeability to water vapor (membrane distillation coefficient) of Membrane M0 (Fig. 2-6). The measured membrane distillation coefficient is slightly lower than the values for other membranes currently used for MD [5]. This is largely explained by the significantly lower porosity (~10% versus >70%) of the PCTE membranes.
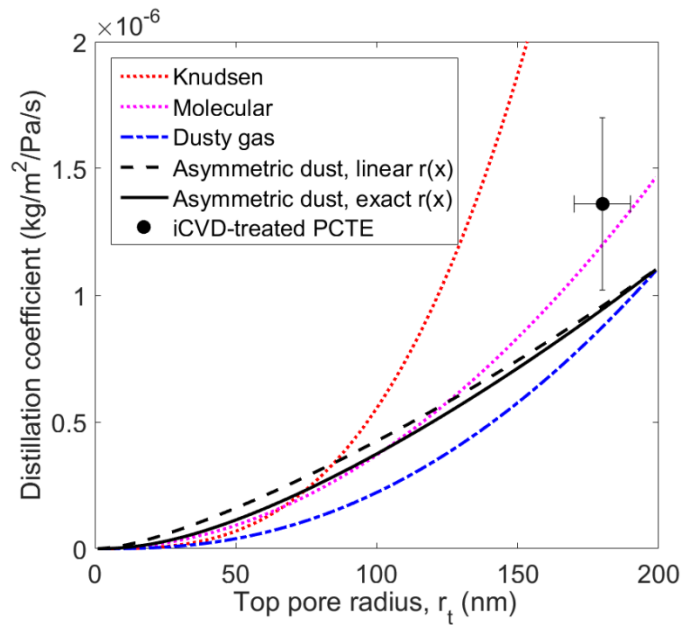
Fig. 2-6. Membrane distillation coefficient of Membrane M0 in the PGMD system for 40 – 60 ° feed temperature and 20 ° distillate temperature. Feed was saline solution (35 g/L, NaCl). Models for permeability to water vapor diffusion are also shown. The two asymmetric models assume S_L = 0.25.

In Fig. 2-6, theoretical models for water vapor permeability are presented along with the experimental data. Knudsen diffusion (Eq. (2-7)) predicts the highest values of permeability, followed by molecular diffusion (Eq. (2-9)), and the dusty gas model (Eq. (2-11)). The parameter values used for these models are based on measurements of the system and can be found in

Appendix 2-D. Two versions of the asymmetric dusty gas models [Eq. (2-12) and (Eq. (2-14)] are also shown. Both intersect the symmetric dusty gas model at $r_t = 200$ nm and $r_t = 0$. Between these extremes, the asymmetric dusty gas models predict higher permeability than the symmetric version and decrease at a more constant rate with respect to pore radius.

Because the Knudsen number for the system is in the transition regime, we expected that the experimental data for Membrane M0 would fall on the curve for the exact asymmetric dusty gas model (Eq. (2-12)). However, the measured membrane distillation coefficient is closer to the molecular diffusion curve. This suggests that intramolecular collisions dominate transport with minimal additional losses from collisions with the pore walls. The effect of asymmetry of the pores is not clear from this data. The molecular diffusion and dusty gas model curves are close enough to each other that more data would be needed to definitively distinguish if one describes the membrane better than the other. The PGMD data thus serves the purpose of verifying that our membrane characterizations and general understanding of diffusion permeability are reasonable. Despite the uncertainty of the exact model, we do our analysis of permeability at high asymmetries (Section 4.3), assuming the dusty gas model is a descriptive model. We believe that the conclusions that we draw using the dusty gas model will extend to improved diffusion models as they arise.

2.4.2. Effects of iCVD film thickness on forced-air permeability

To analyze the effects of iCVD film thickness and asymmetry, we prepared an additional set of nine membranes (M1 – M9, Table 2-1) to test for permeability to forced air. iCVD bilayer thickness for the series ranged from 8 to 101 nm at the top of the pores and from 2 to 25 nm at the bottom of the pores. Step coverage was constant across membranes ($S_L = 0.25$), The range of

bilayer thicknesses resulted in asymmetry, $a = r_b/r_t$, ranging from 1.0 for the thinnest film to 1.8 for the thickest film. The contribution of the pC6PFA layer was estimated to be ~1.6 nm on the top surface and ~0.55 nm on the bottom surface based on having two coats of closed-batch pC6PFA compared to the nine coats on the M0 membrane.

2.4.2.1. Pore profiles

The profiles of the pores in Membranes M1 – M9 calculated from Eq. (2-6) are shown in Fig. 2-7. Linear profiles calculated using Eq. (2-13) are also shown.
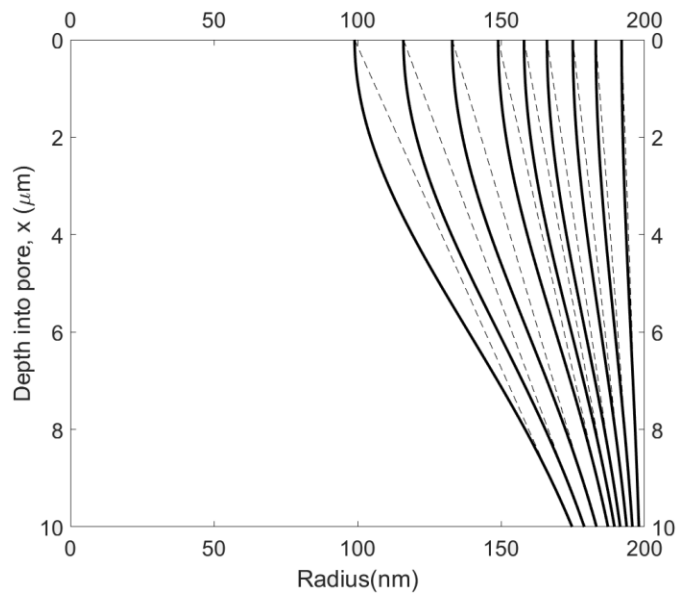
Fig. 2-7. Calculated pore profiles for Membranes M1 to M9 (M1 has the largest pore radius, M9 has the smallest). The solid lines are the exact profiles calculated using Eq. (2-6). The dashed lines are the linear approximations calculated using Eq. (2-13). The scales on the x and y axes are very dissimilar.

2.4.2.2. Forced air permeability

Fig. 2-8 shows the forced air permeability of the series of iCVD-treated membranes and an unmodified (symmetric) PCTE membrane. Four theoretical models for permeability are also shown. The measured parameter values used for the models can be found in Appendix 2-D. The model predicting the lowest permeability is Poiseuille flow (Eq. (2-15)) which has a no-slip boundary condition along the pore walls. The next lowest curve is for slip-flow (Eq. (2-18)). Viscous slip increases the average velocity in the pore, increasing permeability. The two remaining models are for slip-flow in asymmetric pores [Eq. (2-19) and Eq. (2-20)]. The asymmetric slip-flow curves intersect symmetric slip-flow at $r_t = 200$ nm and $r_t = 0$ nm. At all other points, the magnitude of the asymmetric model is greater than the symmetric model.
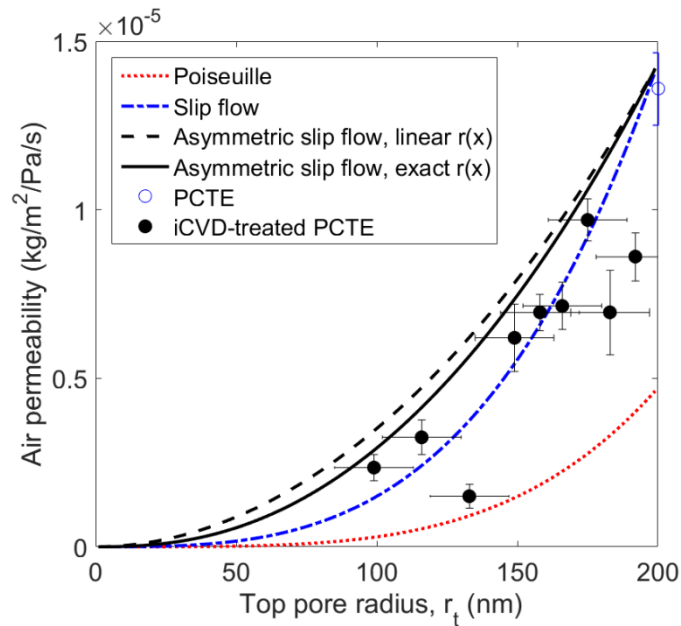
Fig. 2-8. Permeability to forced air for membranes M1 to M9 and an untreated PCTE membrane. The two asymmetric models assume $S_L = 0.25$.

The untreated PCTE membrane, as expected, falls on the symmetric slip-flow curve. The iCVD-treated membranes, which are all asymmetric, have slightly lower permeability than the asymmetric slip-flow model. There are also a few outliers with permeability significantly below the other membranes. The theoretical curves in Fig. 2-8 do not predict a large effect of asymmetry on permeability. This is reflected in the data. However, it is clear from Fig. 2-8 that permeability is strongly dependent on pore radius. The iCVD-treated membrane with the highest permeability is still 29% less permeable than the uncoated PCTE membrane. This experimental finding is consistent with the theoretical models.

2.4.3. Extension to greater asymmetry

The membranes discussed in Section 4.1 and Section 4.2 had mild step coverage ($S_L = 0.25$) and maximum asymmetry of only $a = 1.8$. We extend our analysis to predict how the effects of asymmetry develop for more extreme geometries. We do this to determine if there is a set of membrane and iCVD parameters that could be used to significantly improve the water vapor permeability possible at a constant value of LEP.

To determine the effect of an asymmetric film on membrane permeability, we must compare membranes with the same value of LEP (and so the same r_t). We consider the ratio in permeability between a membrane of starting pore radius, $r_o = r_f$, and film thickness, $t = (r_f - r_t)$ (similar to Fig. 2-1b and Fig. 2-1c) and a membrane with $r_o \approx r_t$ and top film thickness $t << r_t$. (similar to Fig. 2-1a). We assume that the porosity of the unmodified membrane is preserved regardless of the value of r_o. This means that pore density is inversely proportional to r_o.

If this is the case, a membrane with $r_o \approx r_t$ and top film thickness $t << r_t$ has permeability

$$K_t \sim c_t g(r_t) \sim \frac{g(r_t)}{r_t^2}$$ (Eq. 2-23)

where $g(r_t)$ is a polynomial of r_t, and c_t is pore density for $r_o = r_t$.

In Eq. (2-21) and Eq. (2-22), we observed that permeability increases approximately proportionally to the value of asymmetry, a. Permeability of a membrane of starting pore radius, $r_o = r_f$, and film thickness, $t = (r_f - r_t)$ is thus described by

$$K_f \sim c_f a g(r_t) \sim \frac{ag(r_t)}{r_f^2}$$ (Eq. 2-24)

where c_f is pore density for $r_o = r_f$. The ratio in permeability for these two membranes is then

$$R \sim \frac{K_f}{K_t} = \frac{a}{f^2}$$ (Eq. 2-25)

where $f = r_f/r_t$. A larger value of f corresponds to a thicker iCVD film. By rearranging Eq. (2-2), we determine that

$$a = f - (f - 1)S_L.$$ (Eq. 2-26)

Eq. (2-25) can thus be rewritten as

$$R \sim \frac{f - (f-1)S_L}{f^2}.$$ (Eq. 2-27)

According to Eq. (2-27), as S_L approaches one (Fig. 2-1b), R approaches $1/f^2$. As S_L approaches zero (Fig. 2-1c), R approaches $1/f$. This indicates that increasing film thickness decreases permeability regardless of the level of asymmetry of the iCVD film. This is shown in Fig. 2-9a. The ratio of asymmetric and symmetric dusty gas models [(Eq. (2-12) and Eq. (2-11)], evaluated for $r_t = 200$ nm, is shown along with the curves for $1/f$ and $1/f^2$. The exact solution appears to be bounded by these simple functions.
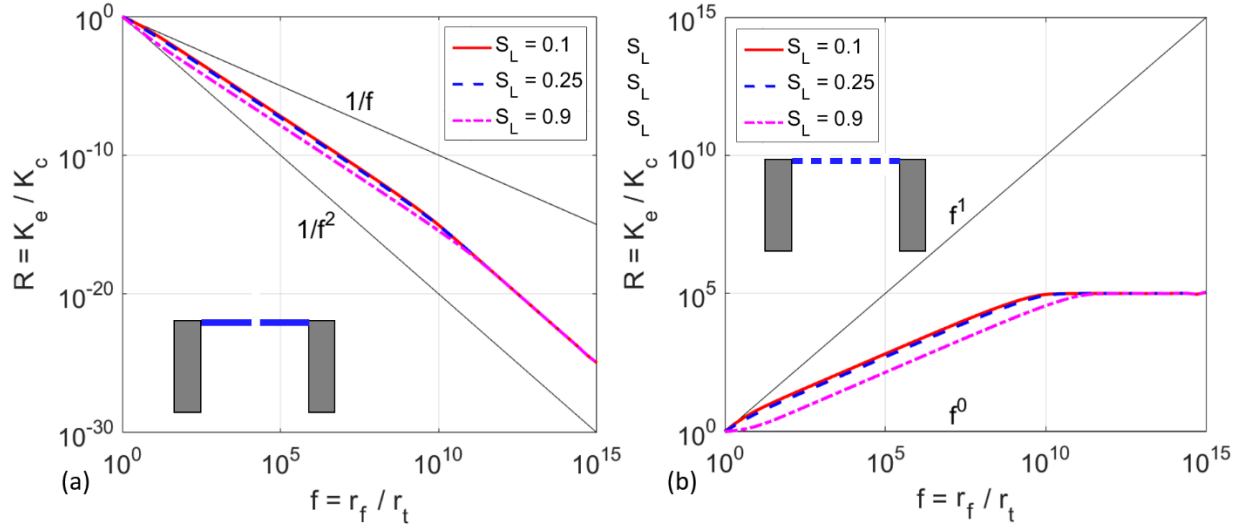
Fig. 2-9. The ratio of asymmetric dusty gas permeability (Eq. (2-12)) and symmetric dusty gas permeability (Eq. (2-11)) with respect to the ratio of starting pore radius (r_f) to iCVD-coated pore radius (r_t). For all calculations, $r_t = 200$ nm. In (a), porosity is preserved and pore density decreases with increasing r_f (inset). In (b), porosity is preserved, but c is also preserved by having multiple pore openings of radius, r_t, within each original pore (inset).

This analysis shows that increasing iCVD film thickness decreases permeability regardless of whether the pore has a "bottle-neck" shape. Based on Eq. (2-21) and Eq. (2-22), it appears that this finding holds across different models for permeability. To maximize permeability for a given value of LEP using iCVD, the best option is to start with a base membrane with smallest possible pore size, $r_o \approx r_t$ and deposit the thinnest iCVD film that effectively reduces surface energy. However, if alternative surface-modification methods are available that can decrease pore radius to the desired r_t without decreasing pore density (Fig. 2-9b), then permeability can increase at constant LEP. If $r_f > r_t$, but there are multiple pore openings within the area originally occupied by a single pore, pore density can remain constant while maintaining porosity. In this case $c_f = c_t$, and

$$R \sim f - (f - 1)S_L \qquad \text{(Eq. 2-28)}$$

In this case, as S_L approaches zero, R approaches f. As S_L approaches 1, R approaches 1. Gains in permeability on the order seen in Fig. 2-9b could valuably improve MD system efficiency. This could potentially be achieved using free-standing, iCVD polymer films [43]. Other methods of producing such composite membranes could also be explored.

2.5. Conclusions

In this study, we analyzed the effects of iCVD surface-modification on the permeability and LEP of MD membranes. We did this through experimentation and through the development of new models for permeability of asymmetric membranes. We found that asymmetry of the iCVD film cannot be used to improve membrane permeability at constant LEP. Key findings are as follows:

- The iCVD pDVB-pC6PFA bilayer successfully increases the LEP of a PCTE membrane to a level adequate to distill water in a PGMD system. This demonstrates that pDVB-pC6PFA bilayers could be a viable alternative to pPFDA for preparing MD membranes.

- The permeability to water vapor of an iCVD-treated PCTE membrane in a PGMD system was on the same order of magnitude as the dusty gas and the molecular diffusion models for permeability. This verified the characterization of the membrane and system parameters was reasonable.

- The permeability to forced air of a series of iCVD-treated membranes was slightly lower than the values predicted by the newly developed asymmetric slip-flow model. Permeability decreased significantly with decreasing pore radius. Asymmetry of the iCVD film did not substantially reduce this decrease.

- The development of asymmetric forms of the diffusion models made it possible to extend the analysis of permeability to pores with higher asymmetry. This analysis showed that

63

using iCVD to increase asymmetry while maintaining constant LEP only decreases the overall permeability of the membrane. When using traditional iCVD methods, permeability is maximized when iCVD film-thickness is minimized. Increasing permeability above this level can only be achieved using methods that allow multiple pore openings for each original pore.

Appendix 2-A: Calculating Knudsen number

The system parameters and Knudsen numbers of the two experimental systems in this study are given in Table 2-A1. Mean free path is calculated according to $\lambda = \frac{k_B T}{\sqrt{2}\pi P d_e^2}$ and the Knudsen number is calculated according $Kn = \frac{\lambda}{2r}$.

Table 2-A1. System parameters and Knudsen numbers of the two experimental systems in this study.

Variable	MD system	Forced air
Boltzmann constant, k_B (J/K)	1.38×10^{-23}	1.38×10^{-23}
Average temperature, T (K)	313	298
Average pressure, P (kPa)	101	101
Collision diameter, d_e (m)	2.64×10^{-10}	3.0×10^{-10}
Mean free path, λ (m)	1.33×10^{-7}	0.9×10^{-7}
Pore radius, r (m)	$1.\times10^{-7}$	$0.99 - 1.92\times10^{-7}$
Knudsen number, Kn	0.38	$0.26 - 0.51$

Appendix 2-B: Derivations of asymmetric transport models

The process for deriving the asymmetric versions of the transport models is the same for water vapor diffusion and forced air permeability. We use the water vapor diffusion equations as the example. To go from K_c (Eq. (2-11)) to K_e (Eq. (2-12)), we need to incorporate the effects of non-constant $r(x)$ and non-constant dP/dx. This results in the equation,

$$K_e = K_c(x)\frac{L}{\Delta P}\left(-\frac{dP}{dx}\right). \qquad \text{(Eq. 2-B1)}$$

Rearranging and taking the integral with respect to x on both sides, this becomes

$$\int_0^L \frac{K_e}{K_c(x)}dx = \int_0^L \frac{L}{\Delta P}\left(-\frac{dP}{dx}\right)dx. \qquad \text{(Eq. 2-B2)}$$

Simplify Eq. (2-B2), results in

$$K_e \int_0^L \frac{1}{K_c(x)}dx = L. \qquad \text{(Eq. 2-B3)}$$

Eq. (2-B3) rearranges to Eq. (2-12).

To go from Eq. (2-12) to Eq. (2-14), we use a change of variables from x to r so that Eq. (2-12) becomes

$$K_a = \frac{L}{\int_{r_t}^{ar_t} \frac{1}{K_c(r)\frac{dr}{dx}}dr}. \qquad \text{(Eq. 2-B4)}$$

Using the linear approximation for $r(x)$ in Eq. (2-13), Eq. (2-B4) can be solved to produce Eq. (2-14). The same process can be applied for the forced air models. When evaluating K_e (Eq. (2-12)) and K_t (Eq. (2-19)) numerically in MATLAB, rectangular numerical integration with a step-size of 0.1 nm was used.

Appendix 2-C: Error introduced by assuming linearly varying pore radius

The error introduced to water vapor permeability by assuming that pore radius varies linearly in x, is given in Fig. 2-C1a. The largest errors are seen for the intermediate value of $S_L = 0.25$ and increase with increasing values of f. The pore profiles corresponding to the three values of S_L confirm that the largest difference between exact and linear pore profiles are for $S_L = 0.25$ (Fig. 2-C1b-d). Errors introduced by the linear pore profile approximation were of similar magnitude for forced air permeability.
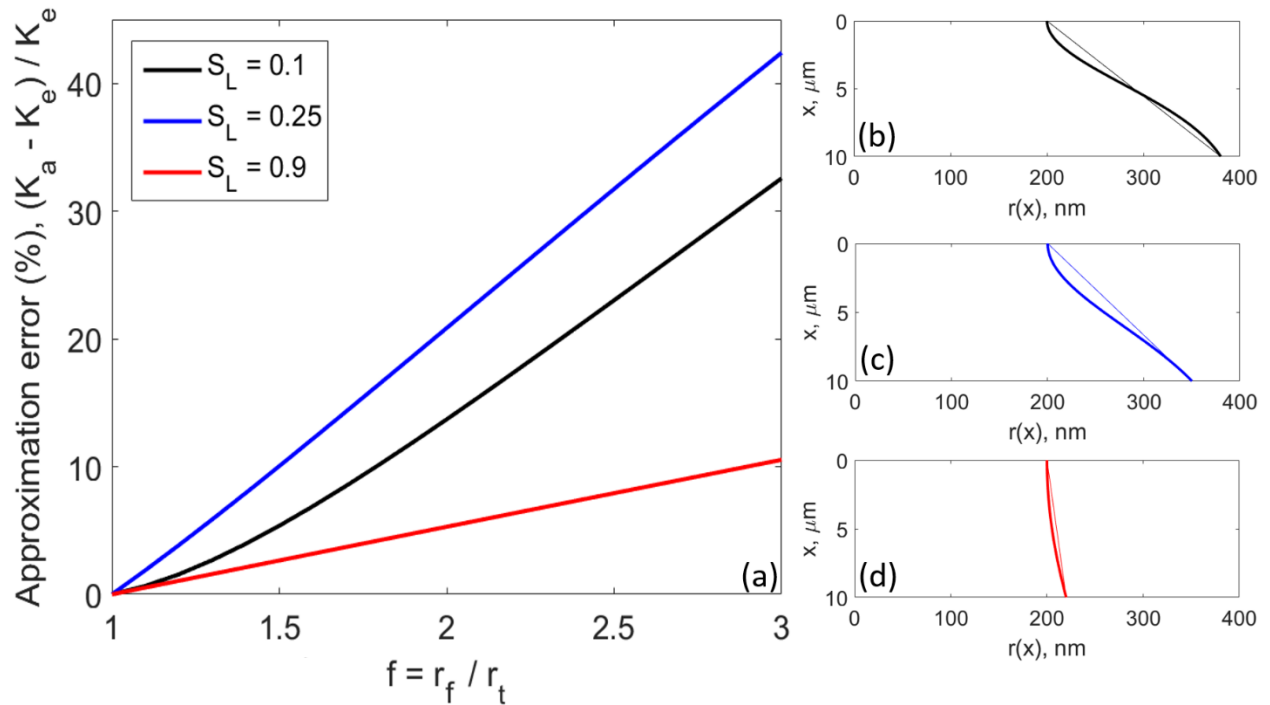
Fig. 2-C1. (a) Percentage difference between dusty gas permeability calculated assuming linearly varying pore radius (Eq. (2-14)) and dusty gas permeability calculated assuming the exact pore profile (Eq. (2-12)). Pore profiles are shown for (b) $S_L = 0.1$, (c) $S_L = 0.25$ and (d) $S_L = 0.9$. In (b)-(d), $f = 2$. The exact pore profile is calculated from Eq. (2-6).

Appendix 2-D: Parameter values for permeability models

Table 2-D1. Parameter values for the permeability models

Parameter	Value
Diffusion coefficient of water in air multiplied by total pressure, PD (Pam^2/s). $PD = 1.895(T^{2.072})10^{-5}$[26]	2.70
Total average pressure, P (kPa)	101
Molecular weight of water, M_w (g/mol)	18
Universal gas constant, R (J/K-mol)	8.314
Average temperature, T (K)	313
Partial pressure of air, P_{air} (kPa)	101
Density of air, ρ (kg/m^3)	1.225
Dynamic viscosity of air, μ (kg/m-s)	1.86×10^{-5}

References

[1] A.M. Alklaibi, N. Lior, Membrane-distillation desalination: Status and potential, Desalination. 171 (2005) 111–131.

[2] K.W. Lawson, D.R. Lloyd, Review: Membrane distillation, J. Membr. Sci. 124 (1997) 1–25.

[3] H. Susanto, Towards practical implementations of membrane distillation, Chem. Eng. Process. Process Intensif. 50 (2011) 139–150.

[4] P. Wang, T.-S. Chung, Recent advances in membrane distillation processes: Membrane development, configuration design and application exploring, J. Membr. Sci. 474 (2015) 39–56.

[5] A. Alkhudhiri, N. Darwish, N. Hilal, Membrane distillation: A comprehensive review, Desalination. 287 (2012) 2–18.

[6] J. Swaminathan, H.W. Chung, D.M. Warsinger, F.A. AlMarzooqi, H.A. Arafat, J.H. Lienhard V, Energy efficiency of permeate gap and novel conductive gap membrane distillation, J. Membr. Sci. 502 (2016) 171–178.

[7] M. Essalhi, M. Khayet, Surface segregation of fluorinated modifying macromolecule for hydrophobic/hydrophilic membrane preparation and application in air gap and direct contact membrane distillation, J. Membr. Sci. 417–418 (2012) 163–173.

[8] M. Khayet, J.I. Mengual, T. Matsuura, Porous hydrophobic/hydrophilic composite membranes, J. Membr. Sci. 252 (2005) 101–113.

[9] M. Qtaishat, M. Khayet, T. Matsuura, Novel porous composite hydrophobic/hydrophilic polysulfone membranes for desalination by direct contact membrane distillation, J. Membr. Sci. 341 (2009) 139–148.

[10] Y. Zhang, R. Wang, S. Yi, L. Setiawan, X. Hu, A.G. Fane, Novel chemical surface modification to enhance hydrophobicity of polyamide-imide (PAI) hollow fiber membranes, J. Membr. Sci. 380 (2011) 241–250.

[11] Y. Liao, R. Wang, A.G. Fane, Engineering superhydrophobic surface on poly(vinylidene fluoride) nanofiber membranes for direct contact membrane distillation, J. Membr. Sci. 440 (2013) 77–87.

[12] F. Guo, A. Servi, A. Liu, K.K. Gleason, G.C. Rutledge, Desalination by Membrane Distillation using Electrospun Polyamide Fiber Membranes with Surface Fluorination by Chemical Vapor Deposition, ACS Appl. Mater. Interfaces. 7 (2015) 8225–8232.

[13] M.I. Ali, E.K. Summers, H.A. Arafat, J.H. Lienhard V, Effects of membrane properties on water production cost in small scale membrane distillation systems, Desalination. 306 (2012) 60–71.

[14] J. Phattaranawik, R. Jiraratananon, A.G. Fane, Effect of pore size distribution and air flux on mass transport in direct contact membrane distillation, J. Membr. Sci. 215 (2003) 75–85.

[15] M.S. El-Bourawi, Z. Ding, R. Ma, M. Khayet, A framework for better understanding membrane distillation separation process, J. Membr. Sci. 285 (2006) 4–29.

[16] E.K. Summers, H.A. Arafat, J.H. Lienhard V, Energy efficiency comparison of single-stage membrane distillation (MD) desalination cycles in different configurations, Desalination. 290 (2012) 54–66.

[17] A.C.M. Franken, J.A.M. Nolten, M.H.V. Mulder, D. Bargeman, C.A. Smolders, Wetting criteria for the applicability of membrane distillation, J. Membr. Sci. 33 (1987) 315–328.

[18] A.M. Coclite, R.M. Howden, D.C. Borrelli, C.D. Petruczok, R. Yang, J.L. Yagüe, A. Ugur, N. Chen, S. Lee, W.J. Jo, A. Liu, X. Wang, K.K. Gleason, 25th Anniversary Article: CVD

Polymers: A New Paradigm for Surface Modification and Device Fabrication, Adv. Mater. 25 (2013) 5392–5423.

[19] D.M. Warsinger, A. Servi, S. Van Belleghem, J. Gonzalez, J. Swaminathan, J. Kharraz, H.W. Chung, H.A. Arafat, K.K. Gleason, J.H. Lienhard V, Combining air recharging and membrane superhydrophobicity for fouling prevention in membrane distillation, J. Membr. Sci. 505 (2016) 241–252.

[20] M. Ma, Y. Mao, M. Gupta, K.K. Gleason, G.C. Rutledge, Superhydrophobic Fabrics Produced by Electrospinning and Chemical Vapor Deposition, Macromolecules. 38 (2005) 9742–9748.

[21] M. Ma, M. Gupta, Z. Li, L. Zhai, K.K. Gleason, R.E. Cohen, M.F. Rubner, G.C. Rutledge, Decorated Electrospun Fibers Exhibiting Superhydrophobicity, Adv. Mater. 19 (2007) 255–259.

[22] M. Gupta, V. Kapur, N.M. Pinkerton, K.K. Gleason, Initiated Chemical Vapor Deposition (iCVD) of Conformal Polymeric Nanocoatings for the Surface Modification of High-Aspect-Ratio Pores, Chem. Mater. 20 (2008) 1646–1651.

[23] S.H. Baxamusa, K.K. Gleason, Thin Polymer Films with High Step Coverage in Microtrenches by Initiated CVD, Chem. Vap. Depos. 14 (2008) 313–318.

[24] A. Asatekin, K.K. Gleason, Polymeric nanopore membranes for hydrophobicity-based separations by conformal initiated chemical vapor deposition, Nanoletters. 11 (2011) 677–686.

[25] J.B. Young, B. Todd, Modelling of multi-component gas flows in capillaries and porous solids, Int. J. Heat Mass Transf. 48 (2005) 5338–5353.

[26] M. Khayet, A. Velázquez, J.I. Mengual, Modelling mass transport through a porous partition: Effect of pore size distribution, J. Non-Equilib. Thermodyn. 29 (2004). http://www.degruyter.com/view/j/jnet.2004.29.issue-3/jnetdy.2004.055/jnetdy.2004.055.xml (accessed February 22, 2016).

[27] E.H. Kennard, Kinetic theory of gases, McGraw Hill Book Company, inc, New York and London, 1938.

[28] S. Fukui, R. Kaneko, A database for interpolation of Poiseuille flow rates for high Knudsen number lubrication problems, J. Tribol. 112 (1990) 78–83.

[29] S. Fukui, R. Kaneko, Analysis of ultra-thin gas film lubrication based on linearized Boltzmann equation: first report—derivation of a generalized lubrication equation including thermal creep flow, J. Tribol. 110 (1988) 253–261.

[30] Y. Mitsuya, Modified Reynolds equation for ultra-thin film gas lubrication using 1.5-order slip-flow model and considering surface accommodation coefficient, J. Tribol. 115 (1993) 289–294.

[31] A. Burgdorfer, The influence of the molecular mean free path on the performance of hydrodynamic gas lubricated bearings. Interim Report., Franklin Inst. Labs. for Research and Development, Philadelphia, 1958. http://www.osti.gov/scitech/biblio/4329043 (accessed February 21, 2016).

[32] A. Liu, E. Goktekin, K.K. Gleason, Cross-linking and ultrathin grafted gradation of fluorinated polymers synthesized via initiated chemical vapor deposition to prevent surface reconstruction, Langmuir. 30 (2014) 14189–14194.

[33] K. Honda, M. Morita, H. Otsuka, A. Takahara, Molecular aggregation structure and surface properties of poly(fluoroalkyl acrylate) thin films, Macromolecules. 38 (2005) 5699–5705.

[34] R.C. Buck, J. Franklin, U. Berger, J.M. Conder, I.T. Cousins, P. de Voogt, A.A. Jensen, K. Kannan, S.A. Mabury, S.P. van Leeuwen, Perfluoroalkyl and polyfluoroalkyl substances in the environment: Terminology, classification, and origins, Integr. Environ. Assess. Manag. 7 (2011) 513–541.

[35] J. Baek, M.J. Kwak, M.S. Oh, Y. Yoo, J.B. You, S.G. Im, A Conformal Vapor-Phase Deposition of Poly(2-(perfluorohexyl)ethyl methacrylate) and the Hydrophobic Properties There, Nanosci. Nanotechnol. Lett. 7 (2015) 45–49.

[36] C.D. Petruczok, N. Chen, K.K. Gleason, Closed Batch Initiated Chemical Vapor Deposition of Ultrathin, Functional, and Conformal Polymer Films, Langmuir. 30 (2014) 4830–4837.

[37] J.I. Calvo, A. Hernández, G. Caruana, L. Martınez, Pore size distributions in microporous membranes. I. Surface Study of Track-etched filters by image analysis, Jouranl Colloid Interface Sci. 175 (1995) 138–250.

[38] M.C. García-Payo, M.A. Izquierdo, C. Fernandez-Pineda, Wetting study of hydrophobic membranes via liquid entry pressure measurements with aqueous alcohol solutions, J. Colloid Interface Sci. 230 (2000) 420–431.

[39] K. He, H.J. Hwang, I.S. Moon, Air gap membrane distillation on the different types of membrane, Korean J. Chem. Eng. 28 (2011) 770–777.

[40] D.E.M. Warsinger, J. Swaminathan, L.A. Maswadeh, J.H. Lienhard V, Superhydrophobic condenser surfaces for air gap membrane distillation, J. Membr. Sci. 492 (2015) 578–587.

[41] K.G. Nayar, D. Panchanathan, G.H. McKinley, J.H. Lienhard V, Surface Tension of Seawater, J. Phys. Chem. Ref. Data. 43 (2014) 43103. doi:10.1063/1.4899037.

[42] E. Guillen-Burrieza, A. Servi, B.S. Lalia, H.A. Arafat, Membrane structure and surface morphology impact on the wetting of MD membranes, J. Membr. Sci. 483 (2015) 94–103.

[43] R.J. Frank-Finney, P.D. Haller, M. Gupta, Ultrathin Free-Standing Polymer Films Deposited onto Patterned Ionic Liquids and Silicone Oil, Macromolecules. 45 (2012) 165–170.

CHAPTER THREE

A systematic study of the impact of hydrophobicity on the wetting of MD membranes

Abstract

Membrane distillation (MD) is a thermal separation process used for desalination. In MD, a hydrophobic membrane acts as a barrier between feed and distillate solutions. MD membranes are often fabricated using surface modification to increase hydrophobicity and prevent wetting. However, environmental safety concerns about the hydrophobic surface-modification materials persist. In this study we quantify the relationship between hydrophobicity and membrane wetting for a surface-modified nylon membrane. This relationship determines the conditions when lower-hydrophobicity, environmentally-friendly surface-modification chemistries, can be used. For the membranes in this study, we found that for all intrinsic advancing contact angles (ACA) ≥ 90 °, water liquid entry pressure (LEP_w) was in a range suitable for MD. We explained this result with a new model for liquid entry pressure (LEP). This work predicted that hydrocarbon film, poly(divinyl benzene) (pDVB), an environmentally-friendly but low-hydrophobicity polymer, could be a successful surface-modifier for MD. We thus fabricated a nylon-pDVB composite membrane and demonstrated it in an MD desalination system. Jehad Kharraz, David Klee, Katie Notarangelo, Brook Eyob, Dr. Elena Guillen-Burrieza, Andong Liu, Professor Hassan A. Arafat and Professor Karen K. Gleason contributed to this work.

3.1. Introduction

Membrane distillation (MD) is a thermal separation process used for desalination [1–5]. In MD, a hydrophobic membrane acts as a barrier between a heated feed stream and a cooled distillate stream (Fig. 3-12a inset). The temperature difference between feed and distillate creates a partial pressure gradient, driving water vapor through the membrane. At the same time, a combination of hydrophobicity and pore architecture prevents the liquid streams from entering the membrane [6]. This prevents cross-contamination and loss of system efficiency [7]. Currently, there are no commercial membranes optimized for membrane distillation. Instead, membranes developed for micro- and ultra-filtration are used [5]. There is ongoing need for specialized membranes to improve MD system performance [3].

Researchers have developed many novel, high-flux membranes for MD [8–13]. These membranes often consist of a phase-inversion or electrospun base, modified to increase the hydrophobicity of the surface. Surface-modification can be incorporated during membrane formation or applied after as a coating. Surface modification is a versatile strategy for developing high-performance hydrophobic membranes. It allows bulk membrane characteristics (pore size, pore size distribution, mechanical properties, etc.) to be combined with surface properties in ways that are not achievable using a single material. These new combinations of properties open up a broader range of possibilities for optimizing the performance of hydrophobic membranes for MD.

Surface-modified membranes have proven successful for MD. However, environmental safety concerns about the surface-modifying chemistries persist. Poly(1H, 1H, 2H, 2H-perfluorodecyl acrylate) (pPFDA) is an exceptionally hydrophobic surface-modification chemistry [14], and

initiated chemical vapor deposition (iCVD) of pPFDA produces super-hydrophobic membranes [13,15,16]. However, decomposition of pPFDA is a pathway to perfluorooctanoic acid (PFOA). PFOA has been found to be toxic and persistent in the environment, causing pPFDA to be banned from future commercial use [17]. iCVD researchers are thus seeking alternative hydrophobic surface-modification chemistries. However, these option are often less hydrophobic than pPFDA. To determine which of these chemistries could still be suitable for MD, it is necessary to know the effects of hydrophobicity on membrane wetting.

This study has two parts. First, we experimentally quantified the relationship between membrane hydrophobicity and water liquid entry pressure (LEP$_w$). We analyzed the results by developing a new model for liquid entry pressure. Second, we used the results to prepare an environmentally-friendly membrane for MD. A commercial, 200 nm pore size (diameter), phase-inversion nylon membrane was used as the base membrane for both parts of this study (Fig. 3-1). The membrane's pores are the spaces between fiber-like pieces of membrane material. The placement of the fibers appears random and each pore has a different size and shape. However, the membrane is quite thick (100 µm) in comparison to the pore size, and there are many layers of pores. This prevents abnormally large passages through the membrane from occurring. A previous study involving the same batch of as-purchased membranes found an average pore radius of 139 nm and a maximum pore radius of 460 nm using capillary flow porosimetry [6].

The commercial nylon membranes are low-cost, environmentally-friendly, and widely available. They are also robust due to the strength of the nylon and the polyester support threads that run through the membrane (Fig. 3-1d). However, despite these advantages, nylon phase-inversion

membranes are hydrophilic and thus cannot be used for MD as-purchased. In order to be useful for MD applications, hydrophobic surface-modification is required. All surface-modification in this work was achieved using iCVD [18]. iCVD grows a conformal, ultra-thin polymer film on the membrane surface and within the pores (Fig. 3-4). This alters the membrane's surface properties without significantly changing the underlying pore structure [19–21].
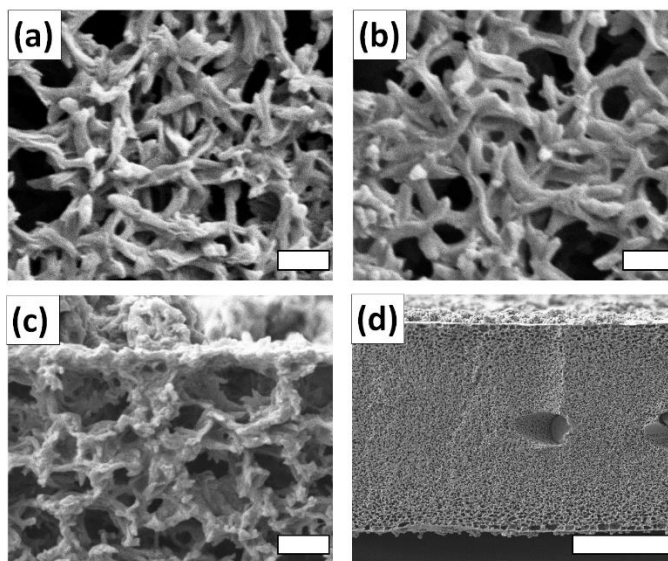
Fig. 3-1. Top views of (a) a nylon membrane as received (b) a nylon membrane coated with a conformal, ultra-thin (~10 nm) layer of pDVB using iCVD. (c) and (d) are cross-section views of a nylon-pDVB membrane. The large features in the middle of (d) are the polyester support threads. Scale bars for (a) and (b) are 1 µm. The scale bar for (c) is 2 µm and the scale bar for (d) is 50 µm.

Two surface-modifying chemistries, pPFDA and poly(divinyl benzene) (pDVB), were used in this study. pDVB is less hydrophobic than pPFDA. It is also environmentally-friendly, inexpensive, robust and well-characterized as an iCVD chemistry [22–24]. In the first part of this study, we prepared a nylon-pPFDA membrane and a nylon-pDVB membrane. We tested these membranes

75

for liquid entry pressure[4] (LEP) using a series of ethanol/water test-solutions (Fig. 3-2a). This series of solutions permitted systematic variation in the difference in surface energy between the solution and the membrane. Processing this data revealed the relationship between hydrophobicity and LEP_w over a large range of contact angles. Similar methods have been used previously to study LEP, but not in the context of membrane design [25,26]. This work determined that a nylon-pDVB membrane should have high enough LEP_w for MD. In the second part of this study, we verified this prediction, testing a nylon-pDVB membrane in an MD system (Fig. 3-2b).

---

[4] Liquid entry pressure (LEP) is the applied pressure at which a liquid in contact with a membrane wets the membrane. Water liquid entry pressure (LEP_w) is the LEP when the liquid is water.
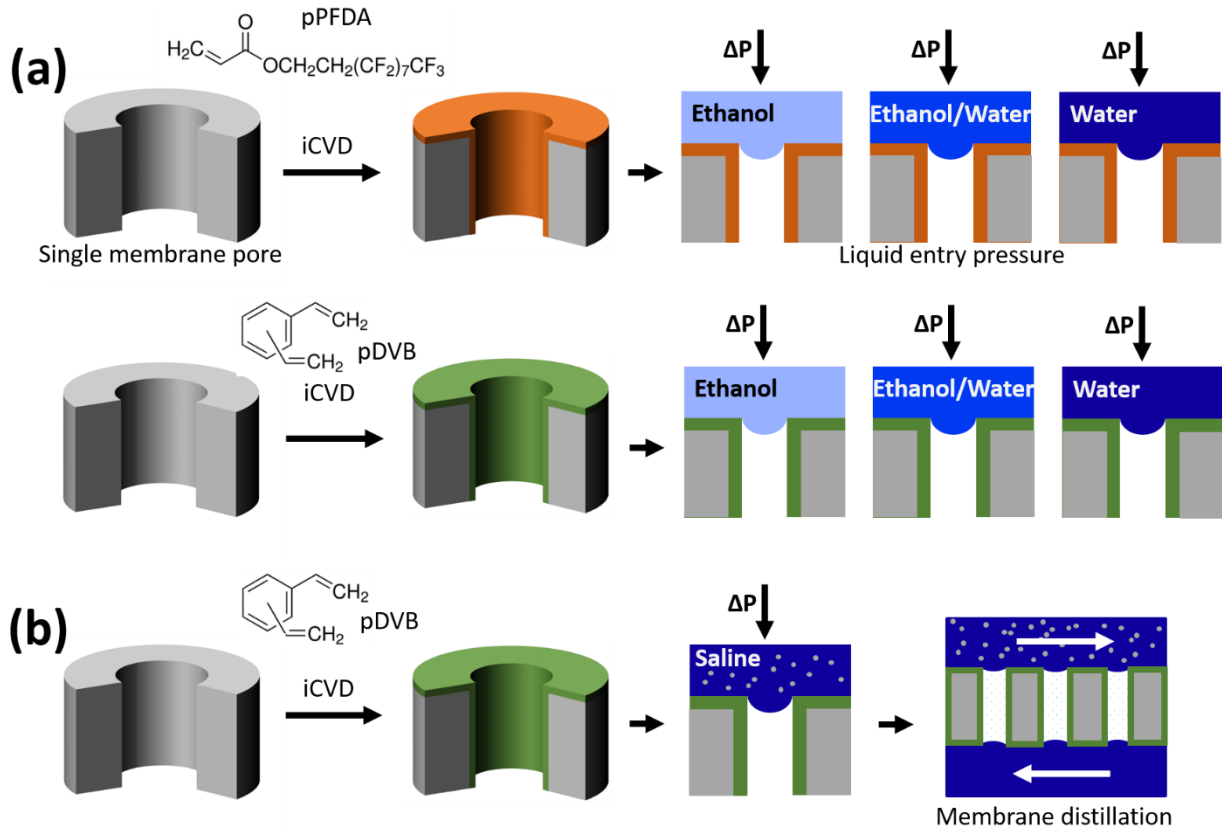
Fig. 3-2. (a) Nylon-pPFDA and nylon-pDVB membranes were tested for LEP using multiple ethanol/water solutions. (b) A second nylon-pDVB membrane tested in a lab-scale MD desalination system.

3.2. Theoretical background

Mathematical models of LEP help guide the interpretation of the experimental results in this study. The general equation for the liquid entry pressure of a single pore is

$$\Delta P = \left(\frac{-B\gamma}{r}\right) cos\theta_{eff} \hspace{2cm} \text{(Eq. 3-1)}$$

where ΔP is liquid entry pressure, γ is the surface tension of the liquid, r is pore radius, and B is a shape factor. $B = 2$ for pores with a circular cross-section and lower values for non-circular pores.

θ_{eff} is the effective contact angle ($0\,° < \theta_{eff} < 180\,°$). θ_{eff} is a function of intrinsic advancing contact

angle (ACA)[5] and pore morphology.

In modeling LEP, pores (Fig. 3-3c) are generally approximated as either cylindrical (Fig. 3-3a,

Fig. 3-3b) or toroidal (Fig. 3-3d, Fig. 3-3e). If the pores are cylindrical, θ_{eff} is the intrinsic ACA

and $B = 2$. Eq. (3-1) thus becomes

$$\varDelta P = \left(\frac{-2\gamma}{r}\right)cos\theta \qquad\qquad\text{(Eq. 3-2)}$$

where θ is the intrinsic ACA. This is the Young-Laplace model for LEP.

---

[5] The intrinsic advancing contact angle is the advancing contact angle between a liquid and an ideal solid surface. An ideal solid surface is defined as a smooth, rigid, chemically homogeneous, insoluble and non-reactive surface. We approximate the advancing intrinsic contact angle between our test solutions and the iCVD polymer films by measuring the advancing contact angles of the solutions on silicon wafers treated with the polymer films. All contact angles referred to in this study are intrinsic advancing contact angles.
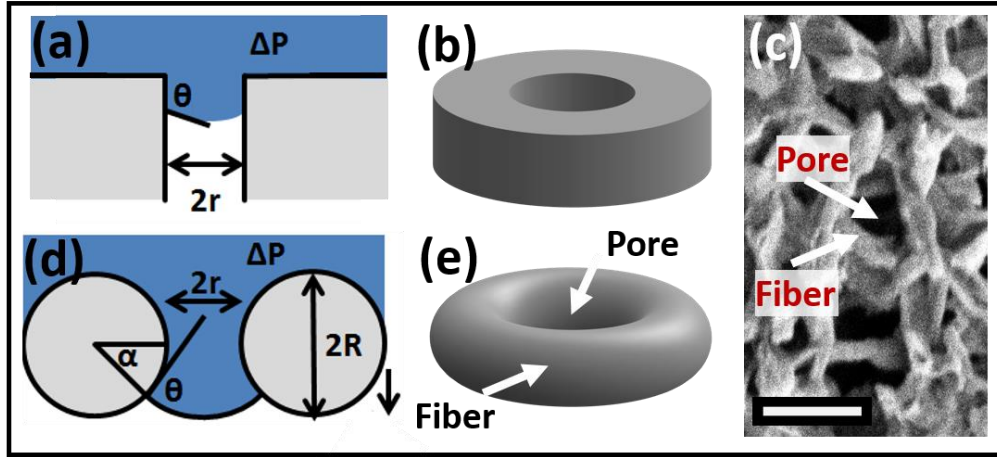
Fig. 3-3. (a), (b) Cylindrical pore (Young-Laplace model). (d), (e) Toroidal pore (Purcell model). (c) SEM image of the nylon membrane used in this study (scale bar is 1 μm).

If the pores are toroidal, LEP follows Eq. (3-1), but with alternative values for θ_{eff} and B (Eq. (3-3), Eq. (3-4)). This produces the Purcell Model [27]. For a toroidal pore, as the pressure across the pore increases, the value of α increases to accommodate it (Fig. 3-3d). At a critical pressure, further increase in α no longer supports additional pressure, and the liquid breaks through the pore. The pressure at which this occurs is the liquid entry pressure.

The equation for liquid entry pressure for the Purcell model is

$$\Delta P = \left(\frac{-2\gamma}{r}\right)\frac{\cos(\theta+\alpha)}{1+R/r(1-\cos(\alpha))} \tag{Eq. 3-3}$$

where R is the fiber radius and α is the angle below horizontal at which the liquid meniscus pins prior to break-through. The value of α is calculated according to

$$sin(\theta + \alpha) = \frac{sin\theta}{1+r/R} \tag{Eq. 3-4}$$

Further explanation of these models can be found in Appendix 3-A.

3.3. Materials and methods

3.3.1 Membranes

The base membranes were commercial phase-inversion nylon membranes (Sterlitech, NY0214225) reinforced with polyester support threads. Nominal pore size (diameter) of the membranes was 200 nm and total membrane thickness was 100 µm (Fig. 3-1).

3.3.2 iCVD polymer thin films

iCVD polymer thin films were deposited in a custom-built reaction chamber (Fig. 3-4). The chamber was cylindrical (height = 38 mm, diameter = 246 mm). It contained an array of 14 resistively heated parallel filaments (80% Ni, 20% Cr). Membranes were taped to a cooled stage (recirculating chiller/heater, NESLAB). The total pressure inside the chamber was maintained at a constant value using a mechanical pump (45 CFM pumping speed, Alcatel). To produce the films, tert-butyl peroxide (TBPO, Sigma-Aldrich, 97%) initiator and PFDA (Sigma-Aldrich, 97%) or DVB (Sigma-Aldrich, 80%) monomer were flowed into the chamber. Film thickness was monitored *in situ* using a laser interferometer. Three separate membranes were prepared for this study. Two of the membranes were for LEP testing. One had ~10 nm of pDVB deposited on one surface, and one had ~10 nm of pPFDA deposited on one surface. A third membrane was prepared for DCMD testing. This membrane had ~5 nm of pDVB deposited on both surfaces. This ensured that both surfaces had equal resistance to liquid water entry, but the total film thickness was the same as for the other two membranes. Table 3-1 includes the deposition parameters for the three membranes.
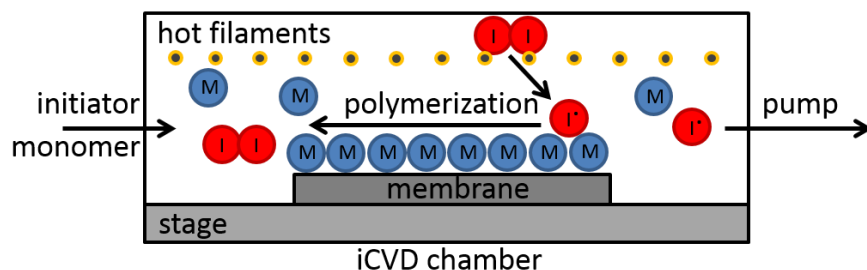
Fig. 3-4. iCVD chamber containing a membrane. Initiator and monomer flow into the chamber where the hot filaments break the initiator into free radicals. Polymerization occurs on the membrane surface and within the pores.

Table 3-1. Experimentally optimized deposition parameters for the pPFDA and pDVB thin-films in this study. The pDVB film on the membrane tested in the DCMD system was deposited in two stages: ~5 nm (35 minutes) on one side and ~5 nm (35 minutes) on the other side.

Membrane	pPFDA for LEP	pDVB for LEP	pDVB for DCMD
TBPO flow rate (sccm[6])	1.0	1.0	1.0
Monomer flow rate (sccm)	0.2	0.5	0.5
Monomer temperature (°C)	60	60	60
Stage temperature (°C)	40	30	30
Total chamber pressure (mTorr[7])	100	800	800
Filament temperature (°C)	290	220	220
Deposition time (min:sec)	1:50	70:00	35:00 +35:00
Total film thickness (nm)	~10	~10	~5 + ~5

---

[6] sccm = standard cubic centimeters per minute (cm^3/min at standard temperature and pressure).
[7] 1 Torr = 133.322 Pa.

3.3.3 Membrane characterization

3.3.3.1 Scanning electron microscope

Membranes were imaged using a scanning electron microscope (SEM, JEOL 6010a) at 5 kV accelerating voltage. Samples were sputtered with 9 nm of gold prior to imaging. To prepare the cross-sections, membranes were frozen in ice before being fractured. This method preserves the pore structure [28].

3.3.3.2 Fourier transform infrared spectroscopy

The iCVD films were characterized using Fourier transfer infrared (FTIR) spectroscopy (Thermo Nicolet Nexus 870 spectrometer) using absorption mode with attenuated total reflection (ATR) and a Germanium hemispherical crystal (Harrick). A deuterated triglycine sulfate KBr beamsplitter and a liquid nitrogen cooled mercury cadmium telluride (MCT-B) detector were used. Baseline-corrected spectra were collected over $650–3400$ cm^{-1} at 2 cm^{-1} resolution and averaged over 256 scans. Spectra were processed using the OMNIC software package (Thermo Scientific).

3.3.3.3. Intrinsic advancing contact angle

Intrinsic advancing contact angles (ACA) were measured on silicon wafers coated alongside the membranes. Measurements were taken using a goniometer equipped with an automatic dispenser (model 590, Ramé-Hart). DropImage software was used to acquire images for measurement. A 2 µL drop of room-temperature DI water was first placed onto the membrane surface. Water was added to this drop in increments of 2 µL. The angle between the advancing drop and the surface was measured 100 ms after each addition. Every reported data point is the average of measurements from 3 – 5 locations on the wafer.

3.3.3.4. Liquid entry pressure

Liquid entry pressure (LEP) was measured with a custom system similar to ones used previously [13,26,29] (Fig. 3-5, Fig. 3-11). Three types of test-solutions were used: ethanol/water solutions, saline (35 g/L, NaCL) and dyed-water. For all LEP tests, a pristine sample of the surface-modified membrane was held in a 13 mm syringe membrane holder (GE healthcare biosciences). The membrane was exposed to the test-solution on one surface and deionized (DI) water on the other. A syringe pump (PHD 22/2000, Harvard apparatus) incrementally increased the pressure of the test-solution against the membrane. After each increase, the pressure was held constant for at least 10 seconds. A USB pressure transducer (PX409, Omega) monitored the pressure difference across the membrane. For the ethanol/water solutions, LEP was detected by a pressure-drop during a hold. For the saline tests, the deionized water reservoir was monitored using an electrical conductivity meter (Oakton Con6 Probe). LEP was detected by an increase in the electrical conductivity of the reservoir. For the dyed-water, LEP was detected when dye was visible in the DI water reservoir.
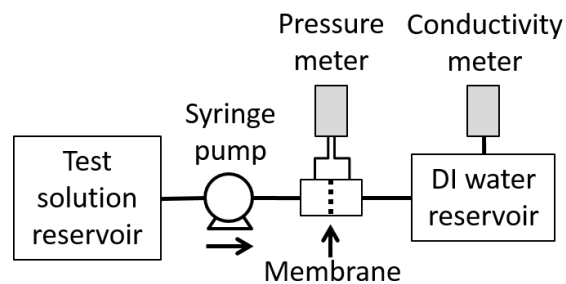
Fig. 3-5. LEP is measured by incrementally increasing the pressure of the test-solution (ethanol/water, saline solution or dyed-water) against the membrane until LEP is reached.

3.3.3.5. Direct contact membrane distillation

Direct contact membrane distillation (DCMD) was conducted using a custom-built lab-scale system. The membrane was held in a cross-flow cell (Sterlitech Corp., USA, Model CF042). Plastic mesh-type spacers were used on both sides of the membrane to promote turbulence and to support the membrane. The active area of the membrane was rectangular with a surface area of 30 cm^2. Feed and distillate tanks were equipped with heating/cooling jackets. Sensors monitored pressure, temperature, flow rates and distillate conductivity. The feed solution contained DI water and table salt at a concentration of 35 g/L. Conductivity of the feed was 40-44 mS/cm. The liquid on the distillate side of the membrane was DI water with a conductivity of 100 µS/cm. Feed and distillate flowed past the membrane at a rate of 25 L/hr using a variable drive pump. Distillate overflow was monitored using a microbalance. All operational parameters were recorded every 10 seconds using a custom data acquisition system (Convergence, Netherlands). These values were used to calculate distillate flux and salt rejection.

We conducted two DCMD tests on a Nylon-pDVB composite membrane. First, the effect of partial pressure on specific distillate flux was determined by raising the feed temperature from 40 to 70 °C in increments of 10 °C while the distillate was held at 25 °C. Second, the stability of distillate flux and salt-rejection over time was tested directly following. For this test, distillate flux and salt-rejection were monitored over the course of 18 hours while the feed was held at 50 °C and the distillate was held at 25 °C.

3.4. Results and discussion

3.4.1 Relationship between hydrophobicity and LEP

In the first part of this study, we quantified the relationship between hydrophobicity and water liquid entry pressure (LEP_w). To quantify this relationship, a nylon-pPFDA and a nylon-pDVB membrane were tested for liquid entry pressure (LEP) using ethanol/water solutions (Table 3-2, Table 3-3). The nylon-pPFDA membrane was tested with solutions over the entire compositional range from 0 - 100 vol% ethanol. Because of its lower hydrophobicity, the nylon-pDVB membrane was tested with solutions ranging in composition from 0 - 50 vol% ethanol. Solutions with higher ethanol content produced negative LEP values for the nylon-pDVB membrane.

Table 3-2. Intrinsic advancing contact angle (ACA), surface tension of the solution and LEP for the nylon-pPFDA membrane tested using a series of ethanol/water solutions. Intrinsic ACA was measured on a silicon wafer treated with a pPFDA coating. LEP_w was calculated by normalizing LEP by the surface tension of water (Eq.(3-5)).

Ethanol volume percentage (%)	Ethanol mol fraction (%)	Intrinsic ACA (measured) (°)	Surface tension (calculated) (N/m)	LEP (measured) (kPa)	Water LEP (LEP_w) (calculated) (kPa)
100	100	88	0.023	58	182
75	48	94	0.025	87	249
65	36	101	0.026	101	275
50	24	102	0.029	120	296
35	14	111	0.033	147	317
25	9	118	0.038	185	353
10	3	122	0.051	276	393
0	0	129	0.072	377	377

Table 3-3. Intrinsic advancing contact angle (ACA), surface tension and LEP for a nylon-pDVB membrane tested using a series of ethanol/water solutions. Intrinsic ACA was measured on a silicon wafer treated with a pDVB coating. LEP_w was calculated by normalizing LEP by the surface tension of water (Eq. (3-5)).

Ethanol volume percentage (%)	Ethanol mol fraction (%)	Intrinsic ACA (measured) (°)	Surface tension (calculated) (N/m)	LEP as measured (kPa)	Water LEP (LEP_w) (calculated) (kPa)
50	24	63	0.029	0	0
30	12	79	0.035	63	128
16.7	6	84	0.043	114	190
10	3	98	0.051	165	234
0	0	104	0.072	288	288

LEP is a function of both contact angle and surface tension (Eq. (3-1)). To determine LEP_w from this data, we normalize LEP by the surface tension of water. This obtains

$$LEP_w = \frac{LEP \times \gamma_w}{\gamma} \tag{Eq. 3-5}$$

where $\gamma_w = 0.072$ N/m is the surface tension of water and γ is the surface tension of the test-solution. The surface tensions of the test-solutions were calculated according to

$$\gamma = \frac{3.35 + 20.6x}{0.0465 + x} \times 10^{-3} \tag{Eq. 3-6}$$

where x is the mole fraction of ethanol and γ is surface tension in units of N/m^{2}.

Fig. 3-6 shows the data for LEP_w plotted against intrinsic ACA. LEP_w appears almost linear over the region studied, ranging from 0 kPa at 63 ° to 377 kPa at 129 °. For intrinsic ACA greater than 90 °, LEP_w is always greater than 200 kPa. These results have implications for MD membrane design. For instance, reducing hydrophobicity from ~ 130 ° to 90 ° reduces LEP_w by approximately 50%. This is a large decrease, but because LEP_w remains positive at the lower intrinsic ACA value, membranes with this lower degree of hydrophobicity remain potential candidates for MD. On the other hand, membranes with intrinsic ACA ~ 60 °, such as untreated nylon, are likely to have negative LEP_w. This would cause them to wet spontaneously upon contact with water making them non-viable for MD.
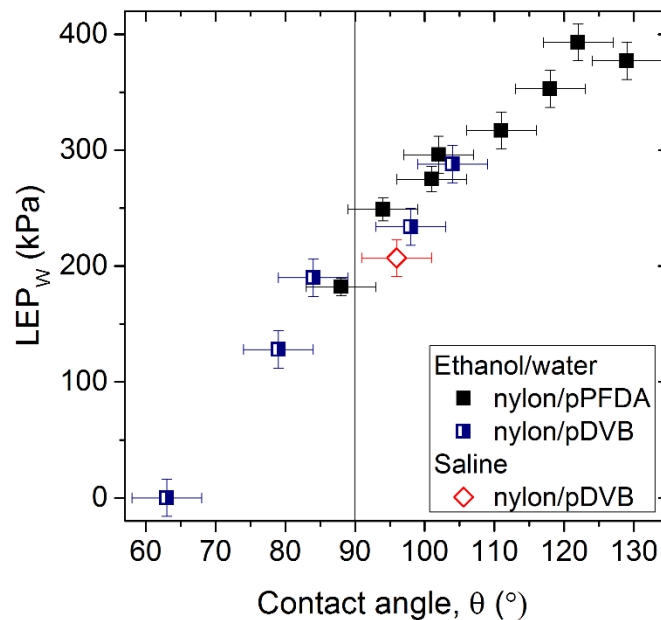
Fig. 3-6. LEP_w with respect to intrinsic advancing contact angle (ACA). LEP_w values were calculated from data gathered using ethanol/water test-solutions. LEP_w for saline of the nylon-pDVB membrane from the second part of this study is also included.

We further analyzed these results using existing theory of LEP. Fig. 3-7 shows the data from Fig. 3-6 alongside the Young-Laplace and Purcell models. Parameter values for each model were calculated for best fit with the data (Table 3-4). In Fig. 3-7, the models are plotted assuming the test solution is water.
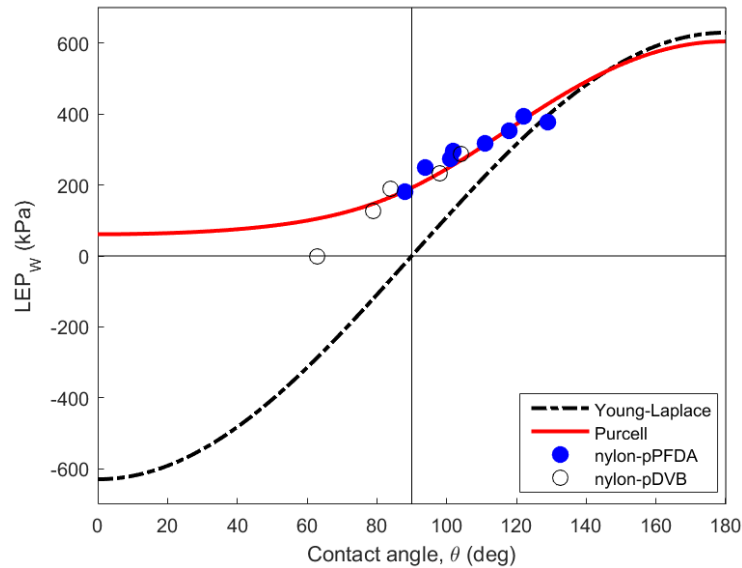
Fig. 3-7. LEP_w data fitted with the Young-Laplace and Purcell models. The fitted parameter values are shown in Table 3-4.

It is clear from Fig. 3-7 that the Young-Laplace model, developed for pores with cylindrical geometries (Fig. 3-3a, Fig. 3-3b), is not an appropriate model for the data. This is important because Young-Laplace is commonly used to interpret the LEP behavior of membranes [1,2,5]. Fig. 3-7 reveals that the Young-Laplace model under-predicts the experimentally measured LEP values. This discrepancy increases for lower values of intrinsic ACA. This suggests that the Young-Laplace has limited utility for any membrane that is not super-hydrophobic. This is regardless of other factors such as pore size and pore morphology. For example, at contact angles approaching 90 °, Young-Laplace predicts LEP approaching 0 kPa. This would be insufficient to

89

support MD. However, the measured LEP value at 90 ° was approximately 200 kPa, a value which might indeed allow for MD operations. The Young-Laplace model also overemphasizes the benefits of maximizing hydrophobicity to improve membrane performance. The Purcell model for LEP, based on toroidal pore shapes (Fig. 3-3d, Fig. 3-3e), is in better agreement with the experimental data. It predicts LEP accurately for $\theta \geq 90$ °. However, a major shortcoming of this model is that it predicts positive LEP values as low as 0 ° intrinsic ACA regardless of the membrane's morphology. This conflicts with the measured value of LEP = 0 kPa at $\theta = 63$ ° in Fig. 3-7. While this is the only data-point in Fig. 3-7 that clearly deviates from the Purcell model, it illustrates a larger issue with the model. If LEP > 0 kPa for all θ, then even a super-hydrophilic membrane would not wet. This goes against our experience that many hydrophilic membranes wet spontaneously.

To address this limitation for predicting LEP from existing models, we developed a new model for LEP that builds upon the Purcell model. The Purcell model describes an isolated toroidal pore. Our extension of this model considers possible interactions with membrane structures below the surface of the pore that is initially wetted. We observed that in the Purcell model, liquid entry depends on two steps occurring: First, the liquid must move into the space between the fibers (enter the pore). Second, it must release from the fibers (exit the pore). For a hydrophilic membrane, liquid spontaneously enters the pore, but a positive pressure is needed to release it from the fibers. This causes the Purcell model to predict positive LEP values even for super-hydrophilic membranes. We hypothesized that for a real membrane, with pores not only at the surface but within the bulk of the membrane as well, the second step is not always needed for liquid breakthrough. In a hydrophilic membrane, the liquid enters the pores spontaneously. Depending

on the pore architecture, it may then immediately contact fibers from nearby pores. These fibers attract the liquid, pulling it further into the membrane under no applied pressure. This results in a negative LEP due to interactions between the pores that are not captured in the Purcell model.

Whether or not the surface pores can be considered to act in isolation or not depends on the placements of the other pores/fibers. We account for this by incorporating a "floor" below each pore into a new model for LEP (Fig. 3-8). A similar idea has been proposed previously [30]. While Fig. 3-8 shows the floor as a flat plate, it represents fibers of any shape located at some distance from the pore. LEP is now defined as the pressure at which the liquid detaches from the pore or intercepts the floor, whichever occurs at the lower pressure. The introduction of the floor introduces a new variable, h, the distance between the floor and the bottom of the pore's fibers. This value is positive if there is a gap between the fibers and floor and negative if the floor is above the bottom of the fibers. To calculate LEP using this new model, Eq. (3-3) is used along with Eq. (3-4) and an additional equation:

$$\frac{r+R(1-cos(\alpha))}{-\cos(\theta+\alpha)}\left(1 - sin(\alpha + \theta)\right) = R\left(1 - sin(\alpha)\right) + h. \tag{Eq. 3-7}$$

The derivation for this new equation is in Appendix 3-A.
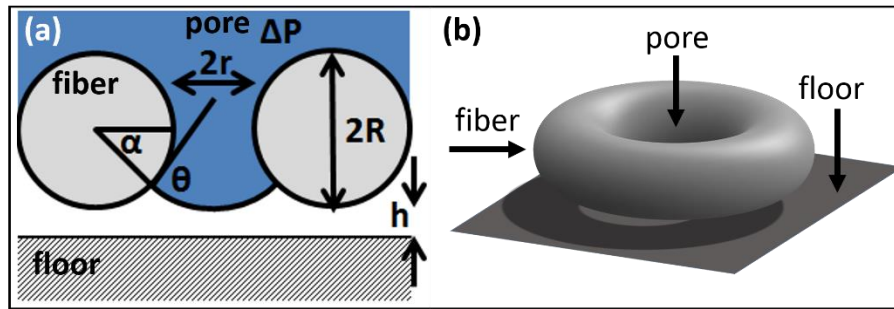
Fig. 3-8. The pore configuration for the modified Purcell model from (a) the side and (b) in three dimensions. h, is the distance between the bottom of the fibers and the floor. h can be positive or negative.

A non-linear least squares regression of our modified Purcell model to the LEP_w data was used to calculate the parameters providing the best fit (Fig. 3-9, Table 3-4). This model correctly predicts negative LEP_w values below a certain contact angle. By accounting for the importance of membrane structures below the initially contacted surface, our modified Purcell model improves upon the predictions of either the Purcell and Young-Laplace for isolated pores, progressing the understanding of LEP of membranes.
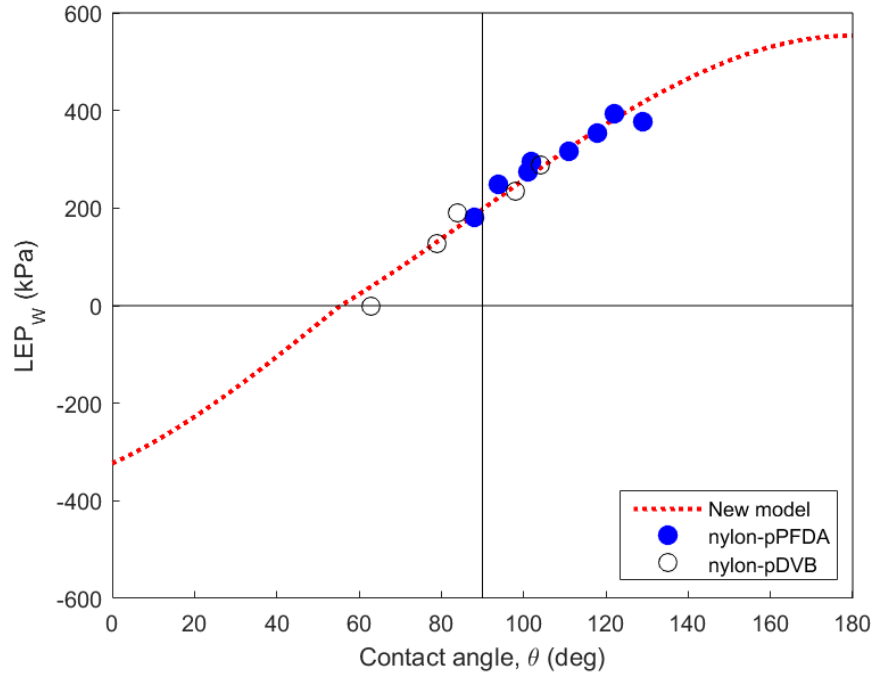
Fig. 3-9. LEP$_w$ for the nylon-pPFDA and nylon-pDVB membranes plotted along with the new modified Purcell model.

The best fit parameter values for the curves shown in Fig. 3-7 and Fig. 3-9 are given in Table 3-4. All values in Table 3-4 are of an order of magnitude expected based on SEM imaging (Fig. 3c) and previous membrane studies [6]. Fig. 3-3c shows how the membrane fibers overlap in a cross-hatched structure. The pores are the spaces between the fibers. Because they overlap, fibers sometime act as "floors" below pores defined by other fibers. The relative positions of the fibers determine the values of r and h. It is also noteworthy that seemingly much larger values of r and h appear in the wider-view SEM images in Fig. 3-1. However, these larger voids are a secondary pore structure. Their existence reduces overall porosity, but does not affect the pores that are relevant to LEP.

93

Table 3-4. Parameter values of the three models for LEP calculated using a non-linear least squares regression.

Model	Pore radius, r (nm)	Fiber radius, R (nm)	Floor height, h (nm)
Young-Laplace	229	---	---
Purcell	238	1059	---
New model	260	604	-264

3.4.2. Nylon-pDVB membrane for MD

The most significant finding from the first part of this study was that LEP_w can be positive for intrinsic ACA values as low as 90 ° but reduces to zero by approximately 60 °. In the second part of this study, we demonstrate the benefits of this finding with successful MD performance of a membrane surface-modified with pDVB. pDVB has an intrinsic advancing contact angle with water of approximately 95 - 105 °. It also has excellent material properties (environmentally-friendly, low-cost, robust etc.). Membranes with similar intrinsic ACAs, such as polypropylene, have been used for MD. However, materials with these contact angles are not typically used for hydrophobic surface-modification. In this work, we combine the benefits of surface-modification and clean chemistry to produce a successful, optimizable membrane for MD.

We used iCVD to prepare a nylon membrane with an ultra-thin (~ 10 nm) pDVB coating. We characterized the pDVB film using Fourier transform infrared (FTIR) spectroscopy (Fig. 3-10). The FTIR spectrum shows sp^3 –CH– and –CH_2– stretching bands between 3000 and 2840 cm^{-1} indicating the backbone chain. Bands between 900 and 680 cm^{-1} are characteristic of the pDVB's meta- and para- disubstituted aromatic rings [23,24,31].
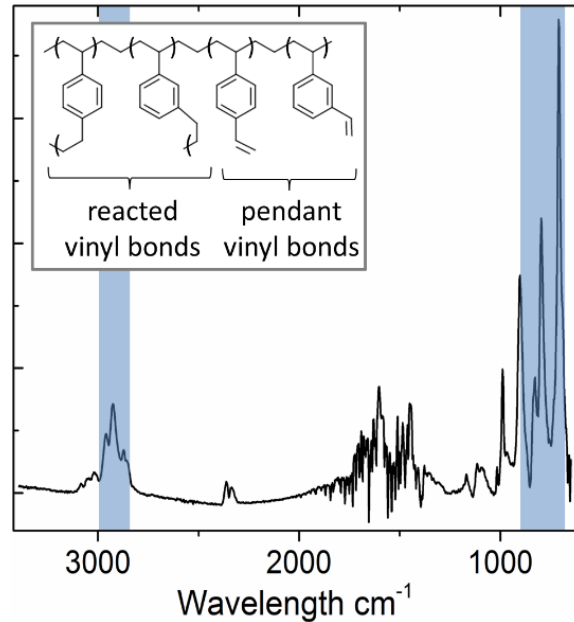
Fig. 3-10. FTIR spectrum for a thin film of iCVD-deposited pDVB. Shaded bands highlight some of the characteristic peaks of the pDVB. Inset shows the four types of pDVB repeat units.

While the intrinsic ACA of pDVB is low relative to pPFDA, it is more hydrophobic than untreated nylon. We first verified that surface-modification is necessary to prepare a nylon membrane suitable for MD. We qualitatively measured LEP_w of an as-purchased nylon membrane and a nylon-pDVB membrane using dyed deionized water as the test-solution (Fig. 3-11). As expected, the nylon membrane wetted spontaneously (Fig. 3-11a). In contrast, the nylon-pDVB membrane held water up to at least 200 kPa (Fig. 3-11b). This shows that $LEP_w \leq 0$ for the nylon membrane, and the pDVB was needed to give the membrane positive LEP_w.
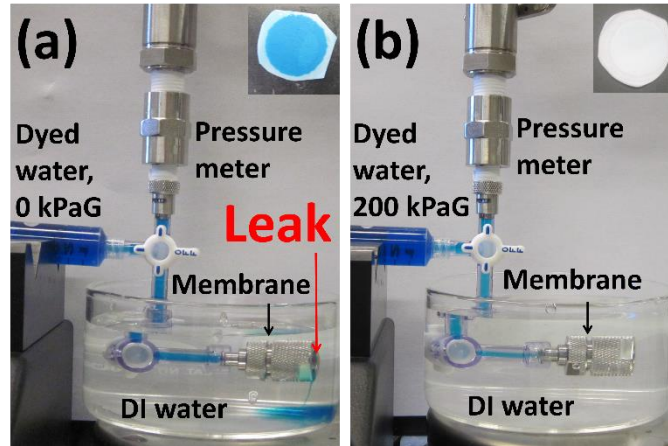
Fig. 3-11. (a) At no applied pressure, the as-purchased nylon membrane leaks visibly. The inset is the nylon membrane sample after testing. (b) Nylon-pDVB membrane with 200 kPaG applied pressure and no leakage. The inset is the nylon-pDVB membrane sample after testing.

Samples from the nylon-pDVB membrane were then tested using saline solution (35 g/L NaCl), finding LEP_w = 207 kPa (Fig. 3-6). The intrinsic ACA of this membrane with DI water was 96 °. These values for LEP_w and contact angle are lower than the values for the nylon-pDVB membrane in the first part of this study. This may be because of small differences in the coatings between the two nylon-pDVB membranes.

Membrane performance was quantified in a lab-scale direct contact membrane distillation (DCMD) desalination system. We determined the membrane distillation coefficient (specific distillate flux per unit partial pressure difference) by varying feed temperature at fixed distillate temperature (Fig. 3-12a). The resulting performance was 0.812 L/m²-hr-kPa. This is a little lower than the value for a commercial PVDF phase-inversion membrane with similar (220 nm) pore size [5]. Salt rejection and distillate flux over time were measured over the course of 18 hours at constant, mild conditions (50 °C feed, 25 °C distillate) (Fig. 3-12b). 99.99% salt rejection and 8

L/m^2-hr distillate flux were observed over the course of this test. This stable performance shows that the membrane does not wet, signifying that this nylon-pDVB membrane has a high enough LEP$_w$ for MD.
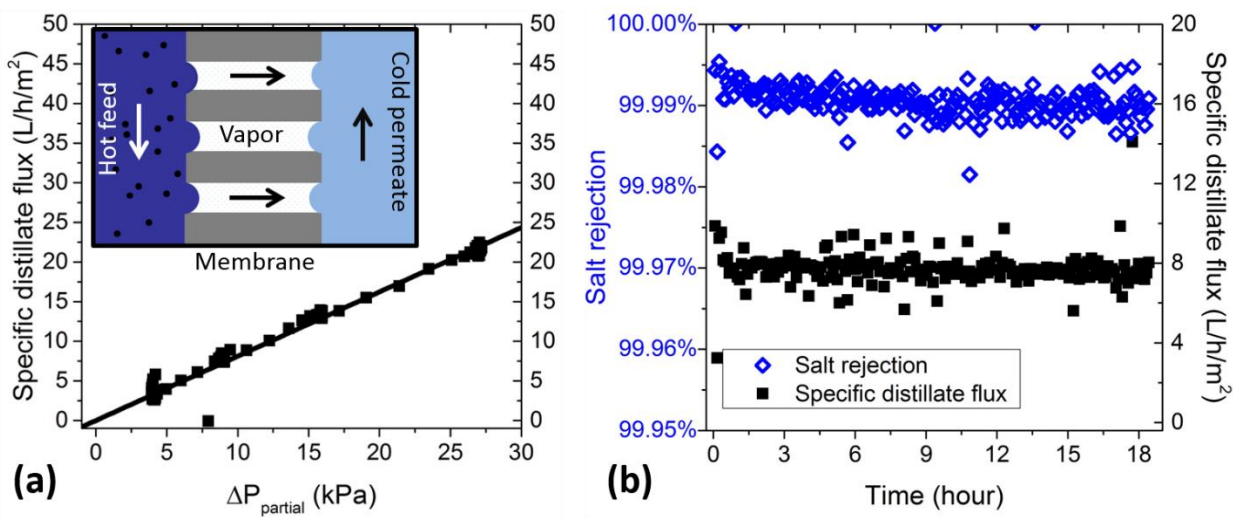
Fig. 3-12. (a) DCMD distillate flux as a function of the vapor pressure difference across the membrane. (b) Salt rejection and distillate flux over the course of 18 hours at constant conditions.

3.5. Conclusions

In this study, we quantified the effects of hydrophobicity on LEP for a surface-modified nylon phase-inversion membrane. We applied these findings to prepare a nylon-pDVB membrane that was successful in a lab-scale DCMD system. This study reveals the following points:

- Ethanol/water solutions and pPFDA and pDVB iCVD surface-treatments can be used together to infer LEP$_w$ for hydrophobocities ranging from 60 ° to 130 °. This is powerful because only two surface-modifying chemistries are needed to study an extremely wide range of contact angles.

- For the membrane in this study, LEP_w is always greater than 200 kPa for intrinsic advancing contact angle (ACA) $\geq$ 90 °. This indicates that high positive values of LEP_w can be achieved even at modest hydrophobicity.

- The Young-Laplace model for LEP does not describe this membrane, especially approaching 90 ° where it predicts LEP approaching 0 kPa. If the Young-Laplace model were assumed, decisions about surface-modification may over-emphasize maximizing hydrophobicity.

- The Purcell model for LEP accurately describes the experimental data for intrinsic ACA $\geq$ 90 °. However, contrary to observation, the Purcell model predicts that even very hydrophilic membranes will display a positive LEP.

- In this work, a new modified Purcell model for LEP was developed that successfully described the observed behavior over the full range of contact angles studied. The modification of the model accounts for interaction of the solution with membrane structures below the initially wetted surface. This model improves our understanding of liquid entry into membranes, and can aid the development of further improved MD membranes.

- We prepared an iCVD-treated, nylon-pDVB composite membrane with LEP_w significantly larger than that of an untreated nylon membrane. This composite membrane had successful DCMD performance with 99.99% salt rejection over 18 hours. This demonstrates that surface-modification can prepare a successful MD membrane using environmentally-friendly materials. Further optimization could further increase this membrane's distillate flux.

Appendix 3-A: Derivation of the modified Purcell model

The modified Purcell model for LEP is similar to the Purcell model but with a few key differences. The full derivation for the Purcell model can be found in the original paper [27]. A brief derivation of the modified Purcell model, illustrated using Fig. 3-A1, is below.
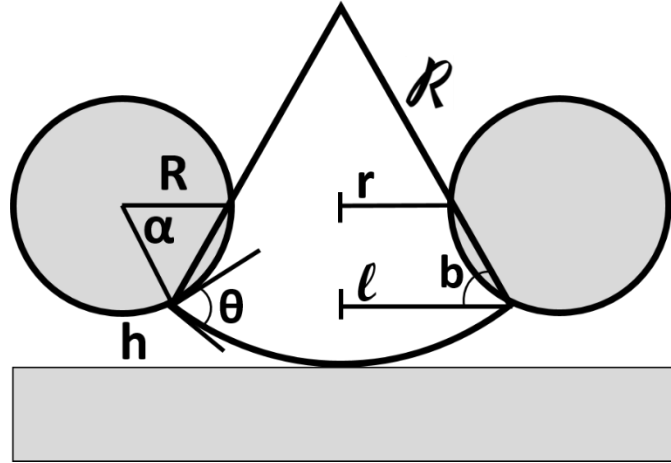
Fig. 3-A1. A pore for the new modified Purcell model with additional dimensions labeled.

The equation for the pressure drop across a meniscus with a circular cross-section is

$$\Delta P = \frac{2\gamma}{\mathfrak{R}}$$
(Eq. 3-A1)

where ΔP is the pressure drop, $\mathfrak{R}$ is the radius of curvature of the meniscus and γ is the surface tension of the liquid. To determine the liquid entry pressure of a pore, it is necessary to determine the value of $\mathfrak{R}$ at the moment of breakthrough. The following relationships between parameters can be observed geometrically from Fig. 3-A1:

$$\mathfrak{R} = \frac{l}{cos(b)}$$ (Eq. 3-A2)

$$l = r + R - Rcos(\alpha)$$ (Eq. 3-A3)

$$b = 180° - \theta - \alpha$$ (Eq. 3-A4)

Combining Eq. (3-A2), Eq. (3-A3) and Eq. (3-A4) produces

$$\mathfrak{R} = \frac{r + R(1 - cos(\alpha))}{-cos(\theta + \alpha)}$$ (Eq. 3-A5)

Combining Eq. (3-A1) and Eq. (3-A5) produces Eq. (3-3). This equation is valid for both the Purcell and the modified Purcell model.

To determine the maximum value of ΔP supported by the pore, the value of α at breakthrough must be calculated. This is where Purcell and the modified Purcell model diverge. For the Purcell model, α is determined by setting the derivative of Eq. (3-3) with respect to α to zero. This results in Eq. (3-4). In the new model, however, the liquid may contact the floor at a smaller value of α than the value calculated by Eq. (3-4). In this case, α at liquid entry is the value at which the meniscus contacts the floor. In this second case a geometric constraint is enforced to calculate α:

$$\mathfrak{R}(1 - sin(\alpha + \theta)) = R(1 - sin(\alpha)) + h.$$ (Eq. 3-A6)

Eq. (3-A5) and Eq. (3-A6) combine to produce Eq. (3-7). To calculate LEP according to the modified Purcell model, Eq. (3-3) is used along with Eq. (3-4) or Eq. (3-7), depending on whether detachment from the fiber or contact with the floor happens at the lower pressure.

Acknowledgments

References

[1] A.M. Alklaibi, N. Lior, Membrane-distillation desalination: Status and potential, Desalination. 171 (2005) 111–131.

[2] K.W. Lawson, D.R. Lloyd, Review: Membrane distillation, J. Membr. Sci. 124 (1997) 1–25.

[3] H. Susanto, Towards practical implementations of membrane distillation, Chem. Eng. Process. Process Intensif. 50 (2011) 139–150.

[4] P. Wang, T.-S. Chung, Recent advances in membrane distillation processes: Membrane development, configuration design and application exploring, J. Membr. Sci. 474 (2015) 39–56.

[5] A. Alkhudhiri, N. Darwish, N. Hilal, Membrane distillation: A comprehensive review, Desalination. 287 (2012) 2–18.

[6] E. Guillen-Burrieza, A. Servi, B.S. Lalia, H.A. Arafat, Membrane structure and surface morphology impact on the wetting of MD membranes, J. Membr. Sci. 483 (2015) 94–103.

[7] M. Gryta, Influence of polypropylene membrane surface porosity on the performance of membrane distillation process, J. Membr. Sci. 287 (2007) 67–78.

[8] M. Essalhi, M. Khayet, Surface segregation of fluorinated modifying macromolecule for hydrophobic/hydrophilic membrane preparation and application in air gap and direct contact membrane distillation, J. Membr. Sci. 417-418 (2012) 163–173.

[9] M. Khayet, J.I. Mengual, T. Matsuura, Porous hydrophobic/hydrophilic composite membranes, J. Membr. Sci. 252 (2005) 101–113.

[10] M. Qtaishat, M. Khayet, T. Matsuura, Novel porous composite hydrophobic/hydrophilic polysulfone membranes for desalination by direct contact membrane distillation, J. Membr. Sci. 341 (2009) 139–148.

[11] Y. Zhang, R. Wang, S. Yi, L. Setiawan, X. Hu, A.G. Fane, Novel chemical surface modification to enhance hydrophobicity of polyamide-imide (PAI) hollow fiber membranes, J. Membr. Sci. 380 (2011) 241–250.

[12] Y. Liao, R. Wang, A.G. Fane, Engineering superhydrophobic surface on poly(vinylidene fluoride) nanofiber membranes for direct contact membrane distillation, J. Membr. Sci. 440 (2013) 77–87.

[13] F. Guo, A. Servi, A. Liu, K.K. Gleason, G.C. Rutledge, Desalination by membrane distillation using electrospun polyamide fiber membranes with surface fluorination by chemical vapor deposition, ACS Appl. Mater. Interfaces. 7 (2015) 8225–8232.

[14] K. Honda, M. Morita, H. Otsuka, A. Takahara, Molecular aggregation structure and surface properties of poly(fluoroalkyl acrylate) thin films, Macromolecules. 38 (2005) 5699–5705.

[15] M. Ma, Y. Mao, M. Gupta, K.K. Gleason, G.C. Rutledge, Superhydrophobic fabrics produced by electrospinning and chemical vapor deposition, Macromolecules. 38 (2005) 9742–9748.

[16] D.M. Warsinger, A. Servi, S. Van Belleghem, J. Gonzalez, J. Swaminathan, J. Kharraz, et al., Combining air recharging and membrane superhydrophobicity for fouling prevention in membrane distillation, J. Membr. Sci. 505 (2016) 241–252.

[17] R.C. Buck, J. Franklin, U. Berger, J.M. Conder, I.T. Cousins, P. de Voogt, et al., Perfluoroalkyl and polyfluoroalkyl substances in the environment: Terminology, classification, and origins, Integr. Environ. Assess. Manag. 7 (2011) 513–541.

[18] A.M. Coclite, R.M. Howden, D.C. Borrelli, C.D. Petruczok, R. Yang, J.L. Yagüe, et al., 25th Anniversary Article: CVD Polymers: A new paradigm for surface modification and device fabrication, Adv. Mater. 25 (2013) 5392–5423.

[19] M. Gupta, V. Kapur, N.M. Pinkerton, K.K. Gleason, Initiated chemical vapor deposition (iCVD) of conformal polymeric nanocoatings for the surface modification of high-aspect-ratio pores, Chem. Mater. 20 (2008) 1646–1651.

[20] A. Asatekin, K.K. Gleason, Polymeric nanopore membranes for hydrophobicity-based separations by conformal initiated chemical vapor deposition, Nanoletters. 11 (2011) 677–686.

[21] S.H. Baxamusa, K.K. Gleason, Thin polymer films with high step coverage in microtrenches by initiated CVD, Chem. Vap. Depos. 14 (2008) 313–318.

[22] C.D. Petruczok, R. Yang, K.K. Gleason, Controllable cross-linking of vapor-deposited polymer thin films and impact on material properties, Macromolecules. 46 (2013) 1832–1840.

[23] J.L. Yagüe, K.K. Gleason, Enhanced cross-linked density by annealing on fluorinated polymers synthesized via initiated chemical vapor deposition to prevent surface reconstruction, Macromolecules. 46 (2013) 6548–6554.

[24] A. Liu, E. Goktekin, K.K. Gleason, Cross-linking and ultrathin grafted gradation of fluorinated polymers synthesized via initiated chemical vapor deposition to prevent surface reconstruction, Langmuir. 30 (2014) 14189–14194.

[25] B.-S. Kim, P. Harriott, Critical entry pressure for liquids in hydrophobic membranes, J. Colloid Interface Sci. 115 (1987) 1–8.

[26] M.C. García-Payo, M.A. Izquierdo, C. Fernandez-Pineda, Wetting study of hydrophobic membranes via liquid entry pressure measurements with aqueous alcohol solutions, J. Colloid Interface Sci. 230 (2000) 420–431.

[27] W.R. Purcell, Interpretation of capillary pressure data, J. Pet. Technol. 2 (1950) 11–12.

[28] R.R. Ferlita, D. Phipps, J. Safarik, D.H. Yeh, Cryo-snap: A simple modified freeze-fracture method for SEM imaging of membrane cross-sections, Environ. Prog. 27 (2008) 204–209.

[29] K. He, H.J. Hwang, I.S. Moon, Air gap membrane distillation on the different types of membrane, Korean J. Chem. Eng. 28 (2011) 770–777.

[30] A. Tuteja, W. Choi, J.M. Mabry, G.H. McKinley, R.E. Cohen, Robust omniphobic surfaces, Proc. Natl. Acad. Sci. 105 (2008) 18200–18205.

[31] E. Pretsch, P. Buhlmann, M. Badertscher, Structure determination of organic compounds: Tables of spectral data, 4th ed., Springer, Berlin, 2009.

CHAPTER FOUR

Effects of membrane morphology on MD membrane wetting

This chapter is based on work conducted collaboratively with the Professor Hassan Arafat laboratory at the Masdar Institute of Science and Technology [1]. Dr. Elena Guillen-Burrieza is the first author on the published study. In this chapter, all text is original. Figures which were reproduced from [1] are indicated with a citation. Original analysis and figures are also included. All data was previously published in [1].

Abstract

In membrane distillation (MD) a hydrophobic membrane acts as a barrier between feed and distillate streams. For the system to work, it is crucial that the membrane not allow liquid into its pores. This quality is quantified as the liquid entry pressure (LEP). LEP has been observed to depend on both surface-energy and membrane morphology. Multiple physics-based models for predicting LEP have been developed. However, their applicability across membranes of vastly differing morphologies has not been proven. This is a challenge when developing new membranes for MD, as the effects of various aspects of membrane morphology on LEP are not entirely known. To aid the development of new MD membranes, we studied the effects of membrane morphology on LEP. We considered five membranes with the same nominal pore size but varying morphology. We standardized their surface energies via initiated chemical vapor deposition (iCVD). However, despite being nominally similar, LEP for the five membranes ranged from 258 kPa to 442 kPa. This allowed us to analyze how differences in membrane morphology contribute to large variations in LEP. We first used a physics-based model with measured parameters values as the inputs. However, we were unable to find a combination of parameter values that resulted in accurate descriptions of LEP across the five membranes. As a second approach, we sought correlations between measured LEP values and morphological parameters. Using this method, we found that pore radius, the ratio of fiber to pore radius, surface porosity, geometric factor and membrane thickness all had strong correlations with LEP. These correlations can be used directly to steer MD membranes towards morphologies that favor higher LEP. Dr. Elena Guillen-Burrieza, Boor. S. Lalia and Professor Hassan A. Arafat contributed to this work.

4.1. Introduction

In membrane distillation (MD) a hydrophobic membrane acts as a barrier between feed and distillate streams [2–6]. A temperature difference across the membrane drives net diffusion of water vapor from the feed to the distillate. The membrane must allow this vapor flux, but prevent liquid from entering the pores. Preventing liquid entry is crucial for avoiding cross-contamination and reduced efficiency. To ensure entry is prevented, the liquid entry pressure (LEP) must be higher than any pressure gradients in the system.

Currently, there are no commercial membranes optimized for MD. Specialized high flux, high LEP membranes could improve MD efficiency and allow MD to reach its potential [5]. MD membrane development is thus an active area of research [7–12]. Many membrane fabrication methods can be employed to produce MD membranes. These include stretching, electrospinning, phase-inversion, sintering and track-etching. The resulting membranes have a vast range of morphologies and surface properties. Membrane performance depends on many of these properties, and each property affects multiple aspects of performance. Understanding the effects of the parameters is necessary to develop optimized membranes for MD. Given its importance to the basic functioning of the MD system, in this study, we focus specifically on how membrane morphology affects LEP.

To a first approximation, LEP increases with decreasing pore size and surface energy [13,14]. These parameters are thus given significant consideration when developing new membranes for MD. However, many additional membrane parameters have been observed to affect LEP. Multiple physics-based models describe LEP as a function of these parameters [15–21]. The models are derived for idealized pores, but have been successfully demonstrated to describe the LEP of real

(non-ideal) membranes. They have helped explain some important aspects of LEP, especially its dependence on surface energy [17]. However, in these studies, measured LEP values are used to infer the values of the membrane's physical parameters, rather than the other way around. This approach can be useful to build understanding about a membrane and fine-tune parameters such as pore size or surface energy. However, it does not determine whether the relationship between membrane parameters and LEP described in the models applies across larger differences in membrane morphology.

We studied the relationship between membrane morphology and LEP using five membranes as test-cases (Fig. 1). Two of the membranes are stretched poly(tetrafluoroethylene) (PTFE). Their pores are the negative spaces between long, thin PTFE fibers (Fig. 2d). Two additional membranes are phase-inversion membranes. One is poly(vinylidene fluoride) (PVDF) and the other is nylon. Their pores are also the negative spaces between fibers, but the pores are more circular than the stretched PTFE pores (Fig. 2b). The last membrane is a track-etched polycarbonate membrane, which has well-defined, cylindrical pores (Fig. 2c).
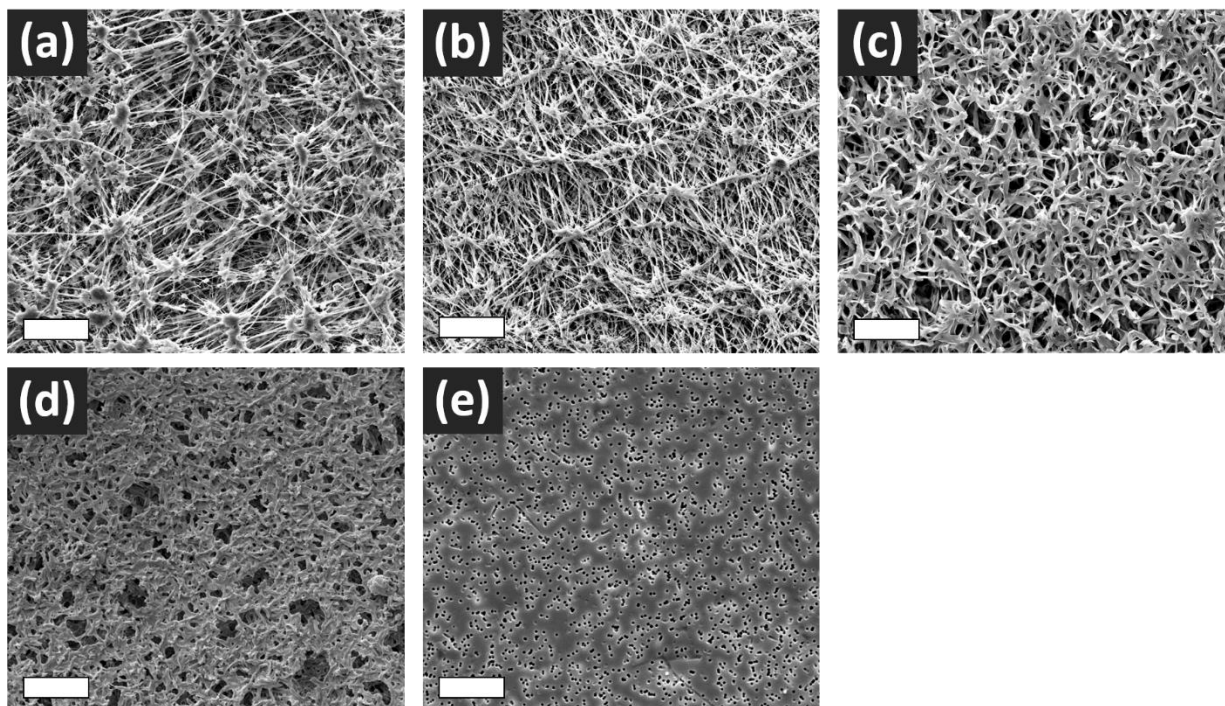
Fig. 4-1. SEM images of the top surfaces of the five membranes in this study: (a) PTFE-1, (b) PTFE-2, (c) PVDF, (d) Nylon, and (e) PC. Scale bars are 5 µm. Adapted from [1].

To isolate the effects of membrane morphology, we used surface-modification to standardize surface chemistry across the five membranes. We did this using initiated chemical vapor deposition (iCVD) [22]. iCVD can grow a conformal, ultra-thin (~20 nm) polymer film directly on a membrane surface including within the pores [23,24]. The polymer film coats all surfaces, changing the properties of the surface to the properties of the coating chemistry. iCVD has been used previously to modify membranes for MD and other applications. poly(1H, 1H, 2H, 2H - perfluorodecyl acrylate) (pPFDA) has been used most often when hydrophobic surface modification is needed [12,25,26]. In this study, we use a shorter-chained analog of pPFDA, poly(1H, 1H, 2H, 2H -perfluorooctyl acrylate) (pC6PFA) as the surface-modifying chemistry [27]. pC6PFA has an intrinsic advancing contact angle with water up to 135 ° making it hydrophobic

108

enough to prepare membranes with LEP in the range needed for MD [28]. With surface-energy standardized, the effects of just membrane morphology can be evaluated.

We use two different approaches to determine the effects of membrane morphology on LEP. Our first approach is to apply a physics-based LEP model across the five membranes using measured parameter values as the inputs. We do this to determine if the relationships between membrane parameters and LEP described in the theoretical models persist across membranes with very different constructions. Multiple physics-based models and idealized pore geometries have been proposed [15–21]. However, the models all appear to have the same underlying form illustrated in Fig. 4-2a. The equation for this general model is

$$\Delta P = \left(\frac{-2B\gamma}{r}\right)\frac{\cos(\theta+\alpha)}{1+R/r(1-\cos(\alpha))} \qquad \text{(Eq. 4-1)}$$

where ΔP is liquid entry pressure, γ is the surface tension of the liquid, r is pore radius, R is the fiber radius and θ is the contact angle between the solid and the liquid. B is a geometry factor where $B = 1$ for a pore with a circular cross-section (Fig. 4-2b, Fig. 4-2c), and $B = 0.5$ for a pore with a linear cross-section (Fig. 4-2d). α is the angle below horizontal at which the liquid meniscus pins prior to break-through. For an ideal, isolated pore, α is calculated according to

$$\sin(\theta + \alpha) = \frac{\sin\theta}{1+r/R}. \qquad \text{(Eq. 4-2)}$$

Throughout, we refer to this model as the "Purcell model", although the Purcell model does not include the variable, B. Depending on the values of the membrane parameters, many seemingly different pores are described by the Purcell model. Some of these pore types are illustrated in Fig. 4-2. Fig. 4-2a shows a cross-section of a generic pore described by this model. The pore in Fig. 4-2b has $R/r \sim 1$ and $B = 1$. This is similar to the pores in the Nylon and PVDF membranes. A

similarly shaped pore is also illustrated in the SEM image in Fig. 4-2e. Fig. 4-2c shows a pore with $R/r \rightarrow$ infinity and $B = 1$. This is similar to the pores in the PC membrane. Fig. 4-2d shows a pore with $R/r \sim 1$ and $B = 0.5$. This is similar to the pores in the PTFE membranes. Thus this one model approximately describes all of the general pore constructions that we encounter in this study. For this reason, we hypothesize that this model may be able describe the relationship between membrane parameters and LEP for the five membranes.
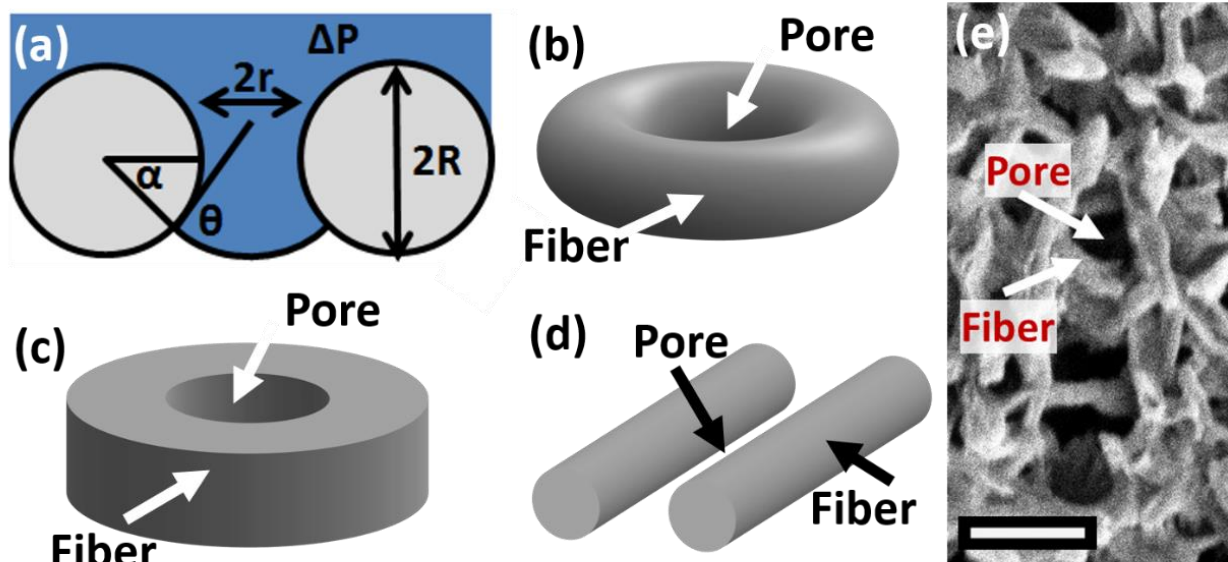
Fig. 4-2. A generalized form of the Purcell model for LEP for an idealized, isolated pore. (a) is a schematic of a single pore labeled with pore radius, r, fiber radius, R, contact angle, θ, and pinning angle, α. (b) is a pore with $R/r \sim 1$ and $B = 1$. (c) with $R/r \rightarrow$ infinity and $B = 1$ (d) is a pore with $R/r \sim 1$ and $B = 0.5$. (e) is an SEM image of a phase-inversion nylon membrane with a fiber and pore labeled. The scale bar is 1 μm. This membrane appears to have pores most similar to the schematic shown in (b).

Our second approach to determine the effects of membrane morphology on LEP is entirely empirically. We observed that there are many membrane parameters that are not accounted for in the Purcell model. While we do not have a physical model describing their role, we can still determine if these parameters are correlated with measured LEP values. To do this, we employed the following equation:

$$\Delta P = \sum c_i X_i \qquad \text{(Eq. 4-3)}$$

where ΔP is LEP. X_i are measured parameter values of the membrane (e.g. porosity and membrane thickness). c_i are coefficients for the parameter values determined using a multilinear regression of the five membranes' measured LEP values. We use Eq. (4-3) to test combinations of one or two parameters at a time, to determine their importance in determining LEP.

4.2 Materials and methods

4.2.1. Membranes

We evaluated five membranes in this study (Table 4-1, Fig. 4-1). Nominal pore size for all membranes was 200 nm. "PTFE-1" (Pall) and "PTFE-2" (Gore) are stretched poly(tetrafluoroethylene) (PTFE) membranes. Both have a thin active layer, supported by a thicker, structural layer. PTFE-1 has a polypropylene scrim support. PTFE-2 has a non-woven polypropylene support. "PVDF" (Thermoscientific) and "Nylon" (Sterlitech) are phase-inversion membranes made out of poly(vinylidene fluoride) (PVDF) and nylon respectively. Both membranes are thick enough (> 100 µm) to be unsupported. The last membrane, "PC" (Sterlitech), is track-etched polycarbonate. It is thinner than the other membranes (10 µm), but also unsupported.

Table 4-1. The five membranes in this study.

Membrane	Type	Supplier	Support layer
PTFE-1	Stretched	Pall	Scrim PP
PTFE-2	Stretched	Gore	Non-woven PP
PVDF	Phase-inversion	Thermoscientific	none
Nylon	Phase-inversion	Sterlitech	none
PC	Track-etched	Sterlitech	none

4.2.2. iCVD Polymer thin films

The five membranes were surface-modified using initiated chemical vapor deposition (iCVD). This standardized their surface energies, isolating the effects of morphology on LEP. iCVD was used to deposit ultra-thin (<20 nm) poly(1H, 1H, 2H, 2H-perfluorooctyl acrylate) (pC6PFA) films on all membranes. The iCVD films were grown in a custom-built reactor using the closed-batch configuration [29]. Closed-batch operation was used to achieve ultra-thin iCVD films. Membranes were placed in the chamber along with a silicon wafer substrate. The films deposited on the silicon allowed additional characterization to be performed. The thickness of the films on the silicon was monitored *in situ* using a laser interferometer. Total thickness on the silicon was < 20 nm for all films. Film thickness on the membranes is likely even less due to the membranes heating during the deposition.

The reaction chamber was cylindrical with a height of 38 mm and a diameter of 246 mm. The top was a removal 25 mm thick transparent quartz plate. The reactor was equipped with an array of 14 parallel filaments (80% Ni, 20% Cr) that could be resistively heated to 210 °C. The membranes

were taped to a stage maintained at 25 °C using a recirculating chiller/heater (NESLAB). The chamber was initially evacuated using a mechanical pump (45 CFM pumping speed, Alcatel). C6PFA monomer (Sigma-Aldrich, 97%), and t-butyl peroxide initiator (TBPO, Sigma-Aldrich, 98%) were introduced into the chamber. Room-temperature TBPO was introduced first, to a total chamber pressure of 80 mTorr[8]. C6PFA, heated to 80 °C, was then fed into the chamber until the total pressure in the chamber was 190 mTorr. After filling the chamber with initiator and monomer, all valves were closed, and allowed to sit for 2 min to allow mixing. The filament array was then turned on for 15 minutes. The heat from the filaments broke the initiator molecules into radicals. The radicals initiated polymerization of the monomer adsorbed to the membrane surface causing a polymer film to form. After 15 minutes, the chamber was evacuated and the filaments were turned off. When the system had cooled, the chamber was refilled and the deposition process was repeated. This increased the total thickness of the film. The PC membranes also received a third layer of polymer deposited on the other surface. This was done because the PC membranes as purchased are hydrophilic. This last deposition made it less likely that any hydrophilic material was left exposed.

4.2.3. Capillary flow porometry

Pore size distributions (PSD) of the membranes were measured using capillary flow porometry (CFP, Porous Materials Inc.). Similar methods have been described previously [30]. The wet/dry flow method was used. Membrane samples were wetted with a low surface tension liquid (Galwick™). They were then placed in a sealed chamber through which dry air was flowed. Initially, there was zero flow of gas through the membrane because all pores were blocked by the

---

[8] 1 Torr = 133.322 Pa

wetting fluid. The pressure of the air against the membrane was then increased. When the pressure was sufficient to remove the liquid from the largest pores, gas-flow through the sample started to occur. The pressure at which this occurred was used to calculate the maximum pore radius. As the pressure increased, smaller pores became unblocked and the gas flow rate increased until all pores became empty of wetting fluid. The rate of gas flow through the membrane was measured at each applied pressure. The amount that the flow increased at each pressure yielded the relative volume of pores with each radius. The pressure at which the flow rate was half the total flow rate was used to calculate the average pore radius.

4.2.4. Contact angle

Contact angle was measured using a contact angle goniometer (EASYDROP, Krüss). All contact angle measurements, were taken at room temperature (around 25 °C) using deionized (DI) water. At least five locations on each sample were tested and averaged. Average standard deviation was 2.2 °. Apparent contact angles were measured directly on the membranes. Intrinsic contact angles were measured on silicon treated with the same polymer film. For dynamic contact angle (advancing and receding), a 1 µL drop was placed on the surface. Volume was increased/decreased from 1 to 20 µL at a rate of 5 µL/min.

4.2.5. Scanning electron microscope imaging

The membranes were imaged with a Quanta FEG 250 Scanning electron microscope (SEM, FEI) operating at ~5 KeV. The samples were gold and palladium coated using a GATAN, Model 682, Precision etching coating system (PECS). Image analysis using ImageJ® software was performed to calculate surface porosity.

4.2.6. Atomic force microscope imaging

Atomic force microscopy (AFM) (Asylum Research, MFP-3D™ Stand Alone) was used to characterize the topography of the membranes. The samples were cut into small square pieces (1 cm^2) and pasted on a glass substrate. A silicon tip with radius ≈ 10 nm, resonance frequency ≈ 70 kHz and spring constant ≈ 2 N/m (non-contact tapping mode) was used. All measurements were at ambient temperature and humidity.

4.2.7. Liquid entry pressure

A custom-built computer-controlled device was used to measure liquid entry pressure (LEP). The wetting liquid chamber was filled with DI water. A membrane sample (3 cm x 3 cm) was placed above the liquid chamber with the active surface facing down (in contact with the liquid). Pressure was applied at a rate of 10.3 kPa/min. When the first water drop was detected visually on the dry surface of the membrane, the corresponding pressure was recorded as the LEP. At least three samples from each membrane were tested and the results averaged. A new, dry membrane sample was used for each iteration.

4.3. Results and discussion

We characterized the five membranes for their physical parameters. These measurements were used as inputs into the Purcell model for LEP. This determined how the model's relationships between parameters and LEP hold for the five membranes. An expanded set of measurements were then analyzed using multilinear regression of the measured LEP values. This showed the relative importance of various membrane parameters in determining LEP. When evaluating the membrane parameter values, we observed that their values were highly dependent on the definitions and

measurement methods employed. Thus, for some of the parameters, we evaluated their values in multiple ways in order to study the effects of the variation on the ability of the models to predict LEP.

4.3.1. Evaluating membrane parameters

4.3.1.1. Pore radius

Pore size distributions were measured before and after iCVD treatment using capillary flow porometry (CFP). Average and maximum pore radii are shown in Table 4-2. Full pore size distributions for PTFE-1, PVDF and PC before and after iCVD treatment are shown in Fig. 4-3.

Table 4-2. Average (r_{avg}) and maximum (r_{max}) pore radii before and after iCVD treatment.

Membrane	r_{avg}, uncoated (nm)	r_{avg}, iCVD (nm)	r_{max}, uncoated (nm)	r_{max} iCVD (nm)
PTFE-1	106	106	226	227
PTFE-2	87	72	149	156
PVDF	106	101	254	252
Nylon	139	107	460	229
PC	85	81	97	88
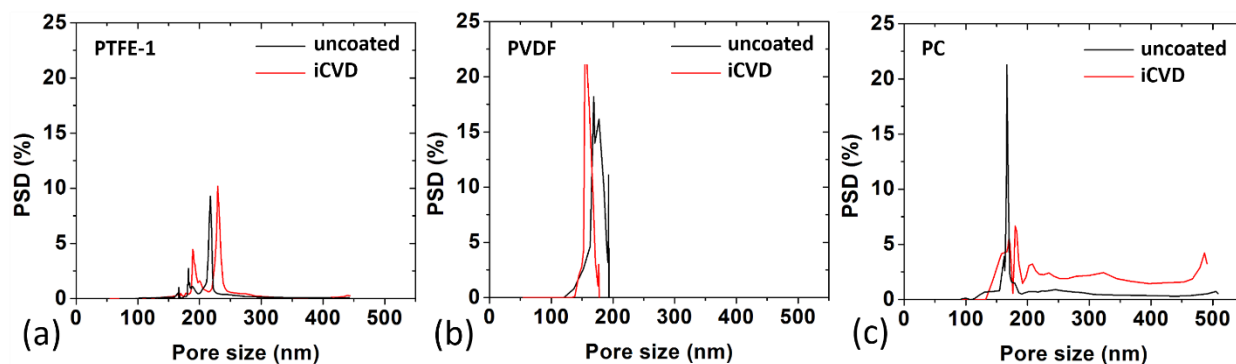
Fig. 4-3. Pore size distribution (PSD) before (black) and after (red) iCVD treatment for (a) PTFE-1, (b) PVDF and (c) PC. Adapted from [1].

The five membranes as-received have the same nominal pore radius (100 nm). Despite this, the uncoated r_{avg} and r_{max} values vary widely. The average uncoated r_{avg} across the five membranes is 93 nm with a standard deviation of 16 nm. The average uncoated r_{max} is 190 nm with a standard deviation of 68 nm. The difference between the nominal pore radii and the measured pore radii (r_{avg} and r_{max}) is likely due to differences in how pore radius is defined and measured. This introduces uncertainty into the implementation of LEP models.

As expected, the iCVD polymer coating reduces r_{avg} and r_{max} for the five membranes. Change in r_{avg} ranges from 0 nm for the PTFE-1 membrane to 32 nm for the Nylon. Change in r_{max} ranges from -7 nm for PTFE-2 to 231 nm for the Nylon. The thickness of the iCVD coating is unclear from this data but based on the change in average pore radius, it appears to be on the order of 10 nm. The existence of membranes with zero or negative change in pore radius indicate that there is significant noise in these measurements of pore size.

Full pore size distributions for PTFE-1, PVDF and PC are shown in Fig. 4-3. These three membranes are examples of stretched, phase-inversion and track-etched membrane types. The widths of the pore size distributions differ between the three membranes. The track-etched PC membrane has the narrowest pore size distribution. This is expected because the chemical etching process is uniform over the surface of the membrane. The stretched PTFE membrane and the phase-inversion PVDF membranes have wider pore size distributions. The pore size distributions for all three membranes are not smooth and the data appears noisy. We suspect that additional data from more samples of each membrane would smooth out the curves. This would strengthen our confidence in the values of r_{avg} and r_{max} and make the contribution of the iCVD to pore radius more clear.

The pore sizes determined using CFP (Table 4-2) differ from the pore sizes seen in the SEM images of the same membranes (Fig. 4-1). In Fig. 4-1, many pores appear larger than 100 nm radius at the surface, especially for the PTFE-1, PTFE-2 and Nylon membranes. This shows the importance of the pore structure within the membranes to determine average and maximum pore size.

4.3.1.2. Contact angle

The apparent contact angles for the five membranes after iCVD-treatment are shown in Table 4-3. The intrinsic advancing contact angle (ACA) of the iCVD polymer film was also measured on a silicon wafer that was treated along with the membranes. The intrinsic ACA for this film was 106 °. Apparent contact angles were measured on the membranes themselves. All apparent contact angles are higher than the corresponding intrinsic values. This suggests that Cassie-Baxter wetting

occurs for all membranes. The apparent contact angle of a surface with Cassie-Baxter wetting is [31]

$$\cos \theta_A^* = f_1 cos\theta_A - f_2 \qquad\qquad \text{(Eq. 4-4)}$$

where $\theta_A{}^*$ is the apparent ACA, θ_A is the intrinsic ACA, f_1 is the area of the solid-liquid interface and f_2 is the area of the solid-air interface that exists over the pores. The membranes have similar ACAs except for the PC membrane. The PC membrane has a flatter surface than the other membranes. This reduced roughness causes it to have a lower value of f_1 and a lower apparent ACA.

Table 4-3. Apparent contact angles with water of the five membranes after iCVD treatment.

Membrane	Advancing (°)	Static (°)	Receding (°)
PTFE-1	147	134	96
PTFE-2	141	130	105
PVDF	143	130	70
Nylon	152	153	141
PC	128	117	45

4.3.1.3. Geometric factor, B and fiber radius, R

The geometric factor, B relates to the ratio between pore perimeter and pore area [15]. Pores with a circular cross-section (Fig. 4-2b and 4-2c) have $B = 1$. More linear pores (Fig. 4-2c) have $B = 0.5$. For PTFE-1 and PTFE-2, we estimate that $B = 0.5$ as was done by Kim and Harriot [17]. For the PC membrane the cylindrical pores mean that $B = 1$. For the PVDF and Nylon membranes we estimate $B = 0.8$ and $B = 0.9$ respectively based on inspection of Fig. 4-1.

The variable, R/r, is the ratio between membrane fiber radius and pore radius (Fig. 4-2). We determined three possible values of R/r for each membrane (Table 4-4). One of these values was calculated using the Cassie-Baxter equation. The other two were calculated from AFM and SEM data. We also considered values from the literature.

We first calculate the value of R/r using the Cassie-Baxter equation. For a surface composed of parallel fibers (Fig. 4-2d), the Cassie-Baxter equation takes the form [32]

$$cos(\theta_A^*) = -1 + \frac{1}{D^*}[(\pi - \theta_A)cos\theta_A + sin\theta_A] \qquad \text{(Eq. 4-5)}$$

where $\theta_A{}^*$ is the apparent ACA and θ_A is the intrinsic ACA. D^* is a dimensionless spacing ratio where $D^*=1+ 1/(R/r)$. The assumption that the membranes resemble Fig. 4-2d holds for PTFE-1 and PTFE-2, but not for the other three membranes. Regardless, using Eq. (4-5) and the ACA values in Table 4-3, we calculated values of R/r for each membrane (Table 4-4). The results range from 0.24 to 1.74. Values of $R/r < 1$ indicate that the membrane fibers are narrower than the pores themselves. It is difficult to assess whether these values are reasonable for PTFE-1, PTFE-2, PVDF and Nylon. For the PC membrane, whose cylindrical pore structure most resembles a membrane with $R/r \rightarrow$ infinity (Fig. 4-2c), the value calculated by Eq. (4-5) is much smaller than expected. This is not surprising given the assumption in Eq. (4-5) that the pore structure is fibrous (Fig. 4-2d).

Table 4-4. Membrane parameters: Total thickness, L (manufacturer specified, includes the support layer), Geometric factor, B (estimated from SEM), surface porosity, ε (measured from SEM), R/r (calculated using the Cassie-Baxter (C-B) equation), R/r (calculated from AFM), R/r (calculated from SEM), R/r (from the literature), LEP (measured).

Membrane	L (µm)	B (SEM)	Surface porosity	R/r (C-B)	R/r (AFM)	R/r (SEM)	R/r (literature)	LEP (kPa)
PTFE-1	280	0.5	0.331	0.36	1.4	2.0	0.5 − 1 [17], 0.92 [18], 35 − 48 [33]	381
PTFE-2	180	0.5	0.365	0.58	2.5	1.7	see PTFE-1	442
PVDF	200	0.8	0.231	0.50	5.0	1.1	6 [18], 18-33 [33]	276
Nylon	120	0.9	0.193	0.24	3.5	1.3	2.3 (Ch 3)	258
PC	10	1.0	0.071	1.74	7.5	2.8	→ inf (Ch 2)	298

An alternative method of estimating R/r uses imaging. Fig. 4-4 shows AFM topographic profiles and SEM binary images for the five membranes. R/r is calculated from the AFM topographic profiles by considering the valleys to be pores (radius, r) and the peaks to be fibers (radius, R). R/r is the average ratio of the peak and valley widths. This method does not make assumptions about the shape of the pores ($B = 0.5$ or $B = 1$), but does assume that the pore walls are rounded (unlike the PC membrane). R/r values calculated from the AFM images were larger than the values calculated using the Cassie-Baxter equation. For instance, the PVDF membrane predicts $R/r = 5.0$.

This would indicate that the fibers are five times wider than the pores. The values obtained using this method could be plausible for all but the PC membrane.

A third method to determine *R/r* uses SEM imaging. Image analysis of the binary SEM images of the five membranes in Fig. 4-4 was used to determine surface porosity (void fraction at the surface) (Table 4-4). The measured surface porosity is significantly lower than the bulk porosities of the same membranes as specified by the manufacturer (~90% for PTFE-1 and PTFE-2, ~70% for PVDF and Nylon, 10% for PC). This is likely due to large void spaces within the membranes. If the pores are long and narrow ($B = 0.5$) it can be determined that

$$\frac{R}{r} = \frac{1}{\varepsilon} - 1 \qquad\qquad \text{(Eq. 4-6)}$$

where ε is porosity. If the pores are square ($B = 1$), it can be determined that

$$\frac{R}{r} = \left(\frac{1}{\varepsilon}\right)^{1/2} - 1 \qquad\qquad \text{(Eq. 4-7)}$$

Assuming that the PTFE membranes have $B = 0.5$ and the other three membranes have $B = 1.0$, values of *R/r* can be calculated from the measured surface porosities (Table 4-4). As with the method using AFM measurements, this method assumes rounded pore walls and so is not suitable for the PC membrane. The values calculated from the SEM images are most similar to those calculated from the AFM data, but with less range in the values.
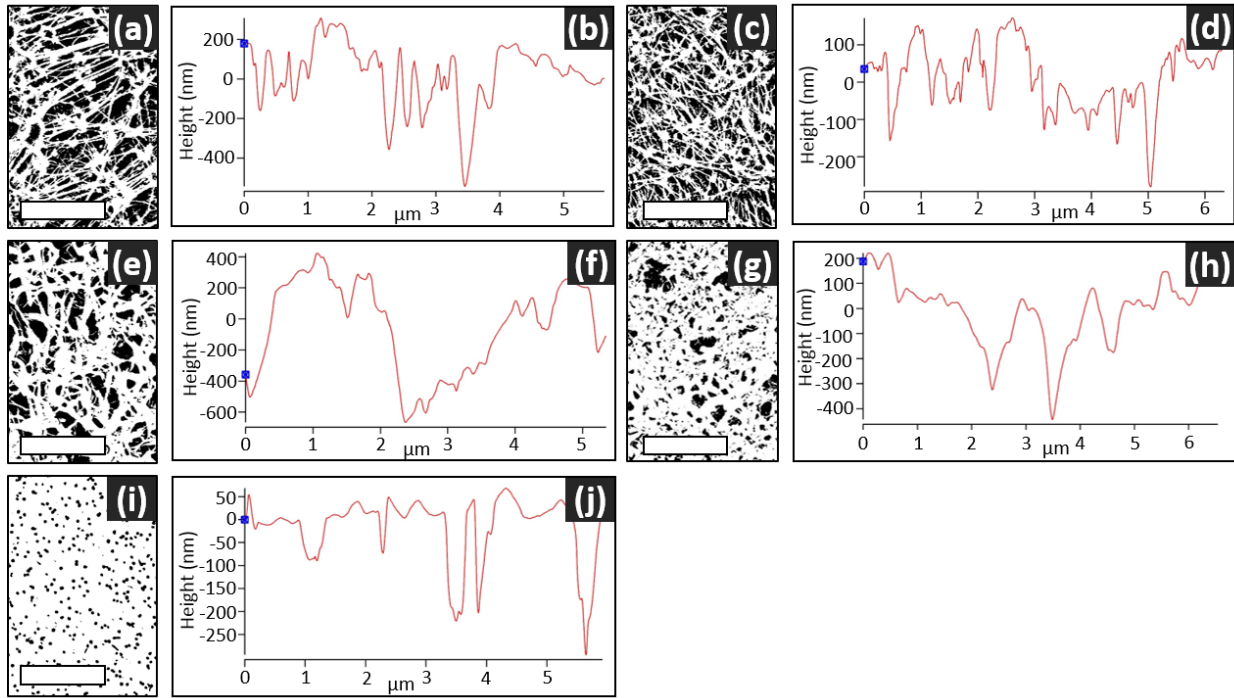
Fig. 4-4. SEM binary images and AFM topographic profiles of the five membranes after iCVD coating. Membranes are (a, b) PTFE-1, (c, d) PTFE-2, (e, f) PVDF, (g, h) nylon, and (i, j) PC. The scale bar is 5 µm for all SEM images. Adapted from [1].

The R/r values calculated using Cassie-Baxter, AFM and SEM were compared to the values found in the literature for similar membranes [17,18,33]. The values for R/r in the literature were determined using regressions for measured LEP values. The only exception is the PC membrane studied in Chapter two of this thesis. In that study, the value of R/r was inferred from the manufacturing process which produces cylindrical pores resembling Fig. 4-2c. Excluding the values from [33], which appear to be outliers, the AFM and literature R/r values are the most similar, including decreasing from largest to smallest R/r in the same order. We use the AFM values in future calculations, while acknowledging that it is a source of uncertainty in our analysis.

4.3.1.4. Liquid entry pressure

We measured liquid entry pressure (LEP) visually for the five membranes. The results are given in Table 4-4. LEP values ranged from 258 kPa to 442 kPa. PTFE-2 has the highest LEP and Nylon has the lowest. We expect that all five membranes have high enough LEP for MD. However, this large range could be problematic if the values were centered even 100 kPa lower than they were.

4.3.2. Evaluating the Purcell model

We evaluated the Purcell model [Eq. (4-1) and Eq. (4-2)] for the five membranes using the measured parameter values as the inputs. Each plot in Fig. 4-5 shows the Purcell LEP value (x-axis) plotted against the measured LEP value (y-axis) for the five membranes. In the Purcell model, LEP is a function of four variables: *B*, *r*, *θ* and *R/r*. For all plots in Fig. 4-5, we assume that *B* is the value from Table 4-4. Each plot in Fig. 4-5 uses different assumptions about the remaining three variables (assumptions shown above each plot). We do this because, unlike idealized pores, membranes do not have clear definitions for each variable. Testing multiple combinations allows us to determine which definitions are most relevant for predicting LEP. The value of R^2 in the top left corner of each plot is the sum of the squares of the differences between the measured and modeled LEP values.
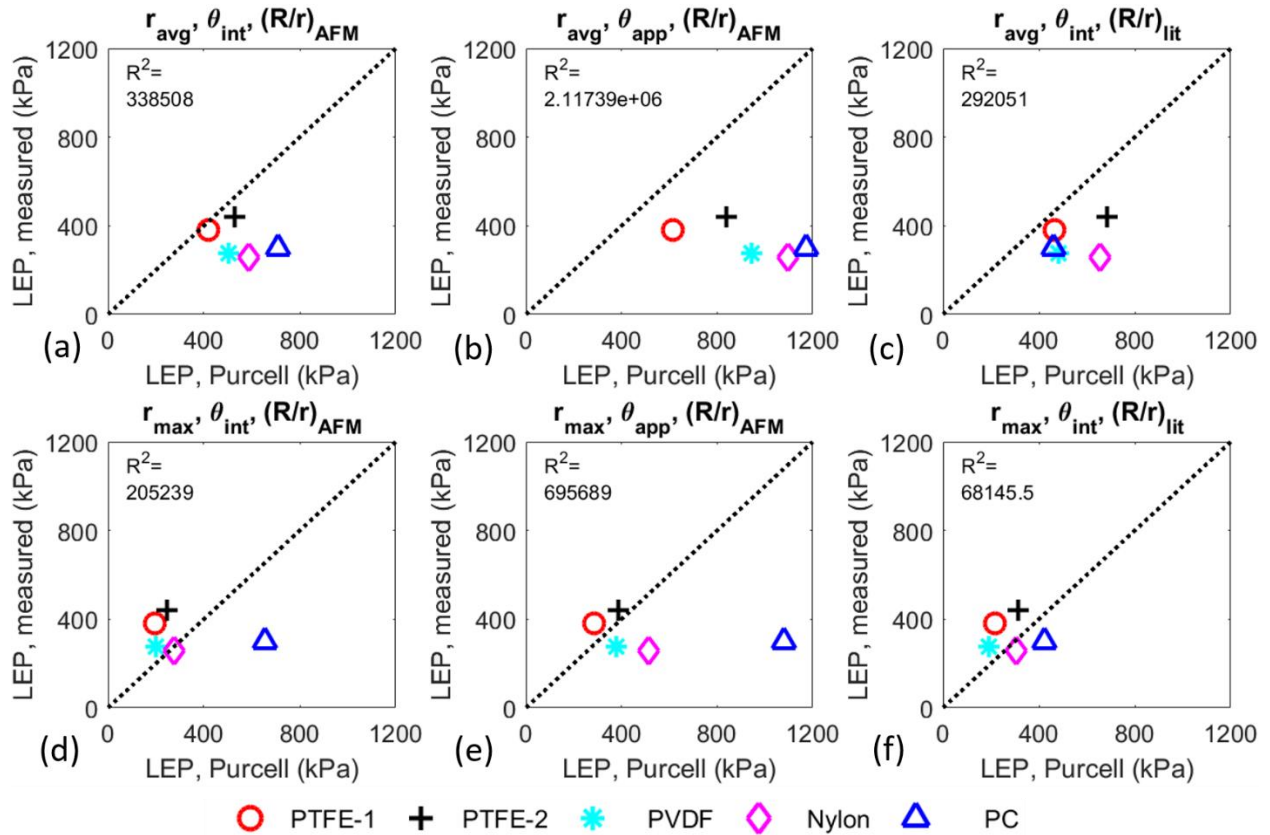
Fig. 4-5. Measured and calculated (Purcell) values of LEP. Each plot assumes a different set of values for r, θ and R/r (shown above each plot). R^2 in the top left corner of each plot is the sum of the squares of the differences between the measured and modeled LEP values.

We did not find any combination of parameter definitions for which the Purcell model agreed with the measured values. However, some definitions appear more useful than others. For instance, there is better agreement when $r = r_{max}$ rather $r = r_{avg}$. This is because r_{max} brings the modeled values closer in magnitude to the measured values. This follows our intuition that r_{max} is more important to LEP than r_{avg}. Liquid enters the largest pores at lower pressures than it enters the average pores. LEP should be detected at these lower pressures, tying it to r_{max} rather than r_{avg}. However, neither definition of r predicts the same order of increasing LEP from membrane to membrane seen for the measured values.

For contact angle, we consider advancing (rather than static or receding) definitions. This is because LEP involves the process of liquid advancing into the pores. When comparing intrinsic and apparent ACA, both have arguments for being more relevant to LEP. The apparent ACA, measured on the membrane itself, captures the roughness of the membrane fibers. This roughness is not captured when measuring the intrinsic ACA on a silicon surface. However, apparent ACA also incorporates the roughness of the membrane surface on the scale of many microns. This roughness should not be relevant to liquid entering a single pore. The apparent ACA thus likely over-predicts the applicable contact angle for predicting LEP. Because it does not include any membrane roughness, the intrinsic ACA likely under-predicts the applicable contact angle. We found that using the intrinsic ACA in the Purcell model predicts LEP values closer in magnitude to the measured values. However, again, neither predict the membranes' LEP values relative to each other. For R/r, we tested both the AFM and the literature values. These value are similar although the literature has more realistic value of R/r for PC. This one difference reduces the overall error of the model in Fig. 4-5c and 5f but does not cause any other significant changes.

Overall, the best agreement is seen in Figure 4-5f ($r = r_{avg}$, θ = intrinsic ACA and R/r = literature values). However, even then, the errors are large, and the model does reflect the observed differences in LEP between the membranes. Based on its roots in physics and its previous successes, we believe that the relationships between membrane parameters and LEP described in this model are meaningful. It is possible that the correct combination of parameter definitions would reveal this. However, with so many unknowns we could not verify these relationships.

4.3.3. Empirical correlations between parameters and LEP

In light of the limitations in applying the Purcell model, we take a second approach to relate membrane morphology to LEP. In this approach we focus on correlations between membrane parameters and LEP rather than a physical model. Using Eq. (4-3), we test one or two parameters at a time to determine their correlations with LEP. One of the parameters is always the inverse of pore radius. We always include the inverse of pore radius because we found that its effects overshadowed the effects of other parameters if not included. Other tested parameters include the ratio of fiber to pore radius (*R/r*), surface porosity (*ε*), the geometric factor (*B*), and membrane thickness (*L*). All parameters were normalized to a maximum value of one. The inverse of some parameters (pore radius, *R/r* and *B*) were used to make all correlations positive. Other parameters (roughness, apparent ACA, etc.) were also considered, but only parameters with strong correlations to LEP are discussed.

Six plots are shown in Fig. 4-6, each corresponding to a different set of parameters. In each plot, LEP calculated using Eq. (4-3) (x-axis) is plotted against the measured LEP values (y-axis). The parameters used for each plot are shown above the plots. The values of R^2 are the sums of the squares of the differences between the measured and calculated LEP. The coefficients and R^2 values for the six sets of parameters are shown in Table 4-5. Each row of Table 4-5 corresponds to the plot from Fig. 4-6 with the same name.
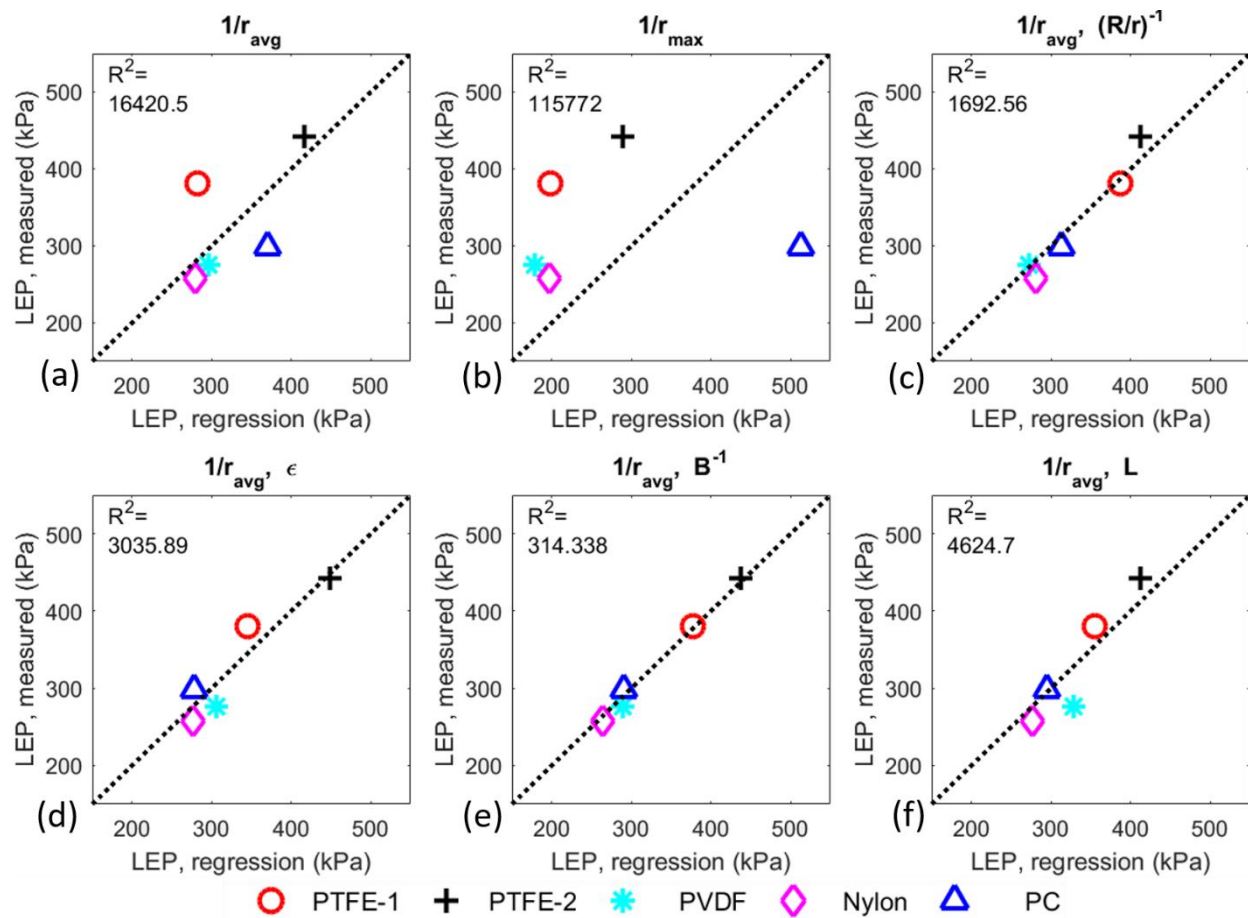
Fig. 4-6. Measured LEP versus LEP calculated using linear combinations of membrane parameters (Eq. (4-3)). The parameters for each plot are shown above the plots. (a) and (b) have just one parameter (X_1). All other plots have two parameters (X_1 and X_2). R^2 in the top left corner of each plot is the sum of the squares of the differences between the measured and modeled LEP values.

Table 4-5. The six combinations of variables shown in Fig. 4-6. X_1 and X_2 are two parameters in Eq. (4-3). c_1 and c_2 are their coefficients. R^2 is the sum of the squares of the differences between the measured and modeled LEP values.

	X_1	X_2	c_1	c_2	R^2
(a)	$1/r_{avg}$	---	416	---	16421
(b)	$1/r_{max}$	---	512	---	115772
(c)	$1/r_{avg}$	$(R/r)^{-1}$	315	172	1692
(d)	$1/r_{avg}$	ε (surface)	275	174	3036
(e)	$1/r_{avg}$	B^{-1}	184	126	314
(f)	$1/r_{avg}$	L	327	133	4625

Fig. 4-6a and Fig. 4-6b each have one parameter, $X_1 = 1/r_{avg}$ and $X_2 = 1/r_{max}$ respectively. We consider these parameters on their own because pore size is theoretically the most important parameter for determining LEP. However, examining Fig. 4-6a and Fig. 4-6b, the inverse of pore radius alone does not correlate particularly well with LEP. For r_{avg}, the data clusters around, but not on, the line of agreement. For r_{max}, the values for all but the PC membrane fall almost in a line, but the PC membrane is such an outlier that it distorts the correlation. For the remaining plots, we use the inverse of r_{avg} as X_1 because it has a smaller total error. However, r_{max} could also have been used.

In Fig. 4-6c, $X_1 = 1/\ r_{avg}$ and $X_2 = (R/r)^{-1}$ where R/r was determined using AFM imaging. This combination produces a good fit, indicating that these two variables are both important for LEP.

This is in agreement with the Purcell model which predicts increasing values of LEP with increasing $(R/r)^{-1}$.

In Fig. 4-6d, $X_1 = 1/ r_{avg}$ and $X_2 =$ surface porosity (ε). Porosity is a property of the overall membrane, not the individual pores, so porosity is not present in any existing models for LEP. However, the strong correlation for this combination of parameters indicates that porosity is relevant to LEP. We expect this is explained by indirect effects: According to Eq. (4-6) and Eq. (4-7), increasing surface porosity decreases (R/r). In turn, according to the Purcell model, decreasing R/r increases LEP. In this way, this seemingly irrelevant parameter of membrane morphology has a physical basis for being a strong predictor of LEP.

In Fig. 4-6e, $X_1 = 1/ r_{avg}$ and $X_2 =$ the inverse of the geometric factor (B^{-1}). In most LEP models, LEP is proportional to the geometric factor, B. However, we found that it is the inverse of B that correlates (almost exactly) with increasing LEP. While we expect that this is partially coincidence, there is likely an underlying reason for the correlation as well. Like with surface porosity, B also leads back to the value of R/r. When calculating R/r from surface porosity, we found that increasing B from 0.5 to 1.0 means that Eq. (4-7) rather than Eq. (4-6) is used to calculate R/r. Eq. (4-7) predicts lower values of R/r for a given porosity than does Eq. (4-6). Thus increasing B lowers the predicted value of R/r, indirectly reducing LEP.

In Fig. 4-6f, $X_1 = 1/ r_{avg}$ and $X_2 =$ membrane thickness (L). Membrane thickness is another parameter of membrane morphology that is not pore specific and does not appear in existing models for LEP. Further, it is a tenant of our understanding of LEP that it is independent of

membrane thickness. It is thus surprising that there is a positive correlation between membrane thickness and LEP. A possible explanation is that thicker membranes do not increase resistance to initial liquid entry but do prevent liquid from fully traversing the pores. This would delay detection of liquid entry, increasing the measured LEP. The increase in LEP with increased thickness may thus be an artifact of the measurement methods. However, preventing liquid from fully traversing the membrane could have a positive effect on MD system performance: If liquid enters the membrane but does not traverse it, cross-contamination between feed and distillate is prevented and the salt rejection of the system increases.

The correlations in Fig. 4-6 have practical implications. The relationship with $(R/r)^{-1}$ is not surprising in light of the Purcell model. However, the correlations with surface porosity and the geometric factor are especially interesting. It is easier to measure or design for surface porosity and pore shape than it is to measure or control R/r. Using B and surface porosity as proxies for R/r can make it easier to design or identify membranes with high LEP. The relationship between membrane thickness and LEP also has practical implications. Increasing thickness may reduce the possibility of cross-contamination at high pressures. However, the cost of increased thickness to other aspects of membrane performance, especially permeability, must also be considered.

Overall, all correlations except for membrane thickness, lead back to the relationships for LEP with respect to pore radius and R/r described by the Purcell model. This strengthens our belief in these relationships despite the findings that the Purcell model cannot be used directly to predict LEP.

4.4. Conclusions

We studied the relationships between membrane morphology and LEP using five test membranes. These membranes were: Two stretched PTFE membranes, a phase-inversion PVDF membrane, a phase-inversion nylon membrane and a track-etched polycarbonate membrane. We used iCVD to standardize the surface chemistry of these membranes with ultra-thin pC6PFA films. The resulting membranes had the same nominal pore size and surface chemistry, but their measured LEP values ranged from 258 kPa to 442 kPa. This implies that aspects of their morphology beyond nominal pore size have a strong effect on LEP.

We applied the Purcell model to the five membranes using the measured parameter values of the membranes as the inputs. We found that, using these inputs, we could not prove or disprove if the model was descriptive of the five membranes. Instead we found that the model was sensitive to the specific definitions of the parameters about which there is much uncertainty. We also took another, more empirical approach, using multilinear regressions to determine the correlations between membrane parameters and LEP. We found that the ratio of fiber and pore radius (R/r), surface porosity (ε), geometric factor (B) and membrane thickness (L) all had strong correlations with LEP.

Using these correlations, we can predict membrane characteristics for which LEP is expected to be maximized. Small fiber size, high porosity, long-narrow pore shape ($B = 0.5$) and high membrane thickness are all correlated with high LEP. This indicates that stretched and electrospun membranes, both of which have small fibers, high porosity and $B = 0.5$ are favorable for high LEP. Track-etched polycarbonate membranes which have very high fiber diameter ($R/r \rightarrow$ infinity), low

porosity and $B = 1$ are extremely unfavorable for high LEP. Other membrane types such as phase-inversion and sintered membranes are between these two extremes. In addition, membranes of any type may be made to have higher LEP by manipulating morphology parameters such as by increasing membrane thickness or decreasing fiber diameter when possible.

In order to further strengthen these conclusions, we recommend adding additional membranes to this study. These could include electrospun and sintered membranes as well as additional stretched and phase-inversion membranes. By increasing the number of membranes in the study, factor analysis could be used to rigorously determine the number of independent variables that define LEP. The method of using iCVD to standardize surface energy could also be extended to determine the effects of membrane morphology on other aspects of membrane performance including fouling, permeability and vapor flux in an MD system. The findings from this study and any extensions can be used to inform decisions about membrane morphology that ensure high LEP and improved overall MD system performance.

References

[1] E. Guillen-Burrieza, A. Servi, B.S. Lalia, H.A. Arafat, Membrane structure and surface morphology impact on the wetting of MD membranes, J. Membr. Sci. 483 (2015) 94–103.

[2] A. Alkhudhiri, N. Darwish, N. Hilal, Membrane distillation: A comprehensive review, Desalination. 287 (2012) 2–18.

[3] A.M. Alklaibi, N. Lior, Membrane-distillation desalination: Status and potential, Desalination. 171 (2005) 111–131.

[4] K.W. Lawson, D.R. Lloyd, Review: Membrane distillation, J. Membr. Sci. 124 (1997) 1–25.

[5] H. Susanto, Towards practical implementations of membrane distillation, Chem. Eng. Process. Process Intensif. 50 (2011) 139–150.

[6] P. Wang, T.-S. Chung, Recent advances in membrane distillation processes: Membrane development, configuration design and application exploring, J. Membr. Sci. 474 (2015) 39–56.

[7] M. Essalhi, M. Khayet, Surface segregation of fluorinated modifying macromolecule for hydrophobic/hydrophilic membrane preparation and application in air gap and direct contact membrane distillation, J. Membr. Sci. 417–418 (2012) 163–173.

[8] M. Khayet, J.I. Mengual, T. Matsuura, Porous hydrophobic/hydrophilic composite membranes, J. Membr. Sci. 252 (2005) 101–113.

[9] M. Qtaishat, M. Khayet, T. Matsuura, Novel porous composite hydrophobic/hydrophilic polysulfone membranes for desalination by direct contact membrane distillation, J. Membr. Sci. 341 (2009) 139–148.

[10] Y. Zhang, R. Wang, S. Yi, L. Setiawan, X. Hu, A.G. Fane, Novel chemical surface modification to enhance hydrophobicity of polyamide-imide (PAI) hollow fiber membranes, J. Membr. Sci. 380 (2011) 241–250.

[11] Y. Liao, R. Wang, A.G. Fane, Engineering superhydrophobic surface on poly(vinylidene fluoride) nanofiber membranes for direct contact membrane distillation, J. Membr. Sci. 440 (2013) 77–87.

[12] F. Guo, A. Servi, A. Liu, K.K. Gleason, G.C. Rutledge, Desalination by Membrane Distillation using Electrospun Polyamide Fiber Membranes with Surface Fluorination by Chemical Vapor Deposition, ACS Appl. Mater. Interfaces. 7 (2015) 8225–8232.

[13] E.W. Washburn, The dynamics of capillary flow, Phys Rev. 17 (1921).

[14] L.R. Fisher, P.D. Lark, An experimental study of the Washburn equation for liquid flow in very fine capillaries, J Colloid Interface Sci. 69 (1979) 486–492.

[15] A.C.M. Franken, J.A.M. Nolten, M.H.V. Mulder, D. Bargeman, C.A. Smolders, Wetting criteria for the applicability of membrane distillation, J. Membr. Sci. 33 (1987) 315–328.

[16] W.R. Purcell, Interpretation of capillary pressure data, J. Pet. Technol. 2 (1950) 11–12.

[17] B.-S. Kim, P. Harriott, Critical entry pressure for liquids in hydrophobic membranes, J. Colloid Interface Sci. 115 (1987) 1–8.

[18] F. Zha, A.G. Fane, C. Fell, R. Schofield, Critical displacement pressure of a supported liquid membrane, J. Membr. Sci. 75 (1992) 69–80.

[19] A. Tuteja, W. Choi, J.M. Mabry, G.H. McKinley, R.E. Cohen, Robust omniphobic surfaces, Proc. Natl. Acad. Sci. 105 (2008) 18200–18205.

[20] A. Tuteja, W. Choi, M. Ma, G.C. Rutledge, G.H. McKinley, R.E. Cohen, S.A. Mazzella, J.M. Mabry, Designing Superoleophobic Surfaces, Science. 318 (2007) 1618–1622.

[21] S. Srinivasan, S.S. Chhatre, J.O. Guardado, K.-C. Park, A.R. Parker, M.F. Rubner, G.H. McKinley, R.E. Cohen, Quantification of feather structure, wettability and resistance to liquid penetration, J. R. Soc. Interface. 11 (2014) 20140287–20140287.

[22] A.M. Coclite, R.M. Howden, D.C. Borrelli, C.D. Petruczok, R. Yang, J.L. Yagüe, A. Ugur, N. Chen, S. Lee, W.J. Jo, A. Liu, X. Wang, K.K. Gleason, 25th Anniversary Article: CVD Polymers: A New Paradigm for Surface Modification and Device Fabrication, Adv. Mater. 25 (2013) 5392–5423.

[23] A. Asatekin, K.K. Gleason, Polymeric nanopore membranes for hydrophobicity-based separations by conformal initiated chemical vapor deposition, Nanoletters. 11 (2011) 677–686.

[24] S.H. Baxamusa, K.K. Gleason, Thin Polymer Films with High Step Coverage in Microtrenches by Initiated CVD, Chem. Vap. Depos. 14 (2008) 313–318.

[25] M. Ma, Y. Mao, M. Gupta, K.K. Gleason, G.C. Rutledge, Superhydrophobic Fabrics Produced by Electrospinning and Chemical Vapor Deposition, Macromolecules. 38 (2005) 9742–9748.

[26] D.M. Warsinger, A. Servi, S. Van Belleghem, J. Gonzalez, J. Swaminathan, J. Kharraz, H.W. Chung, H.A. Arafat, K.K. Gleason, J.H. Lienhard V, Combining air recharging and membrane superhydrophobicity for fouling prevention in membrane distillation, J. Membr. Sci. 505 (2016) 241–252.

[27] K. Honda, M. Morita, H. Otsuka, A. Takahara, Molecular aggregation structure and surface properties of poly(fluoroalkyl acrylate) thin films, Macromolecules. 38 (2005) 5699–5705.

[28] A. Liu, E. Goktekin, K.K. Gleason, Cross-linking and ultrathin grafted gradation of fluorinated polymers synthesized via initiated chemical vapor deposition to prevent surface reconstruction, Langmuir. 30 (2014) 14189–14194.

[29] C.D. Petruczok, N. Chen, K.K. Gleason, Closed Batch Initiated Chemical Vapor Deposition of Ultrathin, Functional, and Conformal Polymer Films, Langmuir. 30 (2014) 4830–4837.

[30] R.B. Saffarini, B. Mansoor, R. Thomas, H.A. Arafat, Effect of temperature-dependent microstructure evolution on pore wetting in PTFE membranes under membrane distillation conditions, J. Membr. Sci. 429 (2013) 282–294.

[31] A.B.D. Cassie, S. Baxter, Wettability of porous surfaces, Trans. Faraday Soc. 40 (1944) 546–551.

[32] A.M. Elowson, Spread-wing postures and the water repellency of feathers: a test of rijke's hypothesis, The Auk. 101 (1984) 371–383.

[33] M.C. García-Payo, M.A. Izquierdo, C. Fernandez-Pineda, Wetting study of hydrophobic membranes via liquid entry pressure measurements with aqueous alcohol solutions, J. Colloid Interface Sci. 230 (2000) 420–431.

CHAPTER FIVE

Additional contributions to Membrane Distillation (MD) membrane science using initiated chemical vapor deposition (iCVD)

Additional collaborative work is briefly summarized in this chapter. See the cited papers for more details. Chapter 5.1 describes a study conducted collaboratively with the Professor John Lienhard V. laboratory at MIT [1]. Dr. David Martin Warsinger is the first author on this work. Chapter 5.2 describes a study conducted collaboratively with the Professor Gregory Rutledge laboratory at MIT [2]. Dr. Fei Guo is the first author on this work. All figures, data and analysis were reproduced directly from the joint studies. All text is original.

Abstract

The current chapter introduces two studies that supplement the findings described in Chapters 2, 3 and 4 of this thesis. In Chapters 2 and 3, we analyzed how iCVD coatings can be designed to improve the permeability and liquid entry pressure (LEP) of MD membranes. Chapter 5.1 complements this work, adding fouling to permeability and LEP as a factor to consider when designing iCVD coatings. In Chapter 4, we used iCVD to determine how membrane morphology across different membrane types affects LEP. Chapter 5.2 extends this work, focusing on electrospun membranes and refining how their morphology can be optimized for MD. The inclusion of these two studies in this thesis supports our overall goals of advancing the science of MD membranes and working towards improved membrane and MD system performance. Dr. David M. Warsinger, Sarah Van Belleghem, Jocelyn Gonzalez, Jaichander Swaminathan, Jehad Kharraz, Hyung Won Chung, Dr. Fei Guo, Andong Liu, Professor Gregory C. Rutledge, Professor Hassan A. Arafat, Professor John H. Lienhard V and Professor Karen K. Gleason contributed to this work.

5.1. The effects of hydrophobicity and air recharging on MD membrane fouling [1]

Inorganic and organic membrane fouling limits the efficiency of membrane distillation (MD) and other desalination and water treatment systems [3]. This reduced efficiency occurs because fouling reduces active surface area, increases wetting, and increases system downtime (Fig. 5-1). Fouling of reverse osmosis (RO) and other water-treatment membranes is well-researched. However, these membranes have significantly different surface-energies compared to MD membranes. A better understanding of the fouling mechanics of hydrophobic MD membranes is needed [4].
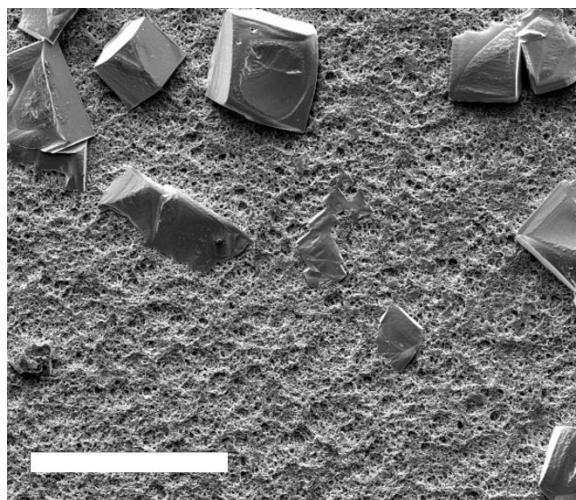
Fig. 5-1. SEM image of an iCVD-treated PVDF membrane after conducting a static MD test using a 30% NaCl solution. Salt crystals on the surface occlude pores and reduce system efficiency. Scale bar is 100 µm. Adapted from [1].

In this study, we examine two factors that influence fouling of MD membranes. Understanding these factors could make it possible to reduce fouling and so increase MD system efficiency. The first factor is the hydrophobicity of the membranes. Superhydrophobic membranes have been shown to have higher resistance to inorganic fouling than less hydrophobic membranes [5–7]. The

second factor is the presence of air layers between the membrane surface and the feed solution. Air layers can be introduced by actively inserting air, or they can be the result of air entrapment on a superhydrophobic surface. Bubbling air into the MD feed solution has been previously shown to reduce fouling [8]. In this study, we use iCVD and multiple methods of introducing air layers at the membrane surface ("air recharging") in order to examine the effects of these interventions on inorganic and organic fouling.

Classical nucleation theory predicts that increased hydrophobicity will decrease inorganic fouling. In order for inorganic fouling to occur, there must be nucleation followed by crystal growth. Increasing nucleation induction time decreases the amount of inorganic fouling that will occur. There are two types of nucleation. Homogeneous nucleation occurs in the bulk solution and has a high Gibbs free energy barrier (ΔG^*_{hom}). Heterogeneous nucleation occurs at interfaces and has a lower Gibbs free energy barrier (ΔG^*_{het}). Nucleation induction time scales exponentially with the Gibbs free energy of nucleation [9] so heterogeneous nucleation is strongly favored. It has been shown that increasing the hydrophobicity of a surface causes ΔG^*_{het} to approach ΔG^*_{hom} (Fig. 5-2) [9]. ΔG^*_{hom} is large and independent of surface energy, so the energy barrier to nucleation on the membrane surface increases with increased hydrophobicity. Increasing membrane hydrophobicity, thus has the potential to decrease nucleation and thus inorganic fouling of the membrane surface.
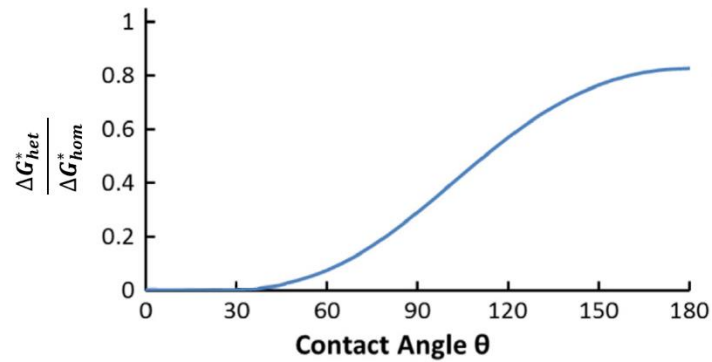
Fig. 5-2. Ratio of heterogeneous and homogeneous Gibbs free energy of nucleation. The x-axis is the liquid/solid contact angle which increases with increased hydrophobicity. Adapted from [1].

Increasing the hydrophobicity of the membrane surface also increases the likelihood of an air layer entrapped on the membrane surface. This air layer may provide an additional physical barrier to both inorganic and organic fouling. At the same time, the air layer creates an air/liquid interface near the membrane surface at which heterogeneous nucleation may occur. If the nucleated particles then settle onto the surface of the membrane, the net inorganic fouling may increase. While reduction of organic fouling is predicted, the effects of increasing hydrophobicity on inorganic fouling in the MD system must be determined experimentally.

Air recharging is another method of introducing air layers at the interface of the membrane and the feed solution. The introduced air carries inorganic and organic particles away from the membrane and acts as a physical barrier between the membrane and potential foulants. It thus has the potential to reduce both inorganic and organic fouling. However, as with increased hydrophobicity, the introduction of air layers at the membrane surface also produces a new air/liquid interface near the membrane surface. Heterogeneous nucleation of inorganic foulants can occur at this interface with a relatively low energy barrier. These nucleated particles may then

settle onto the membrane surface. In this way, air layers may increase inorganic fouling. As with increased hydrophobicity, air recharging is expected to decrease organic fouling. Its net effect on inorganic fouling must be determined experimentally. We also experimentally test the effects of the combination of increased hydrophobicity and air recharging to determine how the two interventions work together.

The base membrane in the experimental study is a commercial PVDF membrane similar to ones currently used for MD (Millipore Immobilon-PSQ, 0.2 µm) [10]. The membrane is hydrophobic as received. We increase the hydrophobicity of the PVDF membranes using iCVD of poly(1H, 1H, 2H, 2H-perfluorodecyl acrylate) (pPFDA). pPFDA has an exceptionally low surface energy (~10 mN/m compared to ~30 mN/m for PVDF). pPFDA has been used previously to increase the hydrophobicity of membranes [11–14], but this is the first time we have used it to study fouling.

Fouling was tested using a novel "static" MD system (Fig. 5-3). The static MD system allows fouling tests to be completed more rapidly (one hour per test) compared to conducting full MD trials. To conduct static MD tests, a membrane is placed on the surface of a beaker of feed solution containing potential foulants. The feed solution is heated with a hot-plate and a fan draws the heated saturated air through the membrane. Fouling takes place on the membrane surface in contact with the feed. During testing, air recharging was applied using multiple techniques. These included injecting dry air into the feed solution with a syringe and periodically removing and replacing the membrane from the surface of the feed solution. Static MD tests were conducted for the PVDF and the iCVD-treated PVDF membranes with and without air recharging. At the end of each test, the membrane was removed from the beaker and allowed to dry. The extent of fouling

was determined by weighing the membrane before and after testing. Separate tests were conducted for three inorganic and one organic foulant. These were Calcium Sulfate ($CaSO_4$), Sodium Chloride (NaCl), silica and alginate. These four species represent the dominant fouling agents in membrane distillation [4,15,16].
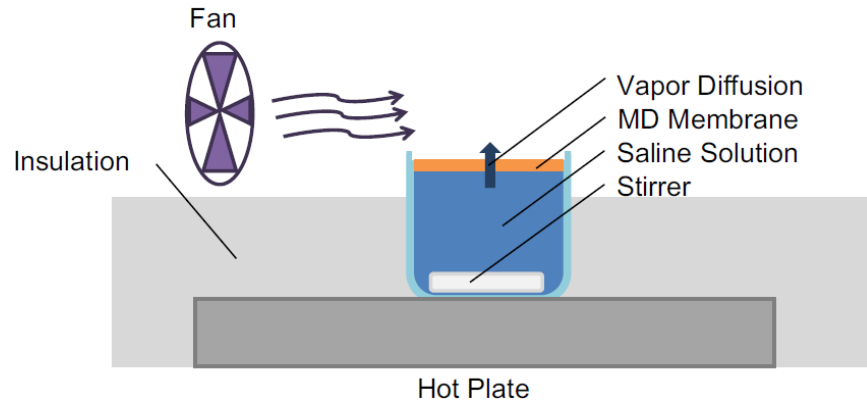
Fig. 5-3. The "static MD" system. Feed solutions containing $CaSO_4$, NaCl, silica and alginate were tested. Reproduced from [1].

A summary of the results is shown in Table 5-1. All values in Table 5-1 are the percentage change in fouling compared to an untreated PVDF membrane with no air-recharging. The effects of air recharging on inorganic fouling are mixed. When air recharging is introduced, $CaSO_4$ and silica fouling increase but NaCl fouling decreases. It appears that the net effect on inorganic fouling thus depends on the details of the situation. When the foulant is organic (alginate), we found that air recharging only reduces fouling.

Increasing hydrophobicity using iCVD of pPFDA reduces organic fouling but has a mixed effect on inorganic fouling. NaCl and CaSO4 fouling are barely changed with increased hydrophobicity, but Silica fouling increased significantly. When air recharging and increased hydrophobicity were

142

applied together, organic fouling continued to be reduced and inorganic fouling results were again mixed. This reemphasizes the conflicting influence of the air layers on nucleation on and above the membrane surface.

Table 5-1. Change in fouling for: Air recharging only, iCVD-treatment to increase hydrophobicity and both air recharging and iCVD treatment. The * indicates that the experimental uncertainty was too large to determine an exact result. Adapted from [1].

	Air recharge	iCVD	Air recharge / iCVD
NaCl	-86.5%	+18%	+50 to +99 %*
$CaSO_4$	+371%	+8.2%	-59%
Silica	+23%	+230%	+55%
Alginate	-96%	-24%	-95%

This study reviews and expands on the theory of inorganic and organic membrane fouling. Using iCVD and novel air recharging techniques, we conducted controlled experiments to isolate the effects of hydrophobicity and air recharging on fouling. This study revealed the conflicting roles of air layers, especially for inorganic foulants.

5.2. iCVD-treated electrospun membranes for membrane distillation (MD) [2]

Electrospinning is a membrane fabrication technique that produces membranes with high-porosity and sub-micron pores. Electrospun membranes have gained attention for water treatment including for membrane distillation [17,18]. However, membrane distillation requires hydrophobic membranes which is a challenge for electrospinning. Electrospinning favors polar polymers which are soluble in polar solvents and tend to be easily more easily spun into membranes. The membranes that are spun from these polar polymers are hydrophilic. Surface-modification, such as iCVD [19], is needed to lower the membrane surface energy so that the membranes can be applied for MD. In this study, we prepare a series of four electrospun membranes with systematically varying fiber diameter (Fig. 5-4). We use these membranes to determine the relationships between fiber diameter, membrane morphology and MD performance. By controlling both membrane morphology and surface chemistry, we work towards optimized electrospun membranes for MD.

As spun

(a) d=0.17±0.01 µm   (b) d=0.32±0.01 µm   (c) d=0.8±0.04 µm   (d) d≈ 1.6±0.1 µm

iCVD-treated

(e) d≈ 0.25±0.01 µm   (f) d≈ 0.43±0.02 µm   (g) d≈ 1.1±0.1 µm   (h) d≈ 1.8±0.2 µm
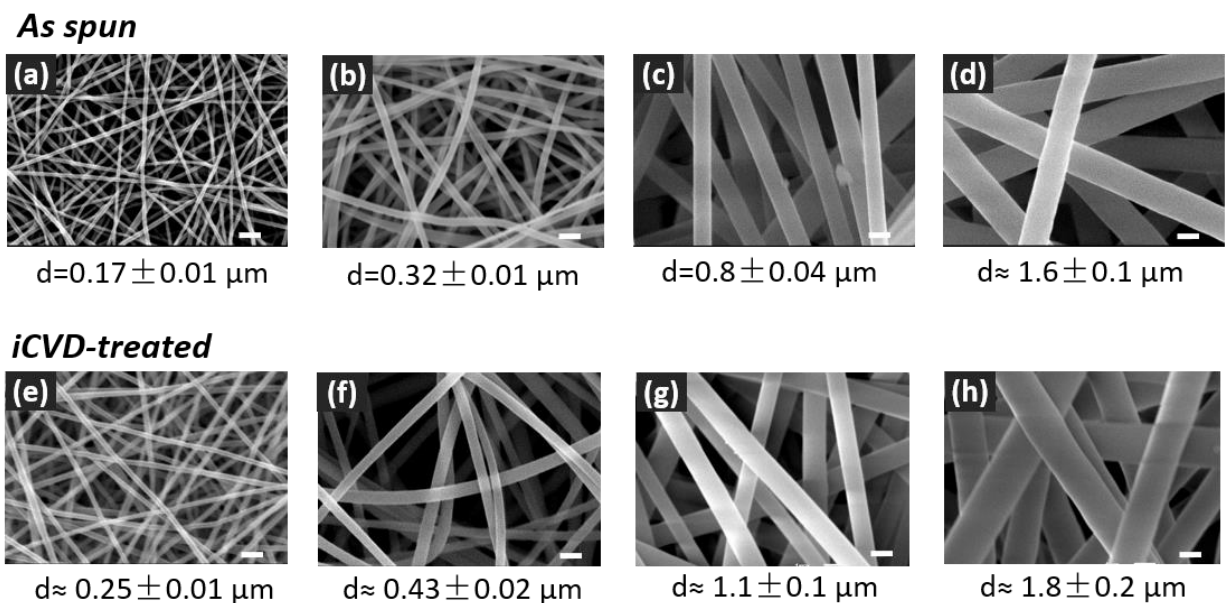
Fig. 5-4. SEM images of the four membranes (a) – (d) as-spun, and (e) – (h) after iCVD treatment. (scale bar = 1 µm). We refer to membranes (e) – (h) as M025, M043, M110, and M180 respectively. Adapted from [2].

In this study, we use poly(trimethyl hexamethylene terephthalamide) (PA6(3)T) as the electrospun material. Unlike more hydrophobic polymers, PA6(3)T has the ability to produce uniform, cylindrical electrospun fibers over a wide range of fiber diameters [20,21]. iCVD of pPFDA rendered the membranes hydrophobic. Without the use of iCVD, the PA6(3)T electrospun membranes could not be used for MD (Fig. 5-5a). iCVD has been used previously to treat electrospun membranes and other complex structures [11–14] and was chosen for its exceptionally low surface energy. The fiber diameters of the four membranes, post iCVD treatment, ranged from 0.25 µm to 1.8 µm. All membranes were 55 µm thick.

The four membranes were tested for liquid entry pressure (LEP) and air gap membrane distillation (AGMD) performance. LEP of each membrane was measured in a custom-built system. This system used a syringe pump to pressurize liquid against the membrane. The other surface of the membrane was exposed to ambient air. By increasing the volume displacement of the pump, the pressure difference across the membrane was increased until breakthrough occurred. The pressure at breakthrough is the liquid entry pressure. After breakthrough, the pressure across the membrane decreases rapidly before equilibrating at a lower value. Fig. 5-5 shows the pressure difference across the membranes over the course of the LEP tests.
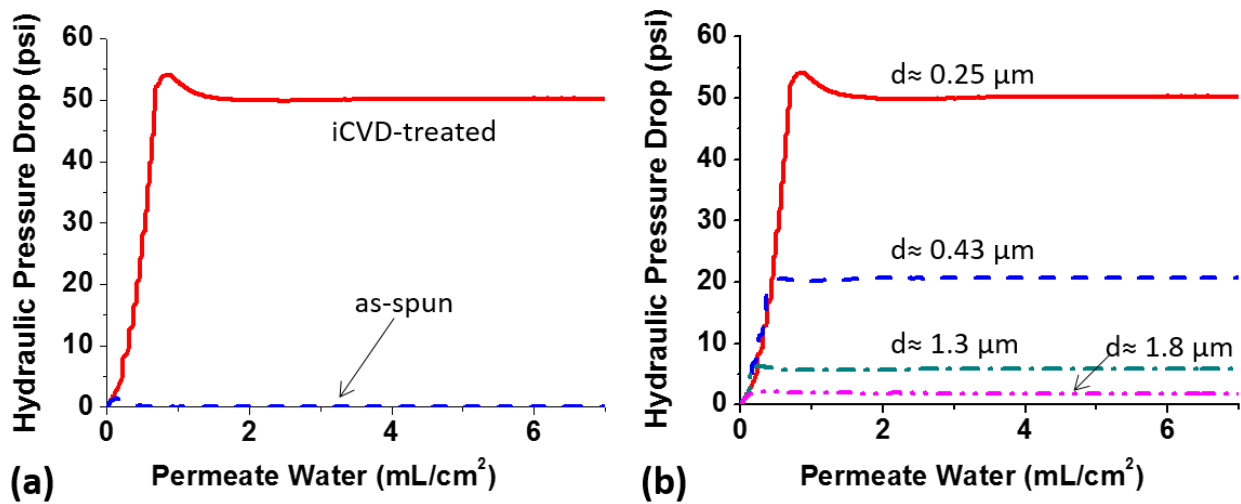
Fig. 5-5. The pressure differences across the membranes with respect to the volume displacement of the syringe pump. (a) A representative membrane (M025) before and after iCVD treatment. (b) The four membranes after iCVD treatment. LEP is the maximum hydraulic pressure difference observed for each membrane. 1 psi = 6.895 kPa. Reproduced from [2].

Prior to iCVD treatment, the four membranes wet immediately upon testing (Fig. 5-5a). This indicates that the as-spun PA6(3)T membranes have LEP values at or below zero. After iCVD

146

treatment with pPFDA, LEP was significantly increased (Fig. 5-5b). LEP varied from membrane to membrane, increasing with decreased fiber diameter. The LEP results were analyzed to determine the effective pore sizes of the four membranes. For electospun membranes, the pores are defined as the spaces between the fibers. Four models were used to calculate pore size from the measured LEP (Fig. 5-6). These models were developed by Young-Laplace [22], Tuteja [23] and Rijke [24]. The four models predict different exact values for pore size. However, they all show the same overall trend of increasing pore size with decreasing fiber diameter.
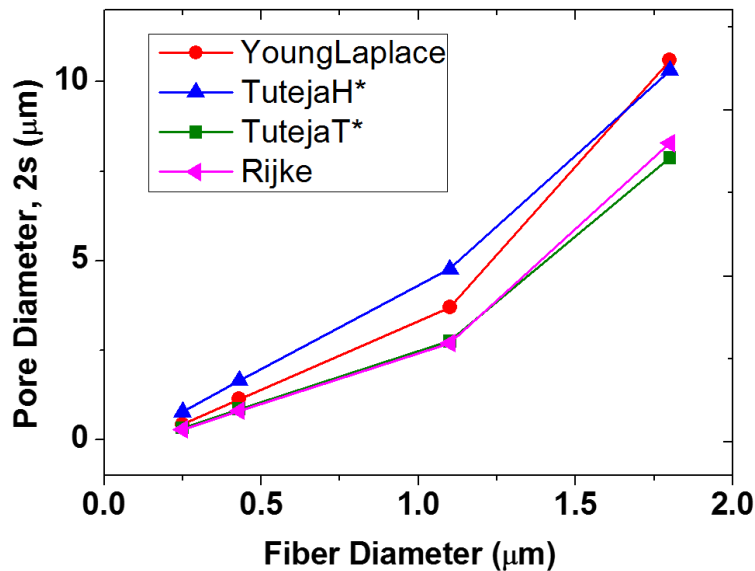
Fig. 5-6. Pore diameter calculated from measured LEP values for the four membranes. Four separate models for LEP were used: Young-Laplace, Tuteja H*, Tuteja T* and Rijke. Reproduced from [2].

Having determined how fiber diameter affects pore size and LEP, we next tested the AGMD performance of the four membranes. In AGMD, water vapor is driven through the membrane by a partial pressure gradient. This partial pressure gradient is induced by heating the feed solution on one side of the membrane, and cooling a condenser plate held millimeters from the other side of

the membrane. The larger the difference between the feed and plate temperatures, the higher the

vapor flux. AGMD vapor flux was recorded at a series of feed temperatures for each membrane.

The temperature of the feed solution (3.5 wt% NaCl) was varied from 40 and 80 °C. The

temperature of the cooling plate was maintained at 25 °C. The results from these tests are shown

in Fig. 5-7. We found that decreasing fiber diameter correlates with increasing vapor flux. Salt

rejection was > 99.98 % for all four membranes for feed temperatures less than 70 °C. However,

salt rejection declined at higher temperatures for the two membranes with the largest fiber

diameters (M110 and M180). This indicates that the LEP of these two membranes was surpassed

at higher temperatures, causing membrane wetting and cross-contamination.
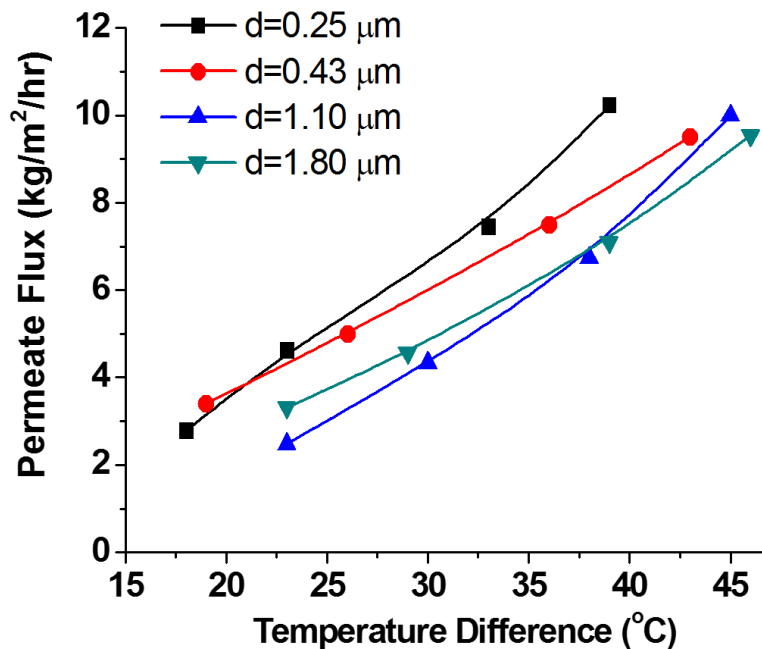

Fig. 5-7. Air gap membrane distillation (AGMD) vapor flux through the four iCVD treated

membranes. Reproduced from [2].

Considering pore size, LEP, and AGMD performance together, some interesting patterns emerge.

We found that smaller fiber diameter correlates with smaller pore size. This is expected as

membranes consisting of thinner fibers have many more pores than membranes with thicker fibers. Smaller diameter fibers also correlated with higher LEP and increased robustness to wetting in the AGMD system. This higher LEP for the membranes with smaller diameter fibers is consistent with their smaller pore size.

A more surprising result is that smaller fiber diameter also correlates with increased AGMD vapor flux. This is despite the membranes with smaller fiber diameter having smaller pore size which we would expect to cause reduced flux. One possible explanation for this finding is that smaller fiber diameter gives rise to decreased tortuosity [20,25]. Another possibility is that higher surface diffusion occurs due to larger surface area for membranes with smaller fiber diameter.

This study demonstrates how PA6(3)T and iCVD can be used together to prepare novel membranes for MD. The combination of electrospun PA6(3)T and iCVD is especially versatile due to the ability to control both membrane morphology and surface energy. By varying fiber diameter, we show that decreasing fiber size improves both LEP and water vapor flux. Further work is needed to fully understand these seemingly contradictory results.

5.3. Conclusions

In Chapter 5.1, we found that decreasing surface energy reduces organic fouling but does not have a consistent effect on inorganic fouling. Introduction of air layers at the membrane surface has similar results. These findings suggest that if an MD system has high risk of organic fouling, it may be prudent to increase hydrophobicity regardless of whether the increased hydrophobicity is needed for adequate LEP. If inorganic fouling is the larger concern, it may be beneficial to have a

less hydrophobic surface. These findings must be integrated with the results from Chapter 3 which may favor more or less hydrophobic iCVD coatings. To further integrate LEP and fouling considerations, an extension of this study could be conducted by preparing additional membranes treated with a wider range of iCVD chemistries. These membranes would provide a more continuous view of how LEP and fouling are affected the iCVD coating.

In Chapter 4, we predicted that electrospun membranes have a favorable morphology for LEP. Chapter 5.2 refines this observation, showing that electrospun membrane performance can be further improved by reducing fiber diameter. This agrees with the finding in Chapter 4 that a lower ratio of fiber to pore diameter correlates with increased LEP. This study could be extended to analyze the effects of other aspects of electrospun membrane morphology on MD performance. For instance, membrane thickness, porosity and pore size could be varied and the effects on LEP, permeability, water vapor flux, fouling etc. could be analyzed. With each parameter studied, we move closer to an optimized membrane morphology. Combining this with the iCVD coating optimization studies in Chapters 2, 3, and 5.1 we can develop a membrane with superior MD performance.

References

[1]   D.M. Warsinger, A. Servi, S. Van Belleghem, J. Gonzalez, J. Swaminathan, J. Kharraz, H.W. Chung, H.A. Arafat, K.K. Gleason, J.H. Lienhard V, Combining air recharging and membrane superhydrophobicity for fouling prevention in membrane distillation, J. Membr. Sci. 505 (2016) 241–252.

[2]   F. Guo, A. Servi, A. Liu, K.K. Gleason, G.C. Rutledge, Desalination by Membrane Distillation using Electrospun Polyamide Fiber Membranes with Surface Fluorination by Chemical Vapor Deposition, ACS Appl. Mater. Interfaces. 7 (2015) 8225–8232.

[3]   D.M. Warsinger, J. Swaminathan, E. Guillen-Burrieza, H.A. Arafat, J.H. Lienhard V, Scaling and fouling in membrane distillation for desalination applications: A review, Desalination. 356 (2015) 294–313. doi:10.1016/j.desal.2014.06.031.

[4]   S. Shirazi, C.-J. Lin, D. Chen, Inorganic fouling of pressure-driven membrane processes — A critical review, Desalination. 250 (2010) 236–248.

[5]   A. Razmjou, E. Arifin, G. Dong, J. Mansouri, V. Chen, Superhydrophobic modification of TiO2 nanocomposite PVDF membranes for applications in membrane distillation, J. Membr. Sci. 415–416 (2012) 850–863. doi:10.1016/j.memsci.2012.06.004.

[6]   Z. Ma, Y. Hong, L. Ma, M. Su, Superhydrophobic Membranes with Ordered Arrays of Nanospiked Microchannels for Water Desalination, Langmuir. 25 (2009) 5446–5450.

[7]   H. Zhang, R. Lamb, J. Lewis, Engineering nanoscale roughness on hydrophobic surface—preliminary assessment of fouling behaviour, Sci. Technol. Adv. Mater. 6 (2005) 236–239.

[8]   G. Chen, X. Yang, R. Wang, A.G. Fane, Performance enhancement and scaling control with gas bubbling in direct contact membrane distillation, Desalination. 308 (2013) 47–55.

[9]   E. Curcio, X. Ji, G. Di Profio, A.O. Sulaiman, E. Fontananova, E. Drioli, Membrane distillation operated at high seawater concentration factors: Role of the membrane on CaCO3 scaling in presence of humic acid, J. Membr. Sci. 346 (2010) 263–269.

[10] A. Alkhudhiri, N. Darwish, N. Hilal, Membrane distillation: A comprehensive review, Desalination. 287 (2012) 2–18.

[11] M. Gupta, V. Kapur, N.M. Pinkerton, K.K. Gleason, Initiated Chemical Vapor Deposition (iCVD) of Conformal Polymeric Nanocoatings for the Surface Modification of High-Aspect-Ratio Pores, Chem. Mater. 20 (2008) 1646–1651.

[12] A. Asatekin, K.K. Gleason, Polymeric nanopore membranes for hydrophobicity-based separations by conformal initiated chemical vapor deposition, Nanoletters. 11 (2011) 677–686.

[13] M. Ma, Y. Mao, M. Gupta, K.K. Gleason, G.C. Rutledge, Superhydrophobic Fabrics Produced by Electrospinning and Chemical Vapor Deposition, Macromolecules. 38 (2005) 9742–9748.

[14] M. Ma, M. Gupta, Z. Li, L. Zhai, K.K. Gleason, R.E. Cohen, M.F. Rubner, G.C. Rutledge, Decorated Electrospun Fibers Exhibiting Superhydrophobicity, Adv. Mater. 19 (2007) 255–259.

[15] E. Guillen-Burrieza, R. Thomas, B. Mansoor, D. Johnson, N. Hilal, H. Arafat, Effect of dry-out on the fouling of PVDF and PTFE membranes under conditions simulating intermittent seawater membrane distillation (SWMD), J. Membr. Sci. 438 (2013) 126–139.

[16] S. Lee, M. Elimelech, Relating Organic Fouling of Reverse Osmosis Membranes to Intermolecular Adhesion Forces, Environ. Sci. Technol. 40 (2006) 980–987.

[17] S. Subramanian, R. Seeram, New directions in nanofiltration applications — Are nanofibers the right materials as membranes in desalination?, Desalination. 308 (2013) 198–208.

[18] C. Feng, K.C. Khulbe, T. Matsuura, R. Gopal, S. Kaur, S. Ramakrishna, M. Khayet, Production of drinking water from saline water by air-gap membrane distillation using polyvinylidene fluoride nanofiber membrane, J. Membr. Sci. 311 (2008) 1–6.

[19] A.M. Coclite, R.M. Howden, D.C. Borrelli, C.D. Petruczok, R. Yang, J.L. Yagüe, A. Ugur, N. Chen, S. Lee, W.J. Jo, A. Liu, X. Wang, K.K. Gleason, 25th Anniversary Article: CVD Polymers: A New Paradigm for Surface Modification and Device Fabrication, Adv. Mater. 25 (2013) 5392–5423.

[20] C.-L. Pai, M.C. Boyce, G.C. Rutledge, Mechanical properties of individual electrospun PA 6(3)T fibers and their variation with fiber diameter, Polymer. 52 (2011) 2295–2301.

[21] M.M. Mannarino, G.C. Rutledge, Mechanical and tribological properties of electrospun PA 6(3)T fiber mats, Polymer. 53 (2012) 3017–3025.

[22] A.C.M. Franken, J.A.M. Nolten, M.H.V. Mulder, D. Bargeman, C.A. Smolders, Wetting criteria for the applicability of membrane distillation, J. Membr. Sci. 33 (1987) 315–328.

[23] A. Tuteja, W. Choi, J.M. Mabry, G.H. McKinley, R.E. Cohen, Robust omniphobic surfaces, Proc. Natl. Acad. Sci. 105 (2008) 18200–18205.

[24] A.M. Rijke, Wettability and phylogenetic development of feather structure in water birds, J. Exp. Biol. 52 (1970) 469–479.

[25] M.N. Silberstein, C.-L. Pai, G.C. Rutledge, M.C. Boyce, Elastic–plastic behavior of non-woven fibrous mats, J. Mech. Phys. Solids. 60 (2012) 295–318.

CHAPTER SIX

Conclusions

6.1. Overview

The objective of this thesis was to determine the effects of iCVD surface modification and membrane morphology on MD membrane performance. We analyzed how the iCVD coatings themselves affect membrane wetting, permeability and fouling. Clarifying the role of iCVD coatings informs the use of iCVD and other surface modification techniques to prepare membranes for MD and related applications. We also analyzed the effects of the underlying membrane morphology on MD membrane performance. To do this, we introduced the approach of using iCVD to standardize surface energy across multiple membranes. This approach makes it possible to isolate the effects of membrane morphology on performance across membranes types and materials. The research in this thesis enables researchers to focus membrane development on the most promising surface treatments and membrane morphologies for the MD desalination application.

6.2. Findings from each chapter

Chapter 2: iCVD surface modification effect on permeability and wettability

Surface modification is a versatile method to fabricate hydrophobic composite membranes for MD. By decoupling the underlying base membrane from the surface chemistry, more materials and manufacturing methods become available. While the goal of surface modification is to increase resistance to wetting, the surface modification also affects permeability. In this chapter, we determine the effects of iCVD film thickness and conformality on permeability. We found that, at a given LEP, permeability is maximized by minimizing iCVD film thickness. Contrary to expectation, we also determined that non-conformal iCVD films that produce "bottle-neck", asymmetric pores, reduce overall membrane performance. We extended existing permeability

models to describe these asymmetric membranes. These models were used to predict performance for a wider range of iCVD films than could be tested experimentally. The findings from this study can be applied to improve design for permeability of other surface-modified and asymmetric membranes.

Chapter 3: Effect of iCVD surface energy on wetting

In Chapter 3, we analyzed the relationship between iCVD film chemistry and LEP. Previously, hydrophobic coatings have focused on ultra-low surface energy chemistries such as pPFDA. However, there are environmental and cost disadvantages to these chemistries. Higher surface-energy, cleaner, less-expensive alternatives are desired. In this study, we experimentally quantified the relationship between liquid/membrane contact angle and LEP for a phase-inversion nylon membrane. We also extended existing models for LEP of membranes to include the effects of pore interactions. This addition makes the LEP model accurate at low (< 90 °) liquid/membrane contact angles. Data and modeling showed that adequate LEP can be achieved for liquid/membrane contact angles approaching 90 °. We demonstrated this finding by preparing a pDVB-treated phase-inversion nylon membrane for MD. This showed that pDVB can be used as an alternative to pPFDA. This study broadens the chemistries that may be considered for MD membrane surface-modification. This increases the potential to optimize the membranes for other characteristics beyond LEP.

Chapter 4: Membrane morphology effect on wetting

Collaborative work based in the Professor Arafat lab at Masdar institute, first author was Dr. Elena Guillen-Burrieza.

In Chapter 4, we used iCVD to standardize surface energy across three types of membranes (stretched, phase-inversion and track etched) to isolate the effects of membrane morphology on wetting. We found that physics-based models were inadequate to predict LEP across these membrane types. We thus developed an empirical, correlations-based approach to predict LEP. Using this approach, we found that narrow (rather than circular) pores and high surface porosity are two observable indicators of high LEP. This suggests that stretched and electrospun membranes would be ideal for MD. Given the many possible base membranes, this work helps focus future MD membrane development on the most promising membrane types.

Chapter 5.1: Effects of hydrophobicity and air recharging on fouling

Collaborative work based in the Professor Lienhard lab at MIT, first author was Dr. David Warsinger.

We used iCVD to determine how hydrophobicity and air layers at the membrane surface affect inorganic and organic fouling. Fouling is a prevalent and expensive problem for MD, and finding ways to mitigate it could greatly improve the attractiveness of MD desalination. We prepared phase-inversion PVDF membranes treated with iCVD pPFDA to make them superhydrophobic. We found that superhydrophobicity and air layers reduce organic fouling but have a mixed effect on inorganic fouling. We developed novel theory supporting these findings. This study emphasizes that, while the primary role of the iCVD film is to prevent wetting, its effect on fouling must also be considered. Further work is needed to definitively determine the trade-offs between preventing

wetting and minimizing fouling. This work is of interest to the broader scientific community in the realm of fouling reduction for both MD membranes but also other hydrophobic surfaces.

Chapter 5.2: iCVD-treated electrospun membranes

Collaborative work based in the Professor Rutledge lab at MIT, first author was Dr. Fei Guo.

In the final part of this thesis, we used iCVD pPFDA to prepare novel electrospun membranes for MD. We also used these membranes to study the effects of fiber size on MD performance. Electrospun membranes have a favorable pore structure for LEP, making them an important category of membranes for MD. iCVD surface-modification makes it possible to use hydrophilic PA6(3)T for the electrospun fibers. This is critical because PA6(3)T, unlike more hydrophobic materials, can produce electrospun membranes with controlled fiber diameter. The approach of combining PA6(3)T and iCVD allows study of the effects of fiber diameter on MD performance. We found that reducing fiber diameter resulted in smaller pore size, higher LEP, higher MD water vapor flux and greater robustness to wetting. The increase in both vapor flux and LEP is counter-intuitive and may be caused by reduction in tortuosity. Beyond these scientific findings, this study introduces a novel iCVD-treated electrospun membranes that has potential for competitive MD performance.

6.3. Recommendations for future work

The studies described in this thesis present directions for additional work to improve understanding of MD membranes. In Chapter 2, we introduced the use of iCVD-treated track-etched polycarbonate (PCTE) membranes as a test system to study iCVD-treated MD membranes. We found that PCTE membranes are especially useful for studying iCVD films because the simple

pore structure reveals any defects or unexpected properties of the films. This makes it possible to quantify the effects of the films on LEP. The PCTE pore structure is also useful for studying permeability to water vapor diffusion and forced air. There is still uncertainty about existing permeability models, especially the dusty gas model. Thus, more extensive use of iCVD-treated PCTE membranes to study permeability would be valuable both for MD membrane research as well as for broader research of gas transport in the 100-400 nm size range.

In Chapter 4, we introduced the approach of using iCVD to standardize membrane surface energy in order to analyze the effects of membrane morphology on wetting. This study produced important conclusions that inform the choice of base membranes for MD. This study can be extended by including electrospun and additional phase-inversion and stretched membranes. These additions would refine the correlations found in the original study. In addition, we recommend in-depth analysis of some of the more counter intuitive findings from the original study. These include further study of maximum pore size and membrane thickness. We recommend using a more sensitive LEP test- system to detect if partial wetting influences the findings. Using iCVD to standardize surface energy is a powerful approach for wider analysis of MD membranes. This approach can be extended to study the effects of membrane morphology on additional aspects of membrane performance including fouling, permeability and vapor flux in an MD system.

Finally, the studies described in this thesis have potential for immediate advancement of MD membrane design. We recommend further exploration of the more promising combinations of base membranes and iCVD films reported. For the iCVD film chemistry, we determined that pDVB can be hydrophobic enough to render membranes suitable for MD. pDVB is clean, inexpensive,

easy to process, and physically robust, making it an attractive option when viable. We recommend long-term testing of pDVB-treated MD membranes to determine if they may be suitable for commercialization. For cases where a more hydrophobic chemistry is needed, we recommend pDVB-pC6PFA bilayers as an environmentally-friendly replacement for pPFDA with similar surface properties. However, the pC6PFA chemistry may require further study before it can be controlled well enough for commercialization. The closed-batch iCVD configuration is helpful to deposit ultra-thin pC6PFA, but more work is needed. For the base membrane, electrospun and stretched membranes have characteristics well-suited for high LEP. In particular, iCVD-treated PA6(3)T electrospun membranes have exceptionally versatile design. We recommend optimizing these membranes to determine if they can be competitive for MD. If they are, demonstrating their commercial viability could be a significant step towards improving MD membrane design and increasing the appeal of MD desalination technology.